APPLICATIONS OF HIGH RESOLUTION AND ACCURACY FREQUENCY MODULATED CONTINUOUS WAVE LADAR

by

Ana Baselga Mateo

A thesis submitted in partial fulfillment
of the requirements for the degree

of

Master of Science

in

Optics and Photonics

MONTANA STATE UNIVERSITY
Bozeman, Montana

November 2014

DEDICATION

To my parents.

ACKNOWLEDGEMENTS

I would like to express my gratitude to Zeb Barber for sharing his knowledge and guiding me through this research work, you have been a great mentor for me. Thanks for patiently answering all my questions. Furthermore I would like to acknowledge Randy Babbitt, John Carlsten, Joseph Shaw, Cal Harrington, Tia Sharpe, Jason Dahl, Cooper McCann, Pushkar Pandit, Krishna Rupavatharam, Russell Barbour, Sue Martin, Diane Harn, Sarah Barutha and Margaret Jarrett. Thanks to all of you for the unconditional support, advice and help through my adventure in grad school. I could not have done it without you. Last but not least, I would like to thank my loved ones, both from Montana and Spain, for always being there for me.

TABLE OF CONTENTS

TABLE OF CONTENTS - CONTINUED

LIST OF TABLES

Table Page

LIST OF FIGURES

Figure Page

LIST OF FIGURES-CONTINUED

Figure Page

LIST OF FIGURES-CONTINUED

Figure Page

ABSTRACT

The high resolution frequency modulated continuous wave (FMCW) laser and detection ranging (LADAR) system developed by Spectrum Lab and Bridger Photonics Inc. could be potentially used for volume metrology purposes. However, comparisons with other length metrology methods would help to determine its actual precision and accuracy.

An ultra-low phase noise and narrow bandwidth laser centered at 1536nm is used to build a displacement tracking interferometer for comparisons. Lock-in detection based on phase modulation is used to reduce sensitivity to amplitude noise. The data is processed to obtain an accurate displacement measurement with a novel fringe counting technique that provides resolution higher than $\lambda/4$. After calibrating and figuring out the stability of the FMCW LADAR, its ranging capability is determined by comparison with these results along different wavelength regions.

Furthermore, we propose a combination of the trilateration techniques with the FMCW LADAR system for accurate 2D metrology. This idea is developed from design to implementation stages. Surface profiles of non-cooperative diffuse targets using lasers sources with different optical bandwidths are presented. A photon budget and an error analysis of the experimental results are also included.

INTRODUCTION

Background

LADAR (Laser Detection and Ranging) is the optical counterpart of RADAR (Radio Detection and Ranging), which measures the distance to a target by illuminating it with a pulse of light and analyzing the reflected light. The earliest variation of LADAR systems developed in nature millions of years ago: bats generate ultrasound waves via the larynx, emit the sound through their open mouths/noses and study the correspondent echo to create a 3D view of the surroundings. In 1886 the German physicist Heinrich Herzt showed that radio waves could be reflected from solid objects and in 1904 the also German inventor Christian Hulsmeyer experimentally demonstrated this by detecting a ship in dense frog with the first known form of RADAR (he called it "Telemobiloscope"). The first LADAR was developed in the early 1960s, shortly after the invention of the laser. As laser light has a much shorter wavelength than radio waves, it allowed to accurately measure much smaller objects than with RADAR. Although at the beginning LADAR was mainly used for meteorology purposes (to measure clouds, aerosols,…), nowadays it is a widely used tool with applications in many fields such as archeology, geology, seismology, remote sensing, atmospheric physics, laser altimetry, airbone and laser swath mapping.

Frequency modulated continuous wave (FMCW) LADAR (also called swept frequency chirped interferometry) is a well-known distance measurement technique. By stretching the frequency content of the emitting signal in time, and using heterodyne

coherent detection and performing the mixing in the optical domain, the system provides high sensitivity to low power returning signals and the great advantage of being able to use low bandwidth analog to digital converters (ADC's). Moreover, spreading the pulse in time also lowers the peak optical powers, making it more compatible with fiber optic amplification and delivery. All these benefits have made FMCW LADAR a very attractive solution for many ranging systems.

Motivation

FMCW systems have been proposed in the past to sense both absolute and relative lengths on the micro to nanometer range [1]. However, until recently the sweep nonlinearity and coherence of swept wavelength laser sources has limited the utility of FMCW LADAR. MSU and Bridger Photonics have demonstrated 5 THz bandwidth resulting in a resolution of 30 μm [2]. Calibrating and measuring the stability of the chirp rate of this FMCW LADAR source is one of the major goals of this project. The second major objective is to demonstrate that this chirp rate calibration accuracy for the FMCW LADAR source translates into the accuracy of the length measurements. In order to measure anything to a particular accuracy it must be at least as stable as the accuracy desired [3]. Therefore, a head-to-head comparison of a continuous wave (CW) interferometer displacement measurement technique and the FMCW LADAR system was done to demonstrate the accuracy of the latter in one dimensional metrology. Regarding 3D metrology, triangulation based systems as laser trackers are the leading solution on the current market. However, they have deficiencies that could be addressed by use of an

ultra-high resolution LADAR based metrology system [4]. Consequently, I propose and demonstrate in this thesis a two dimensional metrology system for passive non-cooperative targets based on trilateration principles and using a highly stabilized FMCW LADAR source.

Outline

The Chapter 2 includes the theoretical and mathematical fundamentals necessary to understand and follow the work done for this thesis. The three main systems in study are explained in full detail (FMCW LADAR, Interferometry and Trilateration) as well as the tools used to analyze their performance (Photon Budget, Shot Noise and Error Analysis). The Chapter 3 firstly describes the displacement tracking CW interferometer built for comparison to calibrated FMCW LADAR systems. Then, I present a full description of the FMCW LADAR system accompanied with calibrations of its chirp rate and a measure of its stability. The last part of the chapter shows the actual comparison of the two systems determining the precision and accuracy of the latter. Chapter 4 proposes a 2D trilateration system using the FMCW laser as a source. After giving an exhaustive picture of the whole experimental setup, including the calibration and the scanning processes, photon budget and shot noise analysis are carried out for two different laser sources. Two dimensional profiles of non-cooperative targets are presented. To finish, an error analysis of these results is discussed at the end of this chapter.

FUNDAMENTALS – THEORY AND MATH

Chirped Interferometry: Frequency Modulated Continuous Wave LADAR

Time of Flight (TOF) methods form a group of well-known distance measurement techniques. Basically a pulse of emitted energy travels to a reflecting object and then a receiver detects the echo that comes back following the same path. The measured elapsed time τ determines the round trip distance 2R by the use of elementary principles of physics:

$$2R = v \times \tau \,, \tag{2.1.1}$$

where v is the speed of propagation in the medium. Then, the distance R translates to the actual range to the target.

If a continuous wave modulated in frequency is used instead of a pulse, the technique is called Frequency Modulated Continuous Wave (FMCW) LADAR. In the general case, it involves the transmission of a continuous electro-magnetic wave modulated by a signal. For this thesis work, the signal varies the laser frequency as a linear function of time (t). This signal is commonly called a chirp, it is characterized by a constant chirp rate κ, a chirp bandwidth B, a chirp length τ_c (see Figure 1), a start frequency f_0 and a start time t_0, and is mathematically represented as:

$$f(t) = f_0 + \kappa * (t - t_0) \quad , \qquad \kappa = \frac{B}{\tau_c} = constant \tag{2.1.2}$$

Using $t_0 = 0$ to simplify, the electric field of the chirped signal emitted is:

$$E(t) = e^{-i2\pi ft} = e^{-i2\pi\left(f_o + \frac{1}{2}\kappa t\right)t} = e^{-i2\pi\left(f_o t + \frac{1}{2}\kappa t^2\right)} \tag{2.1.3}$$

Once emitted, the signal is reflected from the target, it arrives back at the receiver (E_{sig}), at a time $t + \tau$, and it is compared with a reference signal taken directly from the transmitter (Local Oscillator (LO) signal, E_{LO}). The received signal is shifted in time with respect the LO signal by τ seconds.

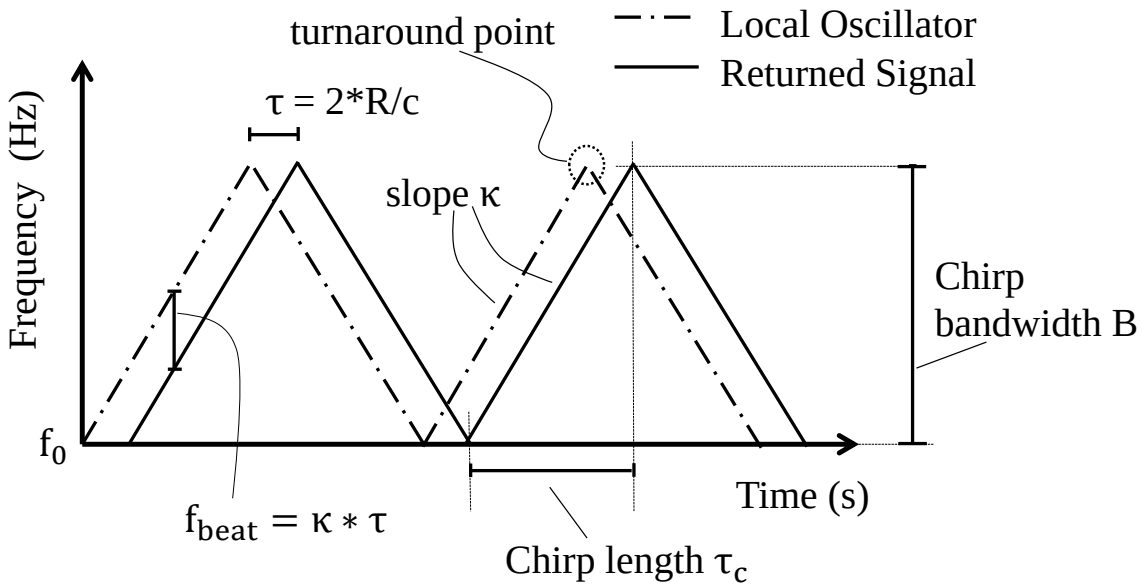

Figure 1. Chirp used for FMCW LADAR ranging measurement technique. Geometrically it can be observed that the optical bandwidth B of the chirp is equal to the product of the chirp constant κ and the chirp length τ_c.

$$E_{LO} = E_{LO_o} e^{-i2\pi\left(f_o t + \frac{1}{2}\kappa t^2\right)}$$
$$E_{sig} = E_{sig_o} e^{-i2\pi\left(f_o (t-\tau) + \frac{1}{2}\kappa (t-\tau)^2\right)} \qquad (2.1.4)$$

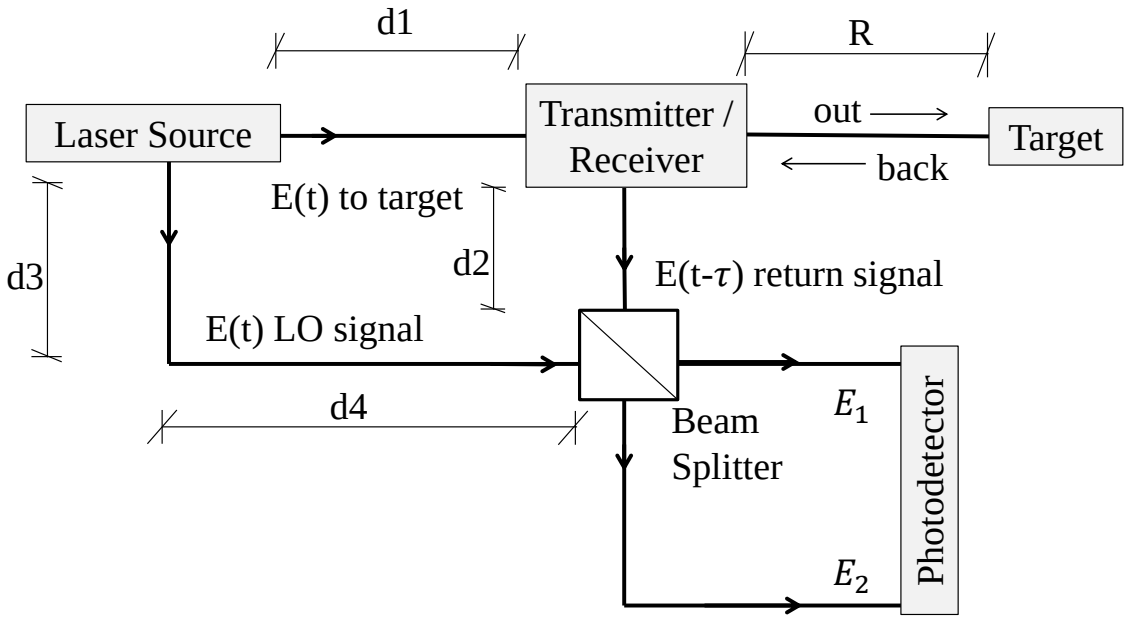

Figure 2. FMCW LADAR scheme. If the sum distance d1+d2 is equal to d3+d4 the optical path difference of the signals right before the mixer is twice the distance from the transmitter to the target 2*R which translates in a relative delay of τ.

After recombining the LO (E_{LO}) and the target signal (E_{sig}) path signals using for example a 50/50 Non Polarized Beam Splitter (NPBM), the two output beams are mathematically expressed as (ignoring an overall phase shift ϕ_o):

$$E_1 = \sqrt{\frac{1}{2}}E_{LO} - \sqrt{\frac{1}{2}}E_{sig} \tag{2.1.5}$$

$$E_2 = \sqrt{\frac{1}{2}}E_{LO} + \sqrt{\frac{1}{2}}E_{sig} \tag{2.1.6}$$

To convert this optical signal to the electrical domain a semiconductor photodiode is used. Basic balanced photodetection uses two photodiodes connected so their photocurrents cancel. A scheme of the physical implementation of this balanced technique for detection is shown in Figure 3.

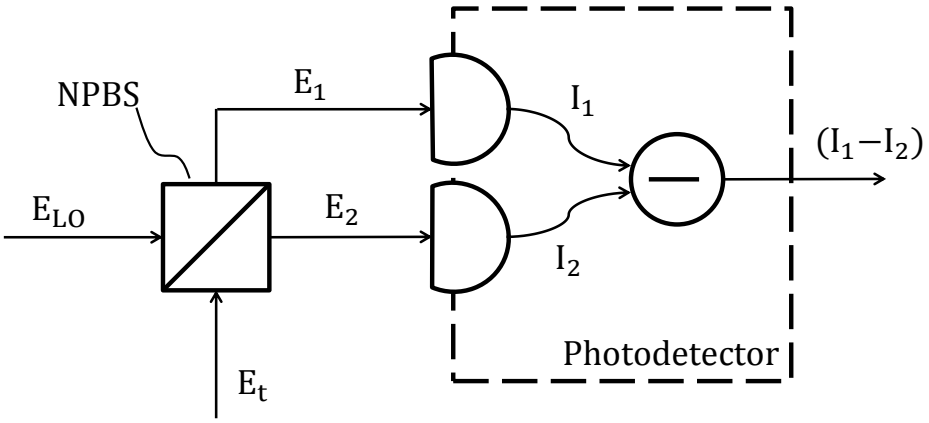

Figure 3. Photodetector balanced technique scheme.

Then, E_1 and E_2 are the inputs of the photodetector, although as every other detector, this does not see electric fields but intensities [W/m^2],

$$\begin{aligned} I_1 &= \frac{|E_1|^2}{2\eta_{medium}} = \frac{1}{4\eta_{medium}}\left[|E_{LO}|^2 + |E_{sig}|^2 - E_{LO}^* E_{sig} - E_{sig}^* E_{LO}\right] \\ &= \frac{1}{4\eta_{medium}}\left[|E_{LO}|^2 + |E_{sig}|^2\right] - Re\left(E_{LO}^* E_{sig}\right) \\ I_2 &= \frac{|E_2|^2}{2\eta_{medium}} = \frac{1}{4\eta_{medium}}\left[|E_{LO}|^2 + |E_{sig}|^2 + E_{LO}^* E_{sig} + E_{sig}^* E_{LO}\right] \\ &= \frac{1}{4\eta_{medium}}\left[|E_{LO}|^2 + |E_{sig}|^2\right] + Re\left(E_{LO}^* E_{sig}\right), \end{aligned} \tag{2.1.7}$$

where η_{medium} is the characteristic impedance of the medium [Ω] .

The output of the photodetector is the difference $(I_1 - I_2)$, where all the intensity dc residual noise terms are cancelled allowing achieving the shot noise limit.

$$I_1 - I_2 = 2\,\mathrm{Re}(E_{LO}^* E_{sig}) / (2\eta_{medium}), \tag{2.1.8}$$

and using Equations (2.1.4),

$$I_1 - I_2 = \eta_{medium}^{-1}\,\mathrm{Re}\left(E_{sig_o} e^{-i2\pi\left(f_o t + \frac{1}{2}\kappa t^2 \right)} E_{LO_o} e^{i2\pi\left(f_o t - f_o \tau + \frac{1}{2}\kappa\left(t^2+\tau^2-2t\tau\right)\right)} \right)$$
$$= \eta_{medium}^{-1} E_{sig_o} E_{LO_o}\,\mathrm{Re}\left(e^{i2\pi\left(f_o \tau + \frac{1}{2}\kappa t^2 - \kappa\tau t\right)} \right) = \eta_{medium}^{-1} E_{sig_o} E_{LO_o}\cos\left(2\pi\kappa\tau t - 2\pi f_o \tau\right)$$
$$= \eta_{medium}^{-1}\sqrt{i_{sig} i_{LO}}\cos\left(2\pi\kappa\tau t + \phi\right) = \eta_{medium}^{-1}\sqrt{i_{sig} i_{LO}}\cos\left(2\pi f_{beat} t + \phi\right),$$

(2.1.9)

where the term $\frac{\kappa\tau^2}{2}$ is small compared with the other terms in the exponential and can be neglected, ϕ is defined as an overall interferometrically sensitive phase and I have replaced the electric field amplitudes for the LO and return signals with their corresponding currents:

$$E_{LO_o} = \sqrt{i_{LO}}, \quad i_{LO} = \frac{\eta e}{E_{ph}} P_{LO}$$
$$E_{sig_o} = \sqrt{i_{sig}}, \quad i_{sig} = \frac{\eta e}{E_{ph}} P_{sig}, \qquad (2.1.10)$$

where e is the electron charge [C], η is the quantum efficiency of the photodetector , E_{ph} is the energy of a photon for the corresponding wavelength [J] and $P_{LO}$and P_{sig} are the powers for the LO signal and the return signal getting to the detector [W] . Using Equation (2.1.10) and considering the noise at the detector its ouput current results to be:

$$i_d(t) = \eta_{medium}^{-1}\sqrt{i_{LO} i_{sig}}\cos(2\pi\kappa\tau t + \phi) + i_s + i_{th}$$
$$= \frac{\eta e}{\eta_{medium} E_{ph}}\sqrt{P_{LO} P_{sig}}\cos(2\pi\kappa\tau t + \phi) + i_s + i_{th}, \qquad (2.1.11)$$

where i_s is the combination of the shot noise due to the fluctuations of the return ($i_{s_{sig}}$), LO ($i_{s_{LO}}$) signals detected and i_{th} is the thermal noise of the detector.

For operational at 1.5 micron InGaAs detectors are used and for this work are configured with auto-balance techniques to obtain a shot-noise-limited signal [5], i.e. as P_{LO} is really high, the noise due to the fluctuations of the LO photons detected ($i_{s_{LO}} \propto P_{LO}$, see detailed analysis of the shot noise in the following section) is predominant and $i_{s_{sig}}$ and i_{th} can be neglected. Ideally then, this technique allows to get rid of the residual intensity noise of the LO, that is it cancels the laser noise or "common mode noise". Therefore, the output at the detector really is:

$$i_d(t) = \frac{2\eta e}{\eta_{medium} T}\sqrt{N_{LO}N_{sig}}\cos(2\pi\kappa\tau t + \phi) + i_{s_{LO}}(t) \qquad (2.1.12)$$

Balanced photodetection techniques are commonly used for laboratory experiments that require an increased signal to noise ratio, i.e. to detect small signal fluctuations on a large DC signal [6]. In order for this balanced photodetector to work, the DC optical power has to be equalized for the two inputs. To avoid doing this manually, a low-frequency feedback loop can be implemented to maintain automatic DC balance between the signal and reference paths [6]. The auto-balanced photodetectors used for the experiments performed for this thesis were built following Hobbs' book [5].

As we can see in Equation (2.1.12) , coherently mixing a local copy of the transmitted chirp waveform (LO signal) with the return signal provides signal amplification (the amplitude of the detected signal is proportional to $\sqrt{P_{LO}}$) and dechirping of the received signal. This process of mixing, also called heterodyning, produces the beat frequencies, that is the sum and difference frequencies of the frequency of the LO and the frequency of the return signal. The dc frequency term f_{beat}, i.e. the

difference between the two is the one observed for this work and it contains the target range information. If the propagation medium is the air ($n = 1$) and c is the speed of light, using Equation (2.1.1):

$$f_{beat} = \kappa\tau = \kappa\left(\frac{2\times R}{c}\right) \rightarrow \quad R = \frac{f_{beat}\times c}{2\times\kappa} \tag{2.1.13}$$

The output signal of the photodetector is captured by a digitizer card to the computer. A great advantage of mixing the signals in the optical domain is that the bandwidth is stretched in time. This results in a reduced receiver frequency bandwidth needed to digitize the heterodyne signal. Then, a Fast Fourier Transform (FFT) is performed to translate the electrical signal into frequency domain. It is the main mathematical tool of use to analyze FMCW LADAR data in this thesis work.

The FMCW LADAR ranging technique provides an unambiguous distance result, that is, a certain range can be obtained from a single measurement. The distance to the target or range is directly proportional to the beat frequency and, as it can be seen in Equation (2.1.13), its resolution strongly depends on the linearity of the frequency variation of the chirp (i.e. how constant the slope of the chirp κ can be). If the chirp is linear but it has some noise modulation, the range resolution after the FFT would decrease. A method using a reference signal to cancel these unwanted modulations is described in detail in 3.2.1.

In order to compare TOF systems on an equal footing, one can define the downrange resolution of a TOF system (in analogy to the Rayleigh spatial resolution criteria) as the distance at which two targets being measured simultaneously can be resolved at their half power points [7].

Resolution, precision and accuracy are important factors to consider when collecting data measurements. To differentiate the meaning of these three concepts is crucial to follow this thesis work. In short, resolution is the fineness to which a measurement can be read and precision is the fineness to which a measurement can be read repeatedly and reliably. A digital stopwatch that has two digits behind the second has a resolution of 1/100 of a second but if this stopwatch is manually actuated its precision will be 1/10 of a second. Humans take in average 1/10 of a second to react to a stimulus and turn it into pressing a button. Because of this human reaction time the hundredths digit of the stopwatch is not reliable and the measurement is only repeatable to 1/10 second precision. Then, repeatability is the key difference between resolution and precision. Accuracy tells how close the measurement is to the real value, that is, it refers to the correctness of the measurement. The cartoon in Figure 4 summarizes in a visual and clear way the difference between precision and accuracy.

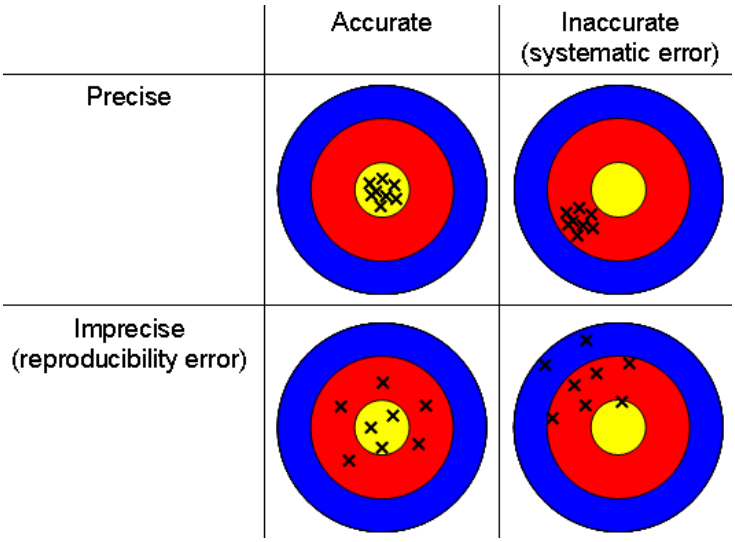

Figure 4. Accuracy versus precision scheme [8]. Resolution in this picture would be the size of the x's, i.e. the smaller the size of the x the better resolution (the finer the measurement is).

Because the signal is sampled in the time domain and transformed to the frequency domain using a Discrete Fourier Transform (DFT), the frequency resolution Δf of the source is equal to the inverse of the chirp length τ_c. Now, using Equation (2.1.13) and Equation (2.1.2) a useful mathematical expression for the maximum achievable range resolution ΔR can be derived in terms of the chirp bandwidth B as follows:

$$\Delta R = \frac{\Delta f * c}{\kappa * 2} = \frac{c}{\tau_c * \kappa * 2} \rightarrow \Delta R = \frac{c}{B * 2} \tag{2.1.14}$$

Thus, a large chirp bandwidth B is desired to achieve high range resolution. The resolution is a useful parameter for comparing ranging systems because it does not depend on any characteristics of the return light (target reflectivity, collection optics, etc.). An important advantage of using this dechirped Fourier sampling method is that unlike pulsed TOF ranging methods, the range resolution is independent of the detection bandwidth, allowing the use of lower bandwidth detectors and sampling electronics which have lower noise and higher dynamic range [9]. An estimate of a target's position can be determined better than the resolution, and is given by the range precision in determining the range, which is limited by the Cramer-Rao lower bound as $\sigma_R \approx \Delta R / \sqrt{SNR}$, where SNR is the electrical signal-to-noise-ratio [10].

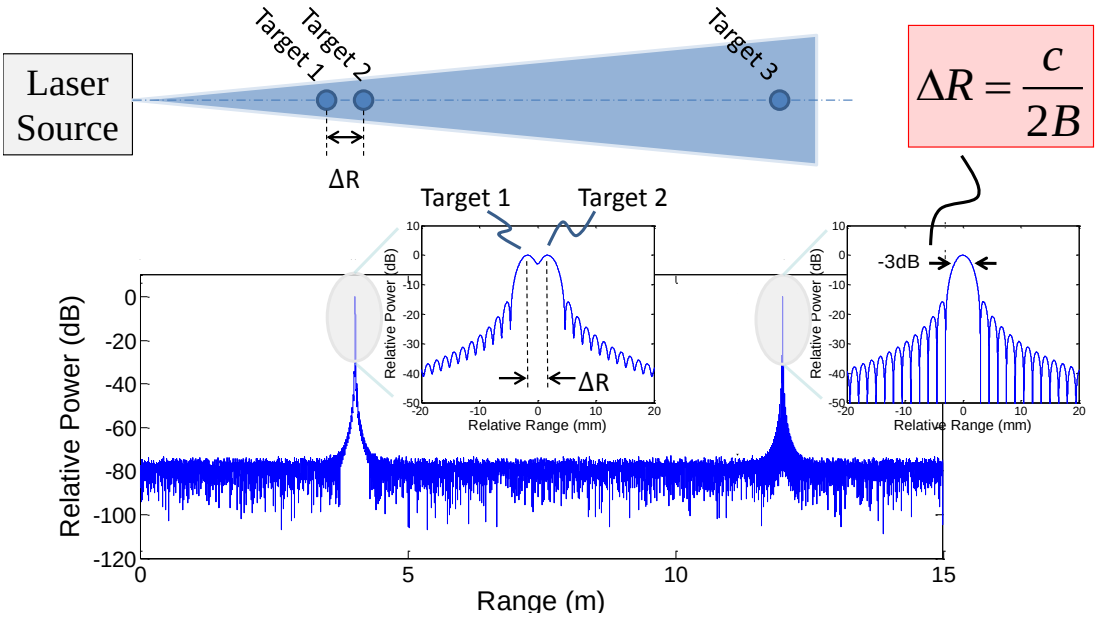

Figure 5. This figure illustrates the definitions of range resolution in the context of chirped LADAR. The independent parameter that can be used to compare all ranging systems is the bandwidth B, which is inversely proportional to the range resolution. Borrowed with permission from [3].

FMCW has been suggested in the past to measure lengths with micro- to nanometer accuracy [1]. Until recently, the chirp's deviation from linearity has been the main limitation for this metrology system. Bridger Photonics Inc. and MSU-Spectrum Lab developed a method that uses a reference interferometer to actively correct the chirp nonlinearities through electronic feedback [11]–[14]. This method allowed to perform the highest resolution LADAR ranging to date (5THz bandwidth resulting in a resolution of 30 μm) [2] and permitted most of the experimental work for this thesis.

Calibrating and measuring the stability of the chirp rate of the FMCW LADAR source is one of the major goals of this project. Performing swept wavelength molecular absorption spectroscopy on Hydrogen Cyanide HCN and on Carbon Monoxide CO

molecules allowed calibrations of laser sweeps in the C and L-band respectively with accuracy at the part per million level [15].

Consequently, another big objective for this thesis is to demonstrate that this chirp rate calibration accuracy for the FMCW LADAR source translates into the accuracy of the length measurements (1D). A head-to-head comparison of a CW interferometer displacement measurement technique and the FMCW LADAR system was done for this purpose on a table top. After this is done, I combine this ultra-high resolution FMCW LADAR with trilateration principles to demonstrate a two dimensional metrology system for passive non-cooperative targets.

Shot Noise for Coherent Heterodyne Detection

As explained before, the coherent detection with a high LO power using an auto-balanced detector dechirps the received signal and gives the coherent signal amplification which leads to the "shot noise rule of one": one coherently added photon per 1 s gives an AC measurement with one sigma confidence in a 1 Hz bandwidth. This is been verified to extend to linearly chirped waveforms [9] as the ones used for this thesis work. Therefore, with a strong LO noise, sources other than shot noise can be neglected (for example thermal noise). Shot noise is a type of electronic noise that exists when the finite number of discrete, quantized packets of photons (in light) and electrons (in current) is small enough to produce detectable statistical fluctuations in a measurement.

For linearly chirped optical fields and using a strong LO signal that allows ignoring thermal noise, the balanced heterodyne setup produces a real differential photocurrent given by Equation (2.1.12) as showed in the previous section:

$$i_d(t) = \frac{2\eta e}{T}\sqrt{N_{LO}N_{sig}}\cos(2\pi\kappa\tau t + \phi) + i_{s_{LO}}(t), \tag{2.2.1}$$

where e is the electron charge [C], η is the quantum efficiency of the photodetector, N_{LO} and N_{sig} are the mean LO and signal photon numbers in the integration time T (calculated from the Photon Budget presented in next section), respectively, ϕ is an overall interferometrically sensitive phase and $i_{s_{LO}}$ is the shot noise current. As the LO photon flux is much larger than the signal flux, $i_{s_{LO}}$ is a Gaussian random process with zero mean and variance $\sigma^2_{s_{LO}}$.

$$\begin{aligned} i_{s_{LO}} &= \eta e N_{LO}/T \\ \sigma^2_{s_{LO}} &= 2ei_{s_{LO}}B = 2\eta e^2 B N_{LO}/T \end{aligned} \tag{2.2.2}$$

In heterodyne detection for this shot-noise dominated limit the carrier-to-noise ratio (CNR), which compares the square of the mean of the signal to the square of the mean of the background noise, results to be [9]:

$$CNR = \eta N_{sig}, \tag{2.2.3}$$

where η is the quantum efficiency of the detector. Each extra signal photon increases the CNR by one ("shot noise rule of one").

The signal-to-noise ratio (SNR) compares the variance in the actual signal measurement to the square of the signal mean. Speckle phase modulation, whose origins are explained in detail in the following section, gives rise to strong apparent outliers that

increase the variance of the signal [16] therefore greatly affecting the SNR of the system. This effect can be significantly reduced with increased optical bandwidth as the variance of the signal is proportional to the logarithm of the range resolution [16] for a range unresolved surface:

$$\sigma^2 = \sigma_z^2\left(\ln\left(\frac{\Delta R}{\sigma_z}\right)-1\right) \quad for\ \frac{\Delta R}{\sigma_z} \gg 1, \tag{2.2.4}$$

where σ_z is the roughness of the target's surface (typically in the order of 3-5 μm, it can be deduced by the far-field light distribution using optical scatterometry) and the target surface is assumed to be perpendicular to the incoming laser beam. The diameter of the laser beam has to be bigger than σ_z to have speckle effect (condition always met in reality for practical experiments).

Also, it has been demonstrated that for heterodyne detection of large signals at the shot noise limit the variance is twice that observed in direct detection systems resulting in the following SNR expression [9]:

$$SNR = \frac{\left(1+\eta N_{signal}\right)^2}{1+2\eta N_{signal}} = \frac{(1+CNR)^2}{1+2CNR} \tag{2.2.5}$$

Once the SNR is known, the range precision of the system can be obtained as explained in the previous section:

$$\sigma_R \approx \Delta R \Big/ \sqrt{SNR} \tag{2.2.6}$$

Photon Budget

The initial power of light needed in a system and the signal-to-noise ratio found at the detector leads to a Photon Budget. When the source beam with radius ω_0 and power $P_{emitted}$ travels along a distance R to a target, the spot size ω of the beam at the target, i.e. the radius of the spot on the target that is illuminated, can be calculated using Gaussian optics:

$$\omega = \omega_0 \sqrt{1 + \frac{\lambda^2 R^2}{\pi^2 \omega_0^4}}, \tag{2.3.1}$$

being the area of the spot $A_{spot} = \pi\omega^2$. The Rayleigh range $R_{Rayleigh}$ of that beam is defined as:

$$R_{Rayleigh} = \frac{\pi\omega_0^2}{\lambda}, \tag{2.3.2}$$

and therefore, after traveling a distance bigger than $R_{Rayleigh}$ the spot size of the beam can be approximated as $\omega \approx \frac{\lambda R}{\pi\omega_0}$, and the divergence angle calculated with:

$$\theta = \frac{\omega}{z} = \frac{\lambda}{\pi\omega_0} \tag{2.3.3}$$

The target reflectivity ρ_T determines the amount of energy reflected and depends greatly on the material. In general, two different surface materials can be distinguished: specular and diffuse (see Figure 6). Specular reflection only reflects light back if the surface is positioned perpendicularly to the emitter/receiver or if the receiver is perfectly aligned to collect the returning light which means scanning the target is not a practical option. Therefore, specular materials are not useful for the purpose of the trilateration

measurements of this thesis and were only used experimentally to determine the accuracy/precision of the FMCW LADAR system in 1D. On the other hand, diffuse or often referred to Lambertian surfaces reflect light almost uniformly over a large scattering field allowing the collection of scattered signal mostly independent of the position of the transmitter, receivers, and the orientation of the surface. For the diffuse (Lambertian) targets under consideration on the following chapters, the scattering solid angle Ω is equal to π steradians.

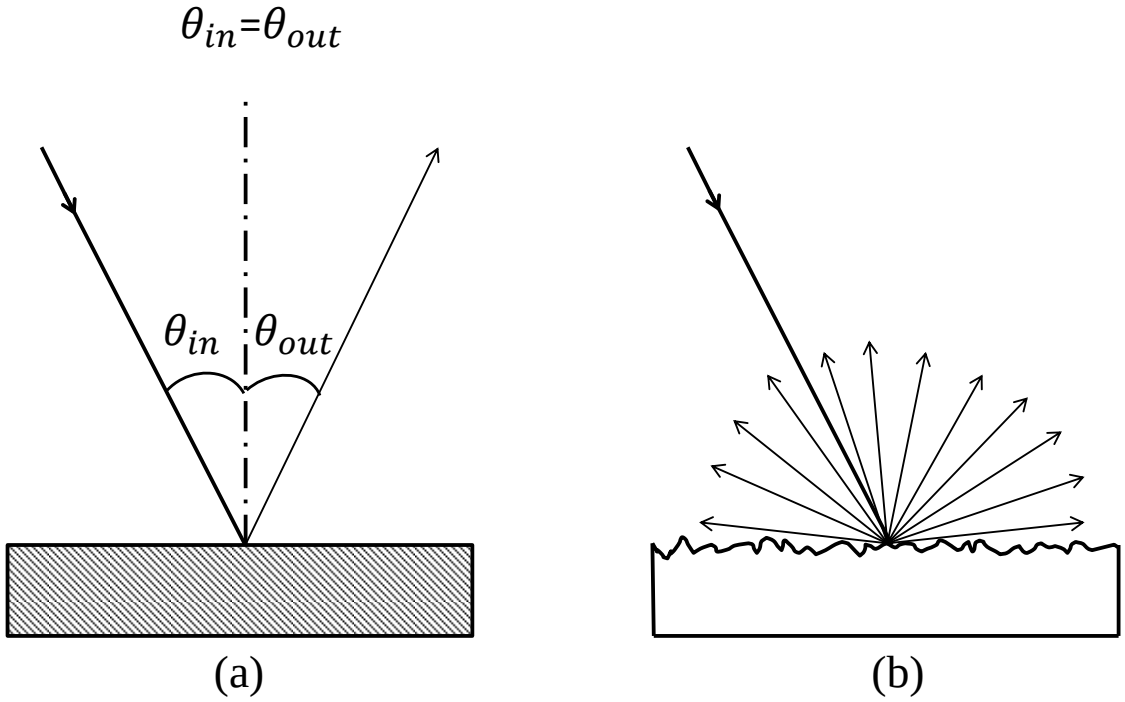

Figure 6. (a) Specular and (b) Diffuse targets.

The radiance of the area A_{spot} at the diffuse target is :

$$L = \frac{P_{emitted}\rho_T\eta_{atm}}{A_{spot}\pi} \quad \left[W/(m^2 sr)\right], \tag{2.3.4}$$

where η_{atm} is the atmospheric transmission factor. Then, the power collected back at the receiver is calculated using:

$$P_{received} = LA_{spot}\Omega_{rec}, \qquad \Omega_{rec} = \frac{A_{rec}}{R_{spot-rec}^2}, \tag{2.3.5}$$

where Ω_{rec} is the solid angle of the receiver [sr], $R_{spot-rec}$ is the distance from Lambertian source (target) to receiver [m] and A_{rec} is the area of the receiver [m^2].

Dividing the total power received by the energy of a single photon at the wavelength in use (E_{ph} [J]) gives the number of photons collected per second, allowing an easy calculation for the number of photons collected during coherence integration time T, given by $N_{collected}$ [$photons$]. The latter is necessary to calculate the final SNR and CNR of the system as explained in the previous section.

Rayleigh scattering is the biggest cause for losses in PM fibers at the wavelength used for the experiments contained in this thesis. The Rayleigh power scattered backwards from the end of the emitter's fibers increases the background noise level per range resolution ΔR bin by a factor of [17]:

$$\eta_{ray} = \gamma_{ray} \times \Delta R \times \frac{NA^2}{4n_{fib}^2}, \tag{2.3.6}$$

where γ_{ray} is the Rayleigh scattering coefficient [1/m], NA is the numerical aperture and n_{fib} is the fiber refractive index. In Chapter 4 this effect is analyzed for the trilateration setup.

Interferometry

In order to demonstrate that the chirp rate calibration accuracy for the FMCW LADAR source translates into its length measurements (1D), a comparison with a second metrology system based in interferometry principles was done. This section provides a little background in interferometry as well as its basic principles with the purpose of easily following the description in Chapter 3 of the displacement measuring CW interferometer built for this thesis work.

Interferometry is a family of techniques in which waves, usually electromagnetic, are superimposed in order to extract information about the waves [18]. Early experimentalists such as Michelson and Morley started using interferometric techniques back in the nineteenth century while trying to prove the existence and measure the properties of the luminiferous aether. This is still the most famous interferometry experiment up to date. Nowadays, interferometric techniques are commonly used in science and industry for the measurement of small displacements, refractive index changes and surface irregularities with great precision and accuracy. Gravitational-wave interferometers such as LIGO (Laser Interferometer Gravitational-Wave Observatory) are expected to measure extremely small distortions (10^{-21} m) in the suspended interferometer´s paths produced by spinning waves, slightly deformed neutron stars in our own galaxy, and other astronomical phenomena [18].

Among the several types amplitude-splitting interferometers that can be built, the Michelson interferometer stands out for being the best known and the most important historically (see Figure 7) and it is the basis of the CW interferometer built for this thesis

work. Usually, a single incoming beam of coherent light is split equally by a partially reflecting mirror (or beamsplitter). Each of these identical beams travel a different optical path ($n_1 L_1$ and $n_2 L_2$) and are recombined with the same or another beamsplitter before arriving at a detector. A physical length difference or the change in the refractive index between the two paths translates to a phase difference between the two waves. Waves that are in phase undergo constructive interference (bright ports), while waves that are out of phase undergo destructive interference (dark ports). Assuming $n_1 = n_2 = 1$ and defining $L = L_2 - L_1$, when the path difference L varies by a distance dL larger than the wavelength λ of the source, the photodetector sees a number N of bright fringes that is twice times the number of laser wavelengths included in dL.

$$dL = \frac{\lambda N}{2} \tag{2.4.1}$$

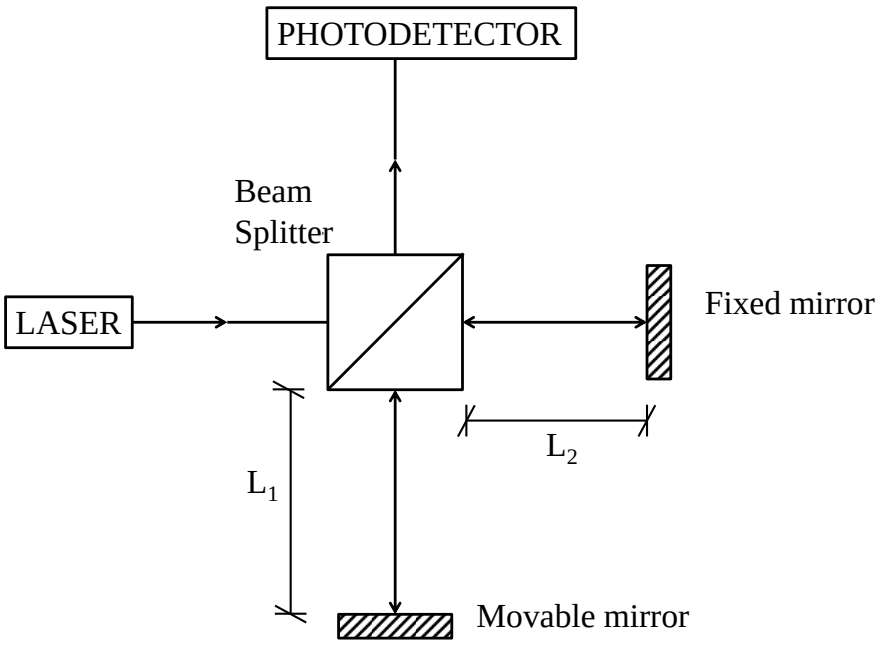

Figure 7. Michelson interferometer diagram.

Fringe-counting techniques are widely used for metrological applications [19],[20] and permit the measurement of macroscopic lengths with interferometric resolution. The output optical power of a regular Michelson interferometer is:

$$P = \frac{P_0}{2}\left(1 + C\ cos\varphi\right), \tag{2.4.2}$$

where P_0 is the input power, φ is the relative phase, and C is the fringe contrast. Converting the analog output signal of the photodetector to digital so it can be processed by a computer gives N and therefore a measure of the length dL with a resolution of $\lambda/4$ (i.e. you can detect four fringes, two bright and two dark for every wavelength) [21].

However, the results can be affected by laser power fluctuations and refractive-index variations. Moreover, it is not possible to know the direction of motion (sign of the path difference) as cosine is an even function. This is a common difficulty faced by fringe counting methods for Michelson and other interferometers whenever a resolution higher than λ is needed. As it is explained in Chapter 3, these issues were overcome using the first and second harmonics of the signal and implementing a novel fringe counting technique in the CW interferometer built for this thesis.

Trilateration

As the final goal of this thesis work, a two dimensional metrology system for passive non-cooperative targets is designed and demonstrated combining FMCW LADAR and trilateration principles. This section contains a quick review of the trilateration history, its current advantages with respect to other techniques and the

mathematical principles that make possible the surface imaging experiments shown in Chapter 4.

Trilateration is a technique used as an alternative to triangulation that relies upon absolute distance measurements only and allows the determination of the angles of the triangle using the law of cosines as shown in Figure 8.

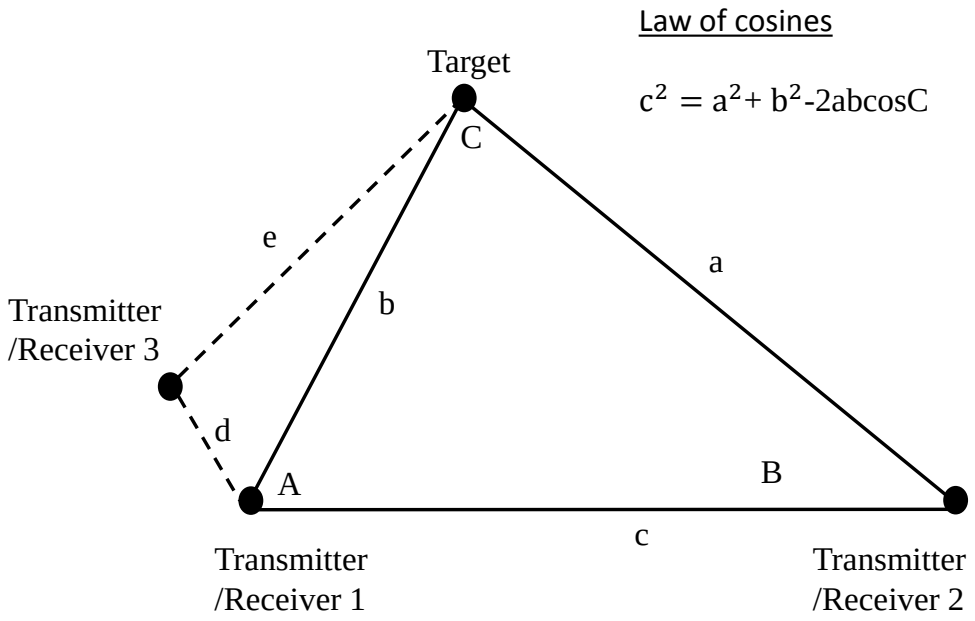

Figure 8. 2D Trilateration scheme. The law of cosines can be used to find the angle C from the absolute distance measurements of a, b and c.

One interesting aspect of the trilateration measurements is that if the goal is to find the angle measurement, this only relies on the absolute distances, so that any common mode scaling error in the distance measurements such as an unknown index of refraction of air in the measurement volume cancels in the angle measurement. Therefore trilateration has the potential to provide angular measurements with accuracy better than the distance measurements on which they are based [3].

Trilateration should not be confused with multilateration, as the first uses distances and absolute measurements versus measuring the difference in distance to two stations at known locations that broadcast signals at known times. Trilateration is a technique commonly used in navigation applications, being the basis for the Global Positioning System (GPS). It is also a cost-effective method commonly used by land surveyors to calculate undetermined positions in plane coordinate systems or by the industry to inspect manufactured parts. Commonly, the absolute distance measurements are taken using Electronic Distance Measurement (EDM) technology implemented in devices called total stations. EDM uses the propagation of electro-magnetic radiation to measure the distance between the total station and a reflector or cooperative target:

$$\frac{c}{n} = f * \lambda, \tag{2.5.1}$$

where c is the speed of light in vacuum, n is the index of refraction in the atmosphere, f is the frequency of the electro-magnetic energy of source and λ its wavelength.

A number of signals modulated at different wavelengths are sent from the same radiation source to the target. Counting the number N of wavelengths included in the returning signal for each frequency determines the distance L to the target:

$$L = \frac{N * \lambda}{2} \tag{2.5.2}$$

Some of the general drawbacks of standard EDM techniques include the need for a highly cooperative target (i.e. mirror or retro-reflector) to provide a high contrast signal and the need for a continually unobstructed interferometer path between target and measurement apparatus to ensure the fringe tracking system does not lose the target

location. Moreover, if the EDM system and the cooperative target are not placed at the same exact height, measurements have to be translated from slope distances to horizontal distances before using the law of cosines for 2D trilateration calculations.

For two dimensional trilateration technique a transmitter/ receiver device as the EDM just described gives a measurement of the distance b (see Figure 8). A second transmitter/receiver gives the distance a. Imagining these two measured distances b and a are the radii of two circles with centers in transmitter/receiver 1 (x_1, y_1) and 2 (x_2, y_2) respectively:

$$(x-x_1)^2+(y-y_1)^2=b^2 \tag{2.5.3}$$

$$(x-x_2)^2+(y-y_2)^2=a^2, \tag{2.5.4}$$

then the target position (x, y) would lie on one of the two possible intersections, that is, one of the two solutions of the system of equations above:

$$\begin{aligned} x &= \frac{x_2+x_1}{2}+\frac{(x_2-x_1)(b^2-a^2)}{2d_{12}^2}\pm\frac{y_2-y_1}{2d_{12}^2}\sqrt{((a+b)^2-d^2)(d^2-(b-a)^2)} \\ y &= \frac{y_2+y_1}{2}+\frac{(y_2-y_1)(b^2-a^2)}{2d_{12}^2}\mp\frac{x_2-x_1}{2d_{12}^2}\sqrt{((a+b)^2-d^2)(d^2-(b-a)^2)}, \end{aligned} \tag{2.5.5}$$

where $d_{12}=\sqrt{(x_2-x_1)^2+(y_2-y_1)^2}$.

An extra transmitter/receiver 3 at (x_3, y_3) providing the distance e would narrow the possibility of location for the target to one. However, often the intersection can be determined by the other knowledge such as the side of the transmitters the target is placed. The underlying assumption is that the relative distances between the transmitter/receiver devices (i.e. d and c) can be obtained independently and are known.

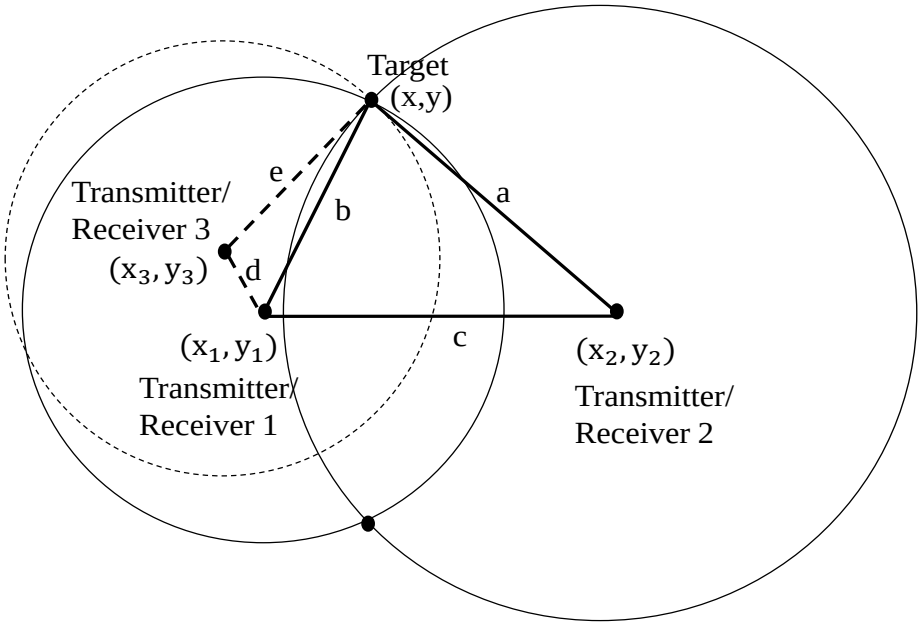

Figure 9. Trilateration scheme for a two dimensional case.

The same translates into three dimensions by positioning transmitter/receiver at different heights and finding the intersection of spheres instead of circles. However, as the solution for the intersection of two spheres is a circle, a third transmitter/receiver is needed to narrow down the solution to two points (solution for the intersection of the third sphere with the circle) and a fourth transmitter/receiver would be necessary to narrow the location of the target to one single point.

These trilateration principles can be combined with the FMCW LADAR source described in the previous section as the transmitter/receiver device, allowing overcoming many of the drawbacks of current systems. The demonstration of this system is the final goal of this thesis work.

Uncertainty Analysis

A basic error analysis consists of the estimation of the uncertainties in the measurements to find the expected uncertainty in the derived results. Two categories of uncertainties are usually distinguished. On one hand, there are instrumental uncertainties arising from a lack of perfect precision in the physical instruments used for measuring. On the other hand, overall statistical fluctuations in the measurements produce what are called statistical uncertainties [22].

Regarding the statistical fluctuations, a measure of the dispersion of the observations for a variable u (standard deviation σ_u) is found by taking the square root of the variance σ_u^2, which is defined in Equation (2.6.1). The covariance between two variables u and v, σ_{uv}^2, is analogously defined as:

$$\begin{aligned} \sigma_u^2 &= \lim_{N\to\infty}\left[\frac{1}{N}\sum\left(u_i-\bar{u}\right)^2\right] \\ \sigma_{uv}^2 &= \lim_{N\to\infty}\left[\frac{1}{N}\sum\left[\left(u_i-\bar{u}\right)\left(v_i-\bar{v}\right)\right]\right] \end{aligned} \tag{2.6.1}$$

For the experiments presented later in this thesis to perform 2D trilateration using FMCW LADAR, the final result (position of the target) is obtained from different measured variables using the geometry principles explained in the previous section. In general, the variance of the individual measured variables u, v,… can be combined to estimate the variance in the final result x using the error propagation equation [22]:

$$\sigma_x^2 \simeq \sigma_u^2\left(\frac{\partial x}{\partial u}\right)^2+\sigma_v^2\left(\frac{\partial x}{\partial v}\right)^2+\ldots+2\sigma_{uv}^2\left(\frac{\partial x}{\partial u}\right)\left(\frac{\partial x}{\partial v}\right)+\ldots=\sum_i\sum_j M_{ij}\times CovMatrix_{ij} \tag{2.6.2}$$

The Equation above will be crucial in the uncertainty analysis for the 2D metrology experiments taking place in Chapter 4.

DISPLACEMENT MEASURING INTERFEROMETER FOR COMPARISON TO CALIBRATED FMCW LADAR SYSTEMS

Overview

The high resolution frequency modulated continuous wave (FMCW) LADAR system developed by Spectrum Lab and Bridger Photonics Inc. could be potentially used for length metrology purposes. The main goal of this chapter is to compare it with another well-known length metrology method, a CW interferometer, to test its range accuracy and precision in one dimensional metrology for both cooperative and non-cooperative targets.

This chapter begins with describing the calibration of the FMCW LADAR system using methods based on molecular absorption standards. Next, an ultra-low phase noise and narrow bandwidth laser centered at 1536 nm is used to build a displacement tracking CW interferometer for comparisons with the FMCW LADAR system. Lock-in detection techniques based on phase modulation are used to reduce sensitivity to amplitude noise, and a novel fringe counting technique allows accurate displacement measurements with resolution higher than $\lambda/8$. Finally, synchronized measurements with the two systems for different wavelength regions are performed to test the one dimensional ranging calibration and capabilities of the FMCW LADAR.

The FMCW LADAR

The setup for the FMCW LADAR technique used for the research in this thesis consists of a laser source, fibers and optics to appropriately direct/split/recombine the

signal, a reference gas cell for calibration purposes, a differential detector to collect the output signal and a computer to process the data. A more detailed characterization of these components, a description of the calibration and stabilization processes and the resulting range resolution of the system are given below.

Setup

The FMCW LADAR experimental setup is shown in Figure 10. The time delay between optical path lengths introduces a frequency difference between Tx/Rx and LO paths. When heterodyned together, beat notes show up at difference frequencies and the Fast Fourier Transform of the differential detector signal reveals the range profile.

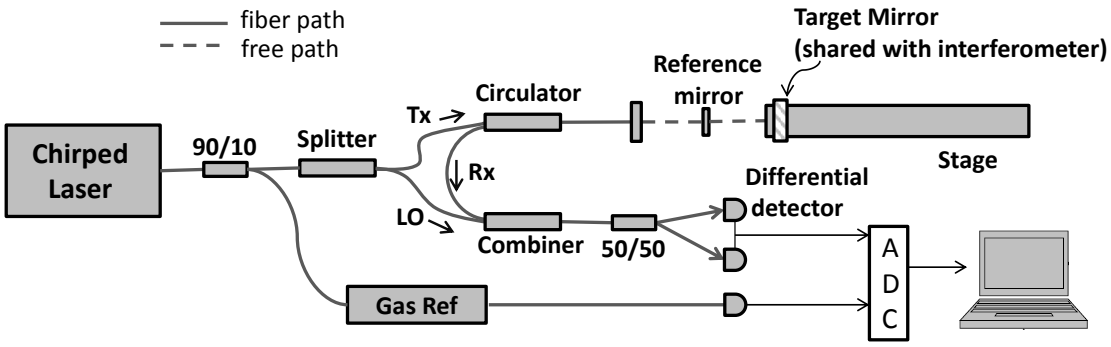

Figure 10. LADAR experimental setup.

The chirped laser source is a high resolution broad bandwidth ($\approx$ 5 THz) actively linearized FMCW LADAR system developed by Spectrum Lab and Bridger Photonics Inc. for length metrology purposes. This source provides active laser stabilization during the frequency sweep, dramatically reducing sweep nonlinearities and substantially increasing the swept source coherence length [1]. The output optical power was in the order of 2 mW and the signal was conveniently manipulated and controlled with software

from the computer. In this way, the start and end wavelengths for the sweep could be changed adjusting the theoretical bandwidth of the system, but also regulating overall instability due to the turnaround regions of the signal, i.e. the very beginning and ends of the ramps in the triangular signal (see Figure 1). These were avoided while grabbing data by setting a trigger delay $\tau_{trigger}$ and a time for reading data T_{read} (see FMCWPicoDRangesSteadyTarget.m script in Appendix). The reason for this is that in practice this region of the chirp is not completely linear (see Figure 11), thus measurements using that part of the sweep would decrease the range resolution of the results significantly. This is a trade off as the theoretical optical bandwidth of the system is reduced a little bit (see equation relating B and length of the chirp). Therefore, the optical bandwidth B_{read} is:

$$B_{read} = \kappa \times T_{read} \tag{3.1.1}$$

Once everything was configured as desired, the MATLAB script would be run and the created waveform sent out. This output chirped waveform, together with the trigger and error servo signals, were continuously monitored with an oscilloscope while taking measurements to assure good operation.

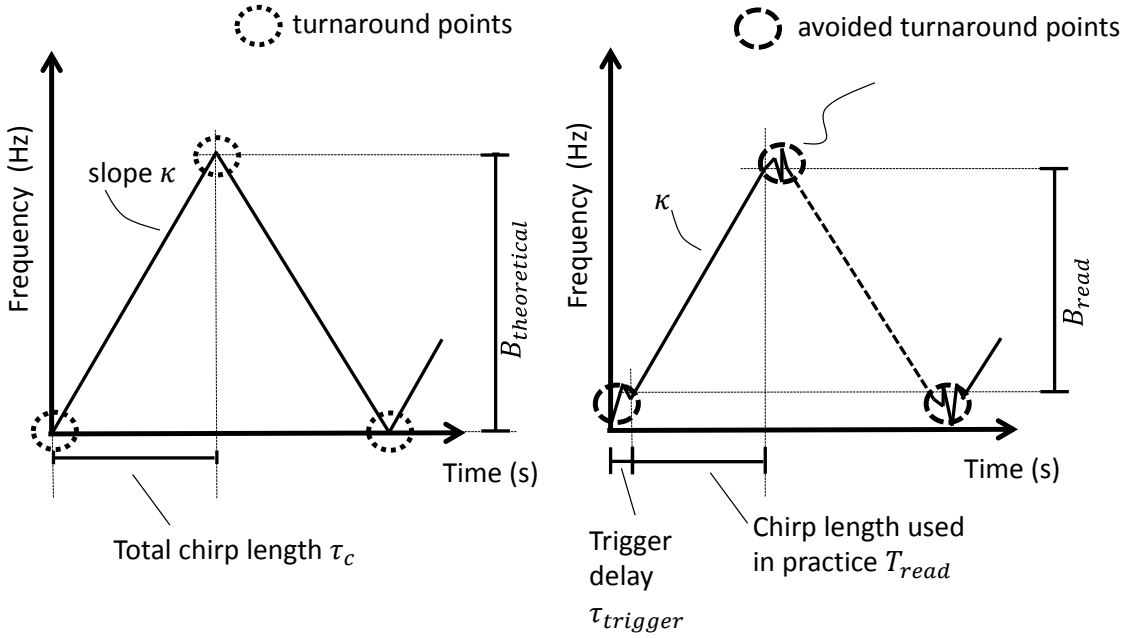

Figure 11. Ideal (left) versus real generated (right) chirp signal. The nonlinearities close to the turnaround points are avoided while taking measurements in order to maintain the range resolution of the results given by kappa.

A Zaber brand stepper motor device (stage in Figure 10) was used to move the target in 10 μm linear steps in both directions at the wished speed. The target mirror was also the target for the CW interferometer setup explained in detail in the following section. The purpose of this configuration was to allow direct measurement comparison of the two methods to determine the FMCW LADAR accuracy as it can be seen at the end of this Chapter. Moreover, the high metrology accuracy of the CW interferometer allowed to account for minimal deviations in the Zaber steps (due to vibrations, lead screw imperfections, etc.) at the last experimental stage of this thesis (2D imaging using trilateration technique).

The differential detector was built using an auto-balance technique to ensure a shot noise limited signal. The output electrical signal y is afterwards stored on the computer with a NI 5122 digitizer card:

$$y = \mathrm{Re}\left(A(t) \times \left[e^{i2\pi f_{ref} t} + e^{i2\pi f_{peak} t} \right] \times e^{i\varphi(t)} \right), \qquad (3.1.2)$$

where $A(t)$ is an amplitude modulation coming from the frequency sweep of the laser which causes the power to vary in time, $e^{i\varphi(t)}$ is a phase modulation caused by the fluctuations of the fiber path before the free space setup and also by residual imperfect linearization of the chirp, f_{ref} is the beat note produced by the signal returning after reflection upon the reference mirror and f_{peak} is the beat note from the target (see Figure 10). The reference mirror is only partially reflecting the light incident on the surface, in a way that some of the light still goes through to hit the target and the reflection of both returns back to the experiment (f_{ref} and f_{peak}). Having the extra reference mirror allowed us to cancel the unwanted modulations $A(t)$ and $e^{i\varphi(t)}$ to achieve the maximum resolution as shown below.

The data was processed using the software MATLAB [23]. The MATLAB library comes with implemented functions of great help for the development of the work in this thesis (Fast Fourier Transform, Inverse FFT, Hanning window, etc.). The frequency profile can be found by Fourier Transforming the signal y (Figure 12a). The reference frequency peak was then windowed by manually setting the lower and upper limits and keeping only the data in between (Figure 12b). Taking the Inverse Fourier Transform of this windowed signal gave y', and dividing the original signal by y' removed the unwanted modulations $A(t)$ and $e^{i\varphi(t)}$ and shifted the signal towards the origin by f_{ref}

(Figure 12c). The frequency profile (and therefore the range profile) free of modulation and noise is computed by using the FFT function and the final range was determined by fitting the right peaks to a Gaussian (see red line in Figure 14). The MATLAB code written to perform these operations can be found in the Appendix (FMCWPicoDRangesSteadyTarget.m).

$$
\begin{aligned}
& y = A(t) \times \left[e^{i2\pi f_{ref} t} + e^{i2\pi f_{peak} t} \right] \times e^{i\varphi(t)} \\
& fft(y) \\
& windowing\ fft(y) gives\ fft(y') \\
& ifft\left(fft(y') \right) = y' = A(t) \times e^{i2\pi f_{ref} t} \times e^{i\varphi(t)} \\
& \frac{y}{y'} = 1 + e^{i2\pi (f_{peak} - f_{ref}) t}
\end{aligned}
\qquad (3.1.3)
$$

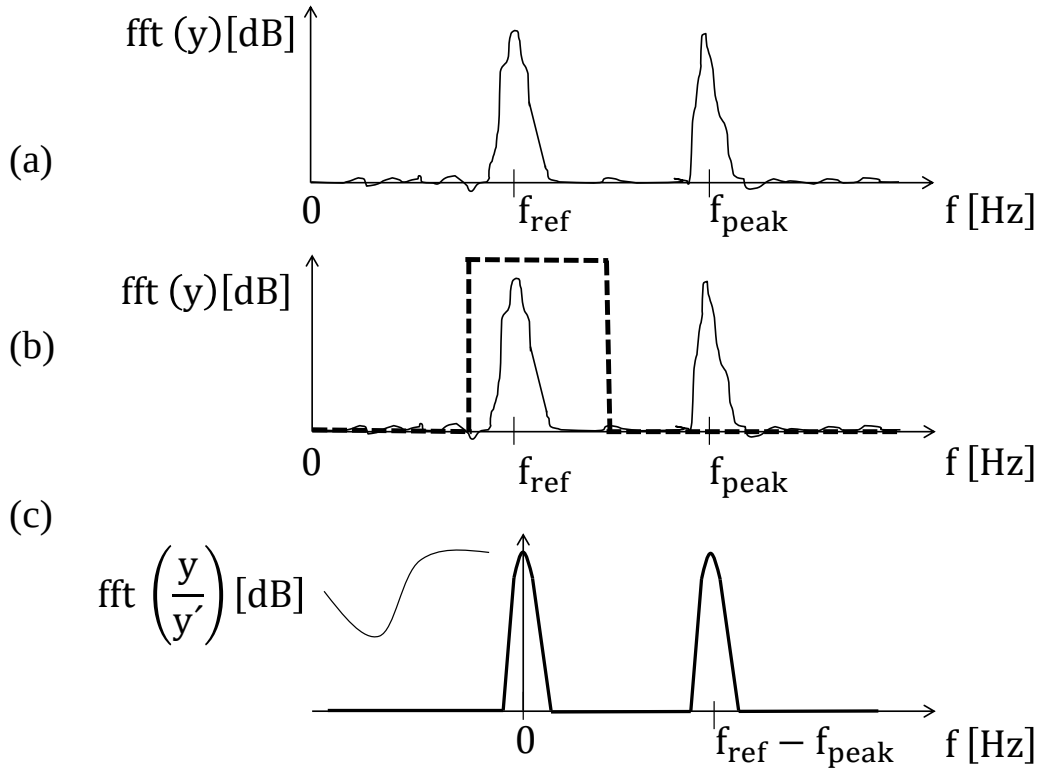

Figure 12. MATLAB processing of the collected data. The features have been exaggerated for the purpose of the explanation.

Calibration-Stabilization-Range Resolution

For this work the chirp rate calibration process consists of using the relatively sharp spectral features and broad frequency coverage of the optical absorption in a molecular gas absorption cell. By recording the transmission of laser light through a gas cell with a well calibrated molecular absorption (such as Hydrogen Cyanide (HCN)) as the laser frequency is swept, the sweep (chirp) rate the FMCW laser source can be measured and calibrated. By comparing the fitted centers of the time domain swept data to the NIST [24] calibrated frequencies one can track the laser sweep. Applying a polynomial fit to the data returns the chirp center frequency, chirp rate (slope κ), and quadratic chirp (curvature $d\kappa$), which is related to the residual dispersion in the reference interferometer of the chirp linearization system of the FMCW LADAR source [2], [25].

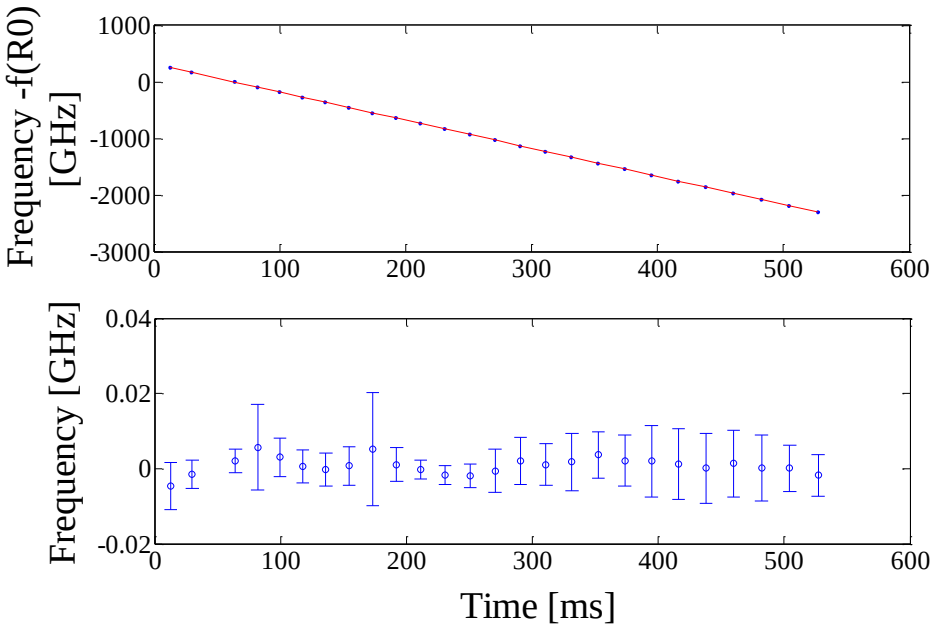

Figure 13. Calibration results using a 10 Torr Hydrogen Cyanide for a 1530 nm to 1565 nm frequency sweep. The polynomial fit returned $\kappa = 4.98834\ MHz/\mu s$ and $d\kappa = 10^{-5}\ MHz/\mu s$, which gives a relative fractional uncertainty of approximately 2 ppm.

With the chirp rate given by the calibration process (κ = 4.98834 MHz/μs) and the time period while data was being grabbed (T_{read}= 648 ms), the optical frequency bandwidth is found to be B_{read}= 3.2 THz using Equation (3.1.2). The corresponding theoretical range resolution is calculated using Equation (2.1.14)

$$\Delta R = \frac{c}{2 \times B_{read}} = 46\,\mu m\,, \tag{3.1.4}$$

where c is the speed of light. This resolution was checked by achieving it experimentally with a 3% of relative error (see Figure 14) after correcting for multiple splitting and broadening of the range peaks due to fiber dispersion [26]. Minimizing the fractional dispersion induced chirp width ΔR/R by making the LO and the Tx/Rx optical path lengths approximately equal and, therefore, minimizing relative dispersion in the two paths.

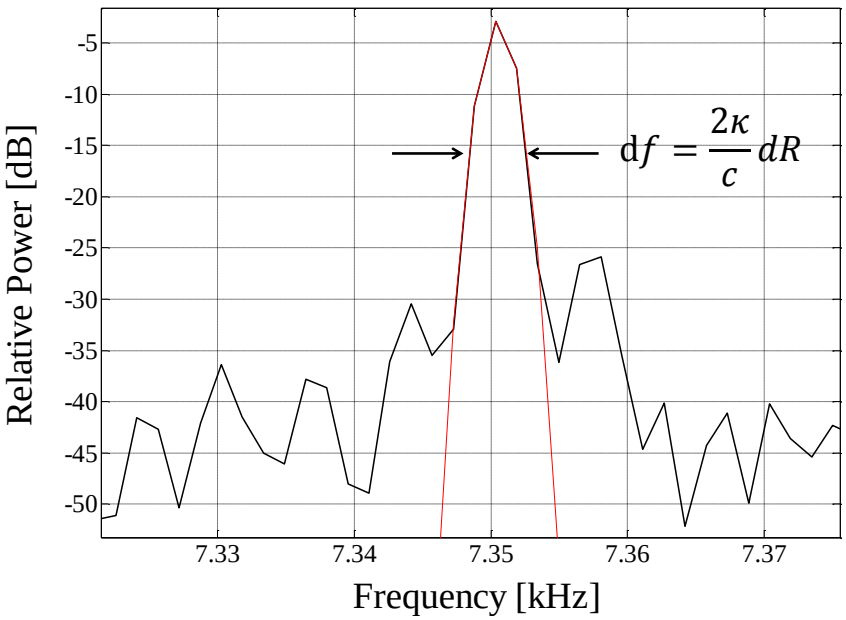

Figure 14. Determining the experimental range resolution ΔR = 48 μm (laser sweeping in wavelength from 1535 nm to 1565 nm). The red line shows the Gaussian fit used to get the final range result.

Since [27] was published, the linearity of the optical frequency of the chirped laser has been observed to have deteriorated. Technical problems and the actions to fix them lowered the PZT's resonant frequency leading to a poorer feed forward correction of the laser piezoelectric transducer (PZT). Currently, it remains linear to within a standard deviation of 350 kHz throughout a 3.2 THz chirp (from 1535 nm to 1565 nm) in 650 ms and to within a standard deviation of 200 kHz throughout a 4.7 THz chirp (from 1555 nm to 1595 nm) in 950 ms. However, at the time of its development it was shown that it remained linear to within a standard deviation of 170 kHz throughout a 4.8 THz chirp (from 1530 nm to 1570 nm) in 800 ms [2].

As the laser linearity is seen to be better at higher wavelengths, an approximately 100- Torr Carbon Monoxide cell was purchased for calibrating the laser following the same process as for the HCN cell. The calibration results are shown in Figure 4. The uncertainties on the frequencies are bigger than the ones obtained for the HCN which is due to the reference data for the CO cell being less accurate than for HCN [28].

Figure 16 shows the fluctuations of the κ result when running the calibration process 200 times in a row. The corresponding standard deviation is $1x10^{-5}$ MHz/μs, which is 2 ppm of the mean value of the chirp rate (≈ 5 MHz/μs). Moreover, the uncertainty in the chirp rate given by a single calibration (see Figure 15) is actually 5 times bigger than the standard deviation of chirp rate for 200 sequential calibrations. That is to say the reference data of CO absorption frequencies limit calibration not the stability or linearity of the chirp laser. The total bandwidth B_{read} = 4.7 THz (T_{read} = 950 ms) and the corresponding theoretical range resolution was 32 μm for this chirp configuration.

This resolution was checked by achieving it experimentally with a 23% of relative error (ΔR = 39 μm).

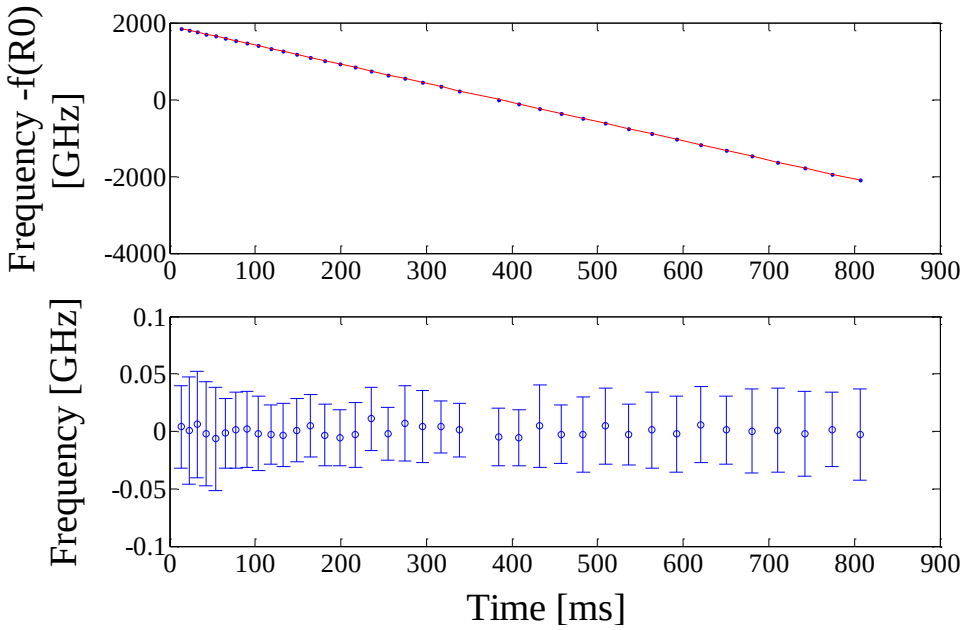

Figure 15. Calibrations results using a CO cell at 100 Torr. The polynomial fit returned $\kappa = 4.9853\ MHz/\mu s$ and $d\kappa = 5 \times 10^{-5}\ MHz/\mu s$ which gives a relative fractional uncertainty of approximately 10 ppm.

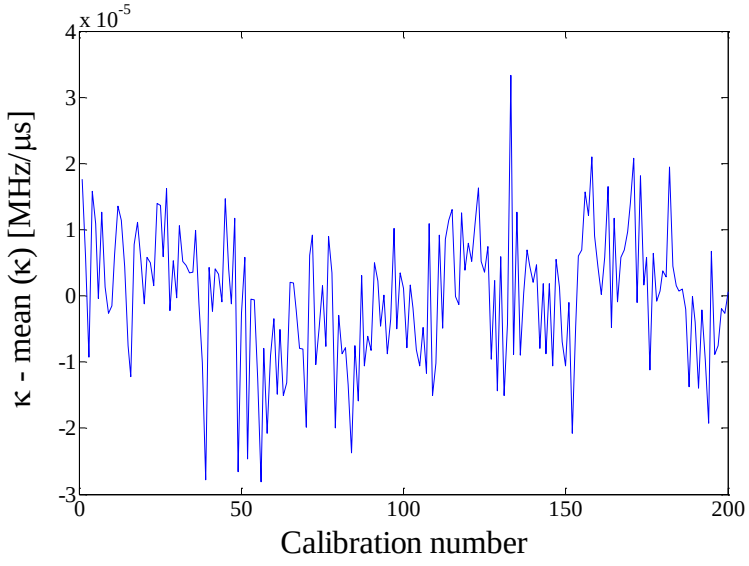

Figure 16. Chirp rate fluctuations after 200 calibrations using the CO cell, showing a fractional standard deviation in the calibration of approximately 2 ppm.

The Interferometer

Setup

In order to measure anything to a particular accuracy it must be at least as stable as the accuracy desired [3]. With the main purpose of demonstrating that the calibration accuracy of the chirp rate of the FMCW LADAR source translates into the length measurements, a CW interferometer was constructed as shown in Figure 17.

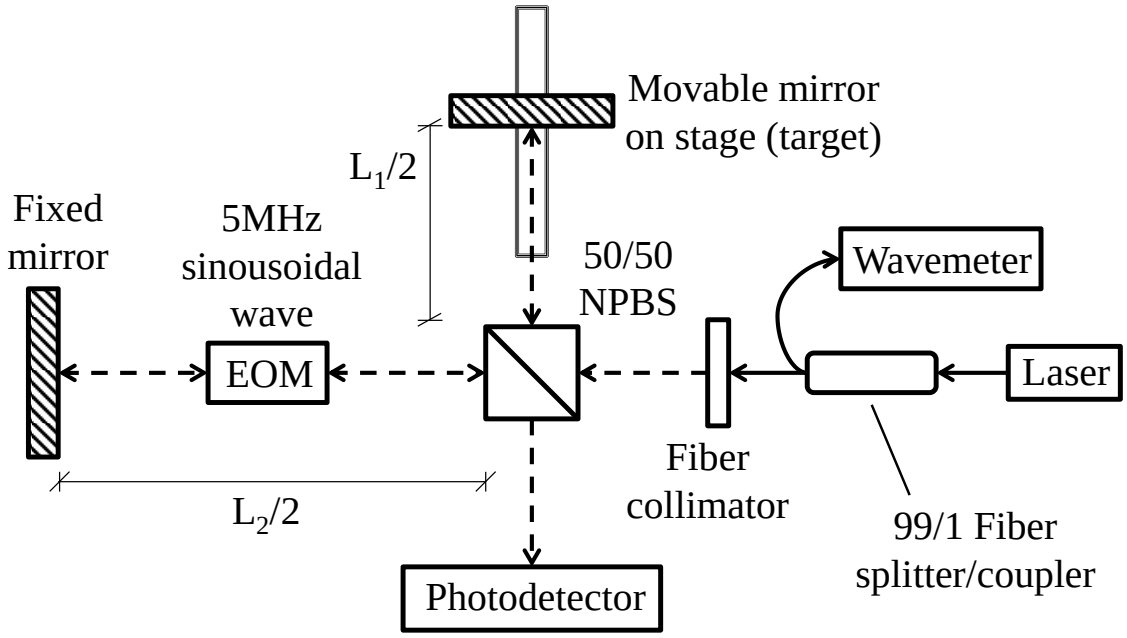

Figure 17. Experimental setup for the Michelson Interferometer. A wavemeter is used for continuously keeping track of the absolute laser wavelength. One of the interferometer's arms is phase modulated by an Electro Optic Modulator (EOM) to allow lock-in detection later.

The laser source was an ultra-low phase noise and narrow bandwidth laser centered at 1536nm. It included an optical isolator to avoid instability caused by optical feedback. The purpose of this choice of wavelength was that it is close to the wavelength of the FMCW chirp laser. Being close in wavelength reduced the effect of dispersion

(wavelength dependent index of refraction) in the air paths of the two systems and allowed the two systems to use the same optics including the target mirror.

The laser power was split (99-1%). The 99% powered fiber provided a real-time measurement of the wavelength λ with the use of a Burleigh 1500 wavemeter, thus the uncertainty in lambda was $\Delta\ \lambda\ < 2$ pm $\left(\Delta\lambda/\lambda < 1.4 \text{ ppm}\right)$, which was a key factor to monitor for reliable results as it can be seen below.

The 1% fiber path was used to interrogate the interferometer, which began with a 50/50 non polarized beam splitter (NPBS) used for dividing the incoming beam of coherent light into two identical beams. Assuming $n_1 = n_2 = 1$, each of these beams traveled a different path (L_1 and L_2) and then the beams were recombined by the NPBS before arriving at the photodetector forming the Michelson interferometer. The photodetector was specially built for this project to sense low light intensities with ordinary and cheap components [29]. As previously described in the fundamentals section, the path difference or relative displacement of the target dL can be retrieved by tracking the number N of bright fringes crossing the photodetector:

$$dL = \frac{\lambda N}{2} \tag{3.2.1}$$

The interferometer setup was constructed with a movable mirror (target) at the end of one interferometer arm mounted to a moving stage and an Electro-Optic Phase Modulator (EOM) in the other interferometer arm to provide modulation of the signal for synchronous lock-in detection (see Figure 17). To obtain pure phase modulation with the EOM it was crucial to carefully align the beam to the crystal´s propagation axis and to

orient the laser´s electric field polarization with the crystal´s electro-optically active axis. A resonant tank circuit was implemented to boost the voltage applied to the EOM at the drive frequency and reduce spurious drive frequencies. The field of the beam through the first arm after transiting the $L_1 + 2dL$ distance was:

$$E_1(t) = \sqrt{P_1}\cos\left(\omega_L t - k_L(L_1 + 2dL)\right), \qquad k_L = \frac{2\pi}{\lambda}, \tag{3.2.2}$$

where P_1 is the power of this beam and ω_L, k_L are the frequency and wavenumber of the laser. Regarding the second path, the voltage applied to the EOM for modulation was $V(t) = V_0 \sin(\omega_{ref} t)$ and therefore, the resulting signal after propagating over the L_2 distance:

$$\begin{aligned} E_2(t) &= -\sqrt{P_2}\cos\left(\omega_L t - k_L L_2 + \frac{\pi V(t)}{V_\pi}\right) \\ &= \sqrt{P_2}[\sin(\omega_L t - k_L L_2)\times \\ &\quad \sin\left(\beta\sin(\omega_{ref} t) - \cos(\omega_L t - k_L L_2)\cos(\beta\sin(\omega_{ref} t))\right)], \end{aligned} \tag{3.2.3}$$

where P_2 is the power of this beam, V_π is half-wave voltage of the EOM and $\beta = \frac{\pi V_0}{V_\pi}$. Finally, the signal once the two beams recombine was $E_d(t) = E_1(t) + E_2(t)$ and consequently, the power measured by the photodetector could be obtained by averaging over a δ_t that met the conditions $\delta_t \gg \frac{1}{\omega_L}$ and $\delta_t \ll \frac{1}{\omega_{ref}}$, to obtain

$$\begin{aligned} (E_d(t))^2 = \frac{P_2 + P_1}{2} &- \sqrt{P_1}\sqrt{P_2}[(1 - \frac{\beta^2}{4})\cos(d) \\ &+ \frac{\beta^2}{4}\cos(d)\cos(2\omega_{ref} t) + \beta\sin(d)\sin(\omega_{ref} t)], \end{aligned} \tag{3.2.4}$$

where $d = k_L(L_2 - L_1 - 2dL)$ and the first term is a DC offset that is ignored. Second order approximations were made as only the two first harmonics are of interest.

Lock in Detection Technique

Lock-in detection is a "phase sensitive detection" (PSD) technique used to measure small AC signals. Lock-in detection can be implemented using hybrid digital\analog techniques that utilize switched gain amplifiers or analog RF techniques that use RF mixers and filters. Here RF techniques were used to allow high modulation rate and achieve the higher bandwidth required to keep track of fast moving targets. The RF base lock-in system is described in Figure 18.

The interferometer signal was modulated by the EOM with a high reference frequency (ω_{ref}) (on the order of 5 MHz) driven by an RF oscillator. The lock-in detection was achieved by multiplying the photodetector signal by the fundamental (ω_{ref}) and the second harmonic of the reference frequency ($2\omega_{ref}$), using a splitter and two independent mixers (see Figure 18). The reference signals were:

$$\begin{aligned} V_f &= V_0 \sin\left(\omega_{ref} t + \theta_{ref}\right) \\ V_{2f} &= V_0 \sin\left(2\omega_{ref} t + \theta_{ref}\right), \end{aligned} \tag{3.2.5}$$

where V_0 is the same as the amplitude going to the EOM.

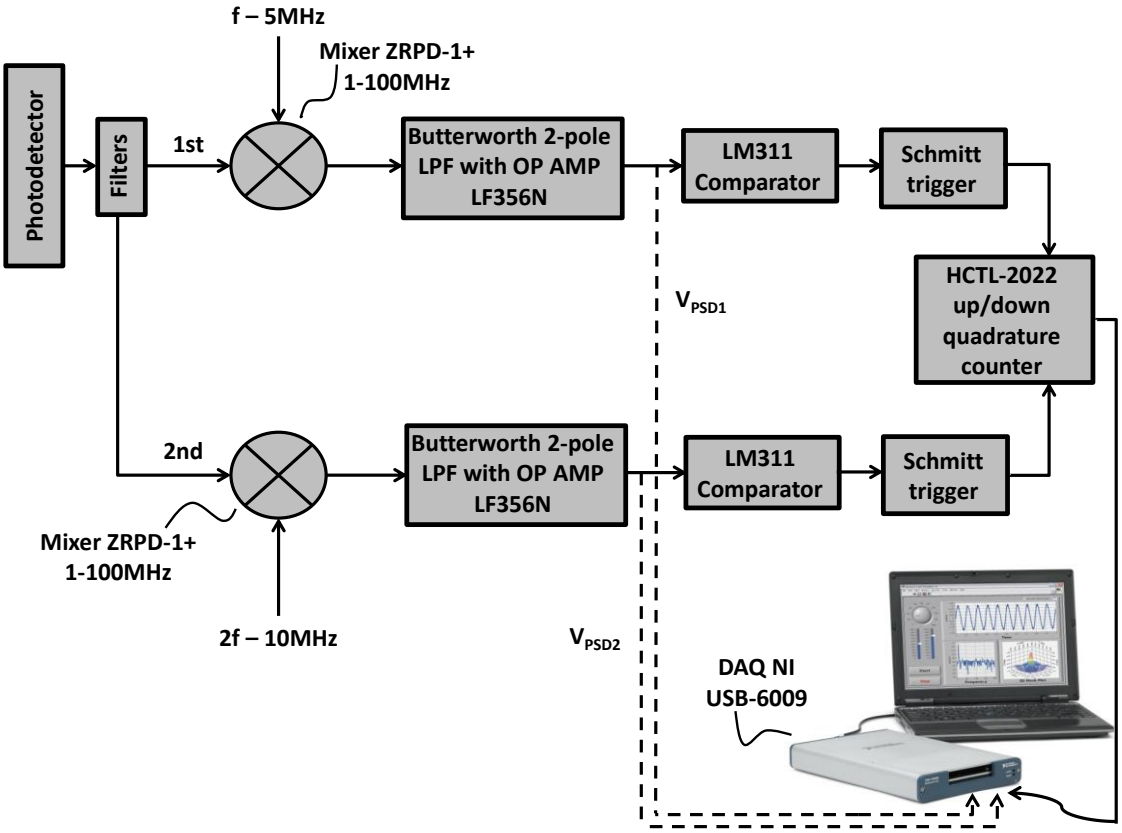

Figure 18. Experimental setup for the PSD before processing the data with Labview [30].

Therefore, the resulting signals for the first and second harmonics after the multiplication detection and low pass filtering were:

$$V_{PSD1} = -\sqrt{P_1}\sqrt{P_2}\,\frac{\beta V_0}{2}\sin(d)\cos(\theta_{ref})$$
$$V_{PSD2} = -\sqrt{P_1}\sqrt{P_2}\,\frac{\beta^2 V_0}{8}\cos(d)\cos(\theta_{ref}) \qquad (3.2.6)$$

In both cases, the mixer outputs were filtered by a low pass filter with a fast roll-off rate, and amplified, to yield phase-sensitive (IQ) measurements of the target displacement. The sinusoidal signals were then run through comparators with Schmitt

triggers to avoid changes due to noise fluctuations along thresholds after squaring the signal.

Fringe Counting Technique

As commented previously, the main difficulties faced in fringe counting are to know the direction of motion and to continuously count fringes and fraction of fringes even in the presence of power fluctuations of the laser.

Due to the limited DAQ device (NI5122) acquisition rate, the counting was done using an ordinary and cheap 32 bit binary up/down 4x fringe counter HCTL2022 that uses quadrature decode logic and was driven by a 10 MHz external clock. This provided the absolute target's displacement (integer counts, M_{int}, resolution up to λ /8). The ability of counting up and down enables easy determining of the direction of motion and its 32 bits permits the user to count up to approximately 4 billion of fringes, which translates into 825 meters. For a Michelson interferometer there is one count every λ /2. Having a 4x counter gave one count (i.e. increases/decreases N by 1) every eighth of wavelength, which for the laser source of 1536nm used for this experiment translated in 192nm of accuracy. However, it had an 8-bit bus interface thus Labview code was necessary in order to read the 32 bit position latch in 4 sequential bytes at a rate fast enough (that is, continuously triggered) to continuously keep track of the fringes. Once the 4 bytes were read, Labview was used to recombine them in a single 32 bits number and transform that to a number of counts M_{int}.

At the same time, the DAQ (NI-5122 14 bits digitizer card) monitored both analog signals for providing digitally the relative target's displacement L, with resolution

more than $\lambda/8$ (M_{frac}). Looking simultaneously at the first harmonic,V_{PSD1}, and second harmonic,V_{PSD2}, has the upside of making the measurements independent of the laser's power variations in time. Since both signals are proportional to the same constants dependent on the power of the laser, dividing one harmonic by the other cancels the dependence on laser power and increases the contrast. Therefore, very conveniently, measurements are not affected by possible fluctuations of the power of the laser or the alignment or fringe contrast of the interferometer. The remaining constant in the equations is directly proportional to an intrinsic characteristic of the EOM (V_π, half wave voltage) and inversely to the amplitude of the sine applied to the EOM (V_0) thus both are known and constant in time and we can solve for the relative target's displacement (fraction of a count, M_{frac}) in the following way:

$$M_{frac} = \theta \times \frac{2}{\pi} = \text{atan}\left(\frac{V_{PSD1}}{V_{PSD2}}\right) \times \frac{2}{\pi} \quad , \tag{3.2.7}$$

where the second term is due to having a 4x counter (yields one count every $\pi/2$ phase).

The two acquired measurements were used to achieve unambiguous and highly accurate measurements of the stage position up to speeds of 8mm/s:

$$dL = \frac{\lambda \times (M_{frac} + M_{int})}{8} \tag{3.2.8}$$

Equation (3.2.7) was implemented in the Labview code using the four-quadrant inverse tangent function, atan2 (y,x) , whose result θ is in radians and lies in the range of $[\pi, -\pi]$. However, when the target is moving towards the positive side, i.e. the number of count M_{fringe} is positive, M_{frac} has to be positive too in order to add both correctly. Moreover, if the target has moved more than $\lambda/8$ (more than a full quadrant, see

Figure 19) the 4x counter accounts for that increasing M_{int} by one, thus the fraction of count M_{frac} should not reflect that completed quadrant. Otherwise, fringes would be counted twice after adding M_{frac} and M_{int}. Figure 19 below shows how these two problems were solved by correcting θ depending on the quadrant. A couple examples are shown to better explain the process.

Quadrant	1	2	3	4
$\boldsymbol{\theta_{corrected}}$	θ	$\theta - {}^{\pi}/_{2}$	$\theta + \pi$	$\theta + {}^{\pi}/_{2}$

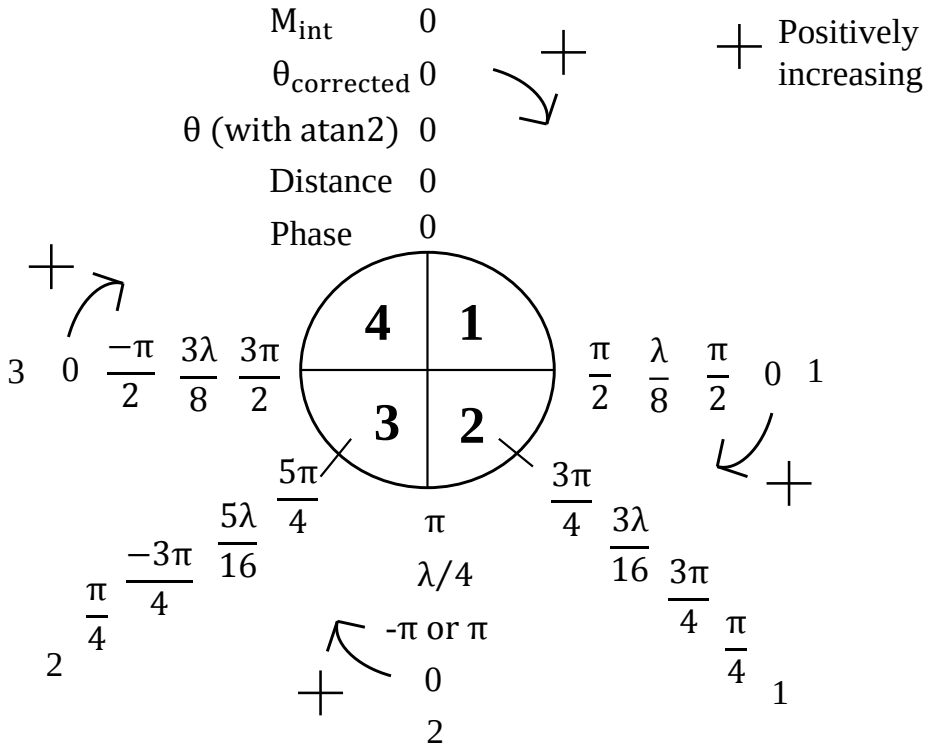

Figure 19. Fringe counting technique with resolution higher than λ⁄8. The figure shows the values of the parameters when the target is moving in the positive direction a distance from 0 to less than λ⁄2 (less than one whole round).

If the distance moved by the target is less than $\lambda/8$, the counter shows 0 and the θ is equal to the portion of the quadrant walked so no correction is necessary for the first quadrant. For example, if the distance moved is $\lambda/16$,

$$\begin{aligned}
&\theta_{corrected} = \theta = \frac{\pi}{4} \rightarrow M_{\,frac\ corrected} = \theta_{corrected} \times \frac{2}{\pi} = \frac{1}{2} \\
&M_{int} + M_{\,frac\ corrected} = 0 + \frac{1}{2} = \frac{1}{2} \\
&\mathrm{dL} = \frac{\lambda \times (\mathrm{M}_{\mathrm{frac\ corrected}} + \mathrm{M}_{\mathrm{int}})}{8} = \frac{\lambda}{16} \rightarrow CORRECT
\end{aligned} \tag{3.2.9}$$

However, if the distance moved is more than $\lambda/8$ and less than $\lambda/4$ (second quadrant), then theta has to be corrected by subtracting $\pi/2$ to yield the right result. For instance, if the distance moved is $3\lambda/16$,

$$\begin{aligned}
&\theta = \frac{3\pi}{4} \rightarrow\ M_{\,frac} = \theta \times \frac{2}{\pi} = \frac{3}{2} \\
&M_{int} + M_{\,frac} = 1 + \frac{3}{2} = \frac{5}{2}\ fringes \\
&\mathrm{dL} = \frac{\lambda \times (\mathrm{M}_{\mathrm{frac\ corrected}} + \mathrm{M}_{\mathrm{int}})}{8} = \frac{5\lambda}{16} \rightarrow INCORRECT
\end{aligned} \tag{3.2.10}$$

$$\begin{aligned}
&\theta_{corrected} = \theta - \frac{\pi}{2} = \frac{\pi}{4} \rightarrow M_{\,frac\ corrected} = \theta_{corrected} \times \frac{2}{\pi} = \frac{1}{2} \\
&M_{int} + M_{\,frac} = 1 + \frac{1}{2} = \frac{3}{2} \\
&\mathrm{dL} = \frac{\lambda \times (\mathrm{M}_{\mathrm{frac\ corrected}} + \mathrm{M}_{\mathrm{int}})}{8} = \frac{3\lambda}{16} \rightarrow CORRECT
\end{aligned} \tag{3.2.11}$$

Similarly, the needed correction for θ when the distance moved by the target is in between $\lambda/4$ and $3\lambda/8$ (i.e. quadrant 3) and in between $3\lambda/84$ and $\lambda/2$ (i.e. quadrant 4) were found to be $\theta + \pi$ and $\theta + \pi/2$ respectively (see Figure 19).

This measurement of the stage position was stored with the correspondent timestamp allowing comparison with the LADAR measurement to test its accuracy as described later.

To summarize, the uniqueness with respect to other fringe counting techniques widely used in metrology is that this technique does not require any extra detectors, allows knowing the direction of motion without extra measurements and continuously and unambiguously measures fringes and fraction of fringes giving a resolution higher than the usual $\lambda/4$.

Steady Target Measurements

A common practice to determine the stability of a system is to take the standard deviation of a data set. However, for the standard deviation to be a valid representation of the stability, the data has to be stationary. Stationary data is time independent and its noise generally does not rise near DC. Some noise types show up because of the reference and the measurement system itself and they can be removed by averaging. The Allan deviation is a non-classical statistic approach to calculate the frequency stability of a system in the time domain and tell if it can be improved by increasing the averaging period (smoothing). By definition the standard deviation subtracts the mean from each measurement before squaring their summation while the Allan deviation subtracts the previous data point removing the time dependent noise [31].

For a 30 minutes measurement with a steady target, the results show a standard deviation of 24 nm from the initial position (see Figure 20(top)). The minimum Allan Deviation for reference resulted to be 4 nm (see Figure 20(bottom)), which means that

the difference with the standard deviation of the results (≈20 nm) was due to air density fluctuations of the path length. Allan Deviation statistics also showed that the stability would not improve significantly by increasing the averaging period for a constant rate of acquisition data of 10 Hz.

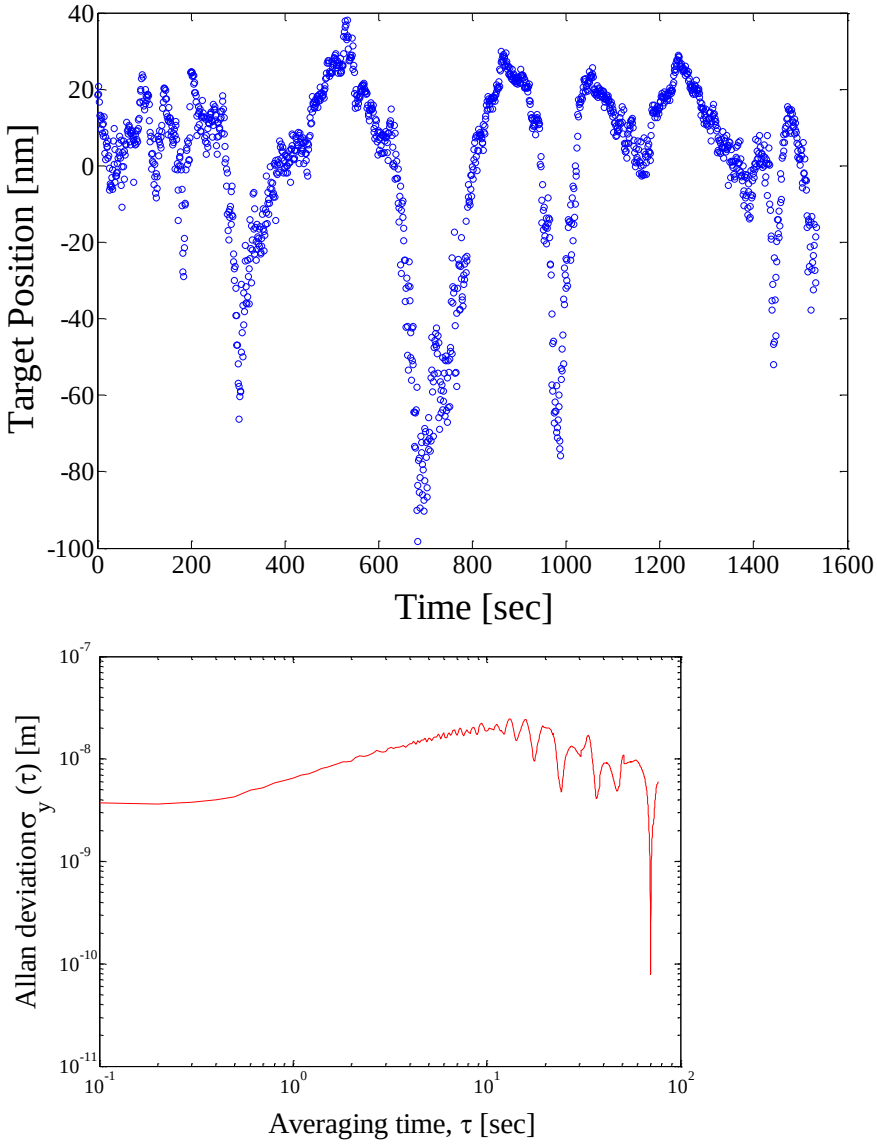

Figure 20. (top) Steady target measurements with the interferometer setup using lock-in detection and fringe-counting technique. (bottom) Allan deviation versus the average period **τ**. The lack of negative slope at the beginning of the curve means that more averaging would not help for this data.

Although the stability could be improved by measuring the index of refraction of the room every few seconds and taking the variations into account, the purpose of this interferometer is to compare measurements with the FMCW Ladar system and as both systems operate at the same wavelength the air fluctuations would cancel.

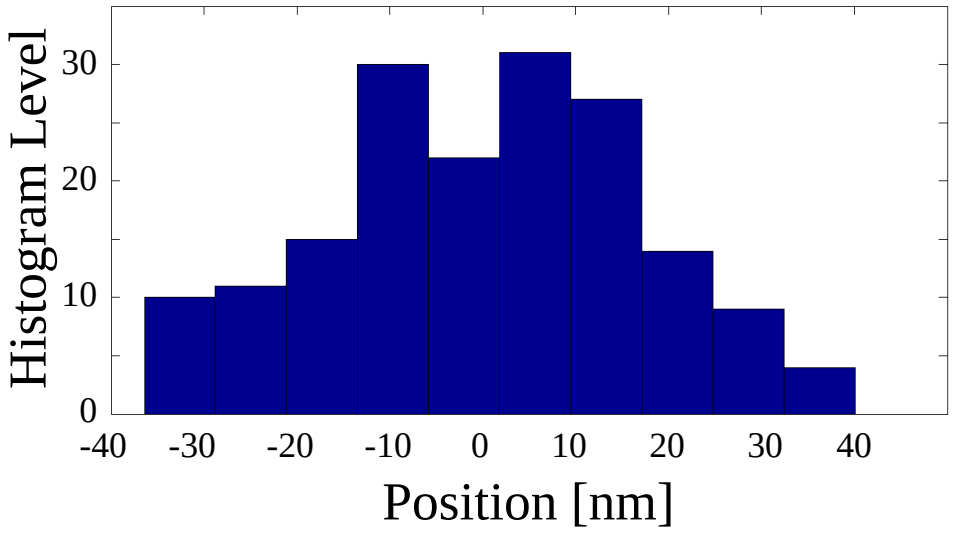

Figure 21. Histogram plot for a different set of stationary data with standard deviation of 17 nm.

Comparison

Once the chirp rate of the FMCW was measured, the system was used to demonstrate one dimensional metrology. To test the accuracy of this measurement, the displacement of the target was measured simultaneously with the CW interferometer. These synchronized measurements were taken sweeping the laser along different wavelength regions for a steady target at a fixed point of the stage first (precision measurements), and a steady target positioned at different points of the stage in second place (accuracy measurements). Then, measurements with non-cooperative targets were

taken in the chirping region where the system showed the best performance. The results are presented below.

Steady Cooperative Target at a Fixed Point of the Stage

Minimizing air fluctuations as much as possible, positioning the reference mirror as close as possible to the cooperative target (mirror) and keeping the latter steady, measurements were taken simultaneously with the CW interferometer and the FMCW LADAR setups described in the previous sections (see Figure 17, Figure 18 and Figure 10).

Sweeping the laser from 1535 nm to 1565 nm and grabbing data during a period of 8 minutes, the standard deviation for the chirped laser and the interferometer were 0.17 μm and 0.01 μm respectively (see Figure 22). As the rate for data acquisition of the interferometer is much larger, algorithms were used to find synchronous measurements. Then, comparison between the mean of four interferometer measurements and the corresponding single chirped LADAR measurement led to a standard deviation of 0.17 μm.

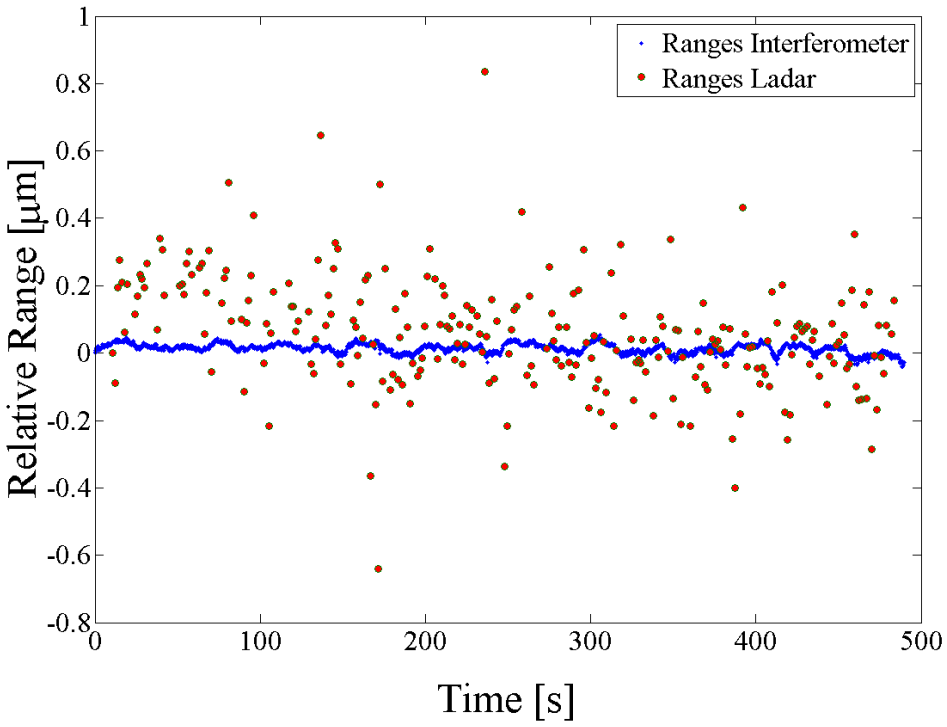

Figure 22. Relative displacements of a "steady" target obtained with the interferometer (blue) and the chirped laser (red) swept from 1535 nm to 1565 nm.

Then, the same measurements were repeated sweeping the laser from 1570 nm to 1600 nm (see Figure 23). This time data was grabbed during a longer period (≈ 20 minutes) and, as expected, the standard deviations appear to be better than at longer wavelengths (Table 1) as well as the comparison between the mean of four interferometer measurements and the corresponding single chirped LADAR measurement, which led to a standard deviation of 0.09 μm for this case. The drifting observed in the LADAR points is likely due to the fiber sensitivity to changes in temperature, which could be solved by an active temperature control in the laboratory as indicated in [25] or by measuring the temperature of the fiber as a function of time and calibrating out the fluctuations..

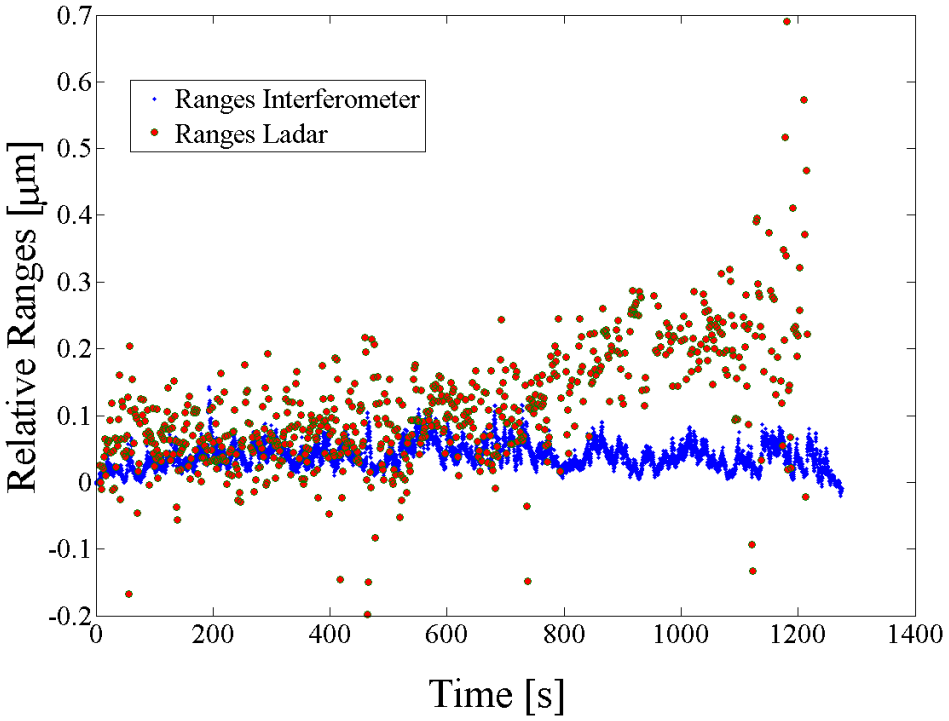

Figure 23. Relative displacements of a "steady" target obtained with the interferometer (blue) and the chirped laser (red) swept from 1570 nm to 1600 nm.

	Standard Deviation [µm]	
Chirp region [nm]	CW Interferometer	FMCW LADAR
1535-1565	0.01	0.17
1570-1600	0.02	0.09

Table 1. Standard deviations for measurements taking with a steady target.

Steady Cooperative Target Positioned at
Different Points of the Stage

Synchronized measurements were taken moving the target along the Zaber motor track controlled electronically for 2 cycles of 30 cm forward motion then 30 cm back to original position in 2 cm steps. This measurement was performed for the 1535-1565 nm calibrated with HCN (see Figure 24 and Figure 25) and the 1570-1600 nm wavelength regions calibrated with CO (see Figure 26 and Figure 27).

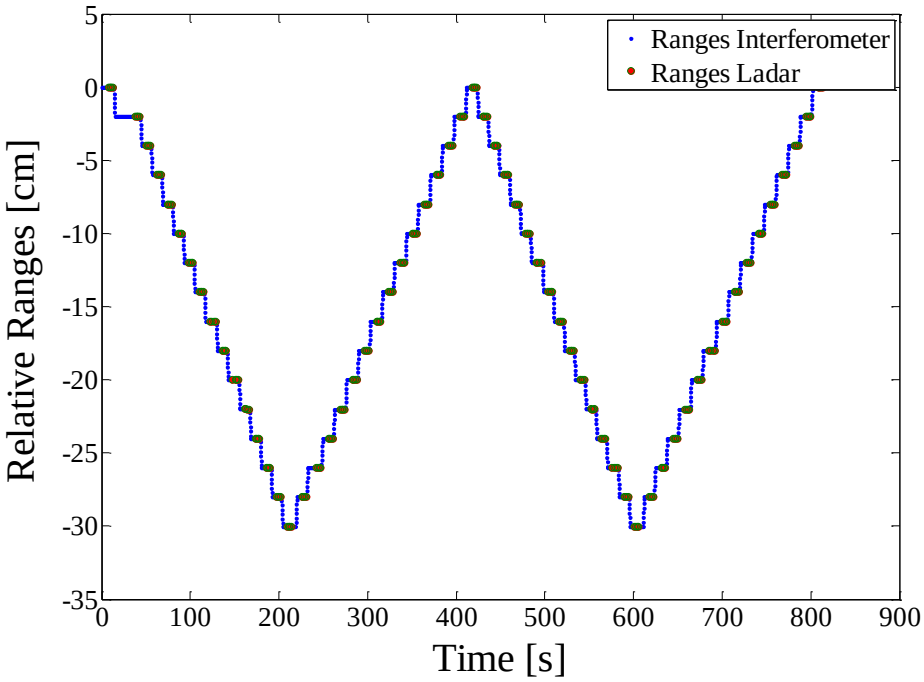

Figure 24. Measurements with target moving along 30 cm. (top) Relative ranges. It is easily observed that calibration is causing the 'w' shape in the bottom figure.

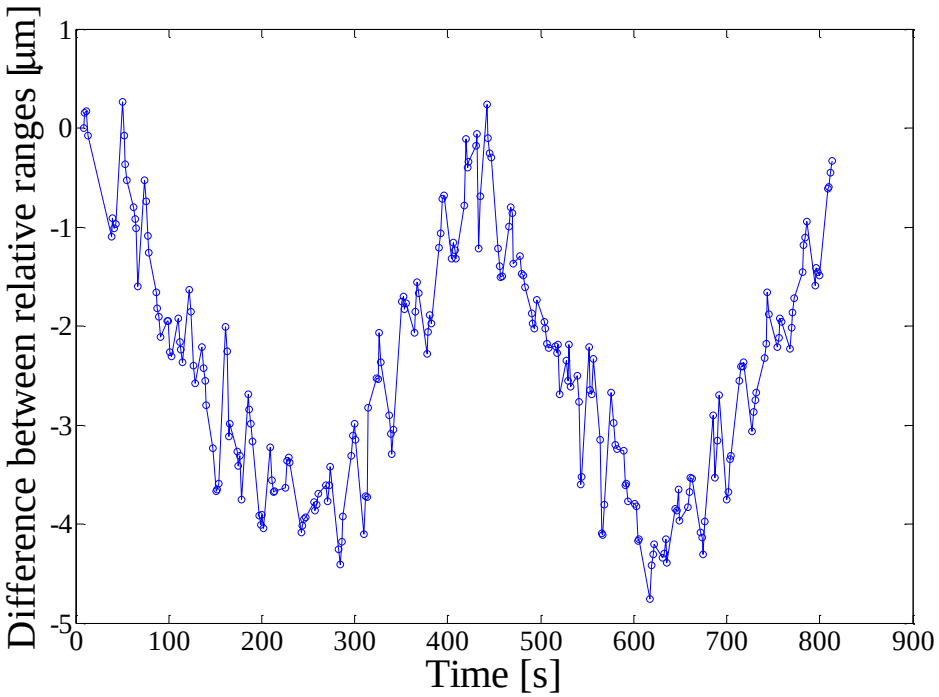

Figure 25. Difference between interferometer and chirped laser from 1535 nm to 1565 nm and HCN calibration. A maximum deviation of ~4 μm for along 30 cm gives a fractional deviation of 13 ppm.

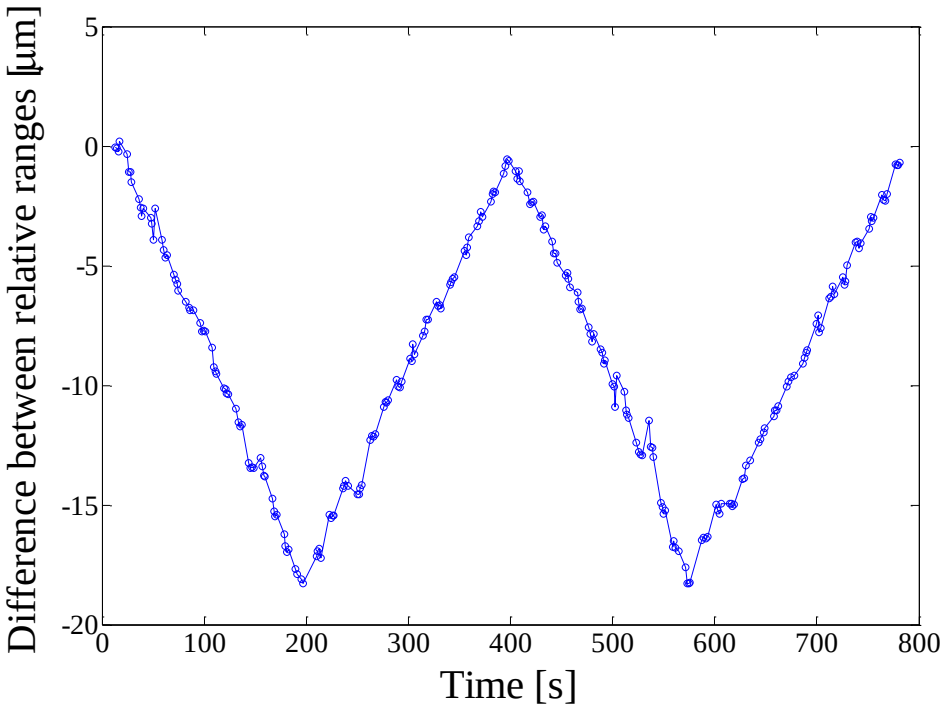

Figure 26. Difference between interferometer and chirped laser from 1570 nm to 1600 nm using CO calibration.

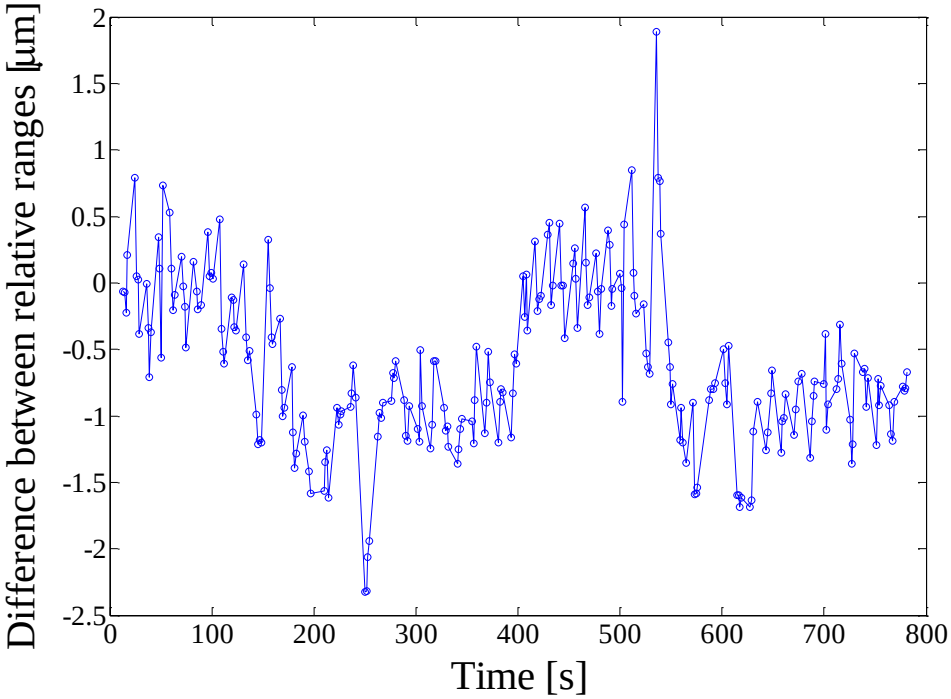

Figure 27.Difference between interferometer and chirped laser from 1570 nm to 1600 nm modifying the chirp calibration factor to minimize the deviation.

The clear “W” shape of the residuals observed in the figures above indicates that the calibration of the CW interferometer and the FMCW LADAR system are not consistent, suggesting improvement of the calibration of the FMCW LADAR system using the optical frequency comb method [25] would be beneficial. In addition to this, comparing the fractional deviations represented in Table 2 to the standard uncertainty of calibrations with HCN and CO indicates that there is an additional discrepancy in range scale calibration unaccounted by the uncertainty in the molecular calibrations.

Chirp region [nm]	Calibration process	Fractional Uncertainty in Calibration	Measurements Max Deviation [μm]	Measurements Fractional Deviation
1535-1565	HCN cell	2 ppm	4	13 ppm
1570-1600	CO cell	10 ppm	18	60 ppm
1570-1600	Best Scale	-	2	6 ppm

Table 2. Standard deviations of the difference between the interferometer and the LADAR measurements with a moving target.

A potential issue could have been a calibration error of the wavemeter that is used to measure the wavelength of the laser used in the CW interferometer. We tracked the wavelength with two different wavemeters at the same time to get to a discrepancy of only 1 ppm. The dispersion due to air between the two wavelengths should only give an approximately 20 ppb shift according to the Ciddor equation or to an updated version of the Edlen equation [32]–[34]. Another issue could have been a clock timing error of the ADC card used to capture the FMCW LADAR data. When comparing this clock with a reliable source, a difference of 50 Hz was found between them. However, as the same digitizer card is used for calibrating the system and taking measurements, the off-clock effect cancels, which in fact can be appreciated as an advantage of the system’s setup.

Although a discrepancy in the parallelism of the CW interferometer and FMCW LADAR beams before hitting the target could be an issue, a realistic deviation per meter would give less than 1 ppm deviation in the results. Summarizing, all the possible issues under consideration could not explain the discrepancy in the results presented in Table 2. The significant increase in error between the HCN and CO measurements indicates a calibration issue. As explained before, during the calibration process the frequencies are fitted to a quadratic polynomial in order to find the chirp κ (linear coefficient of the fit). According to [27], the quadratic coefficient was smaller than 1 ppm. However, while checking this issue the difference between the κ resulting from a linear fit and the the κ resulting from a quadratic fit during the calibration process was in the order of 10 ppm for the HCN cell and 100 ppm for the CO cell. This could probably be the source of the discrepancies in Table 2 although further experiments carefully controlling the calibration process would need to be performed in order to confirm it.

Steady Non-Cooperative Target at a Fixed Point of the Stage

As shown above, the FMCW LADAR system appeared to work better for a steady target when swept in the 1570-1600 nm wavelength region. Keeping this chirp region, rearrangements were made in the setup for the FMCW LADAR system to hit a) the mirror´s mount (anodized aluminum) and b) a section of the mirror painted with white spray paint. In this way, the desired comparison was possible since the target was always shared by the FMCW LADAR and the CW interferometer systems, being non-cooperative for the first and still a mirror for the later.

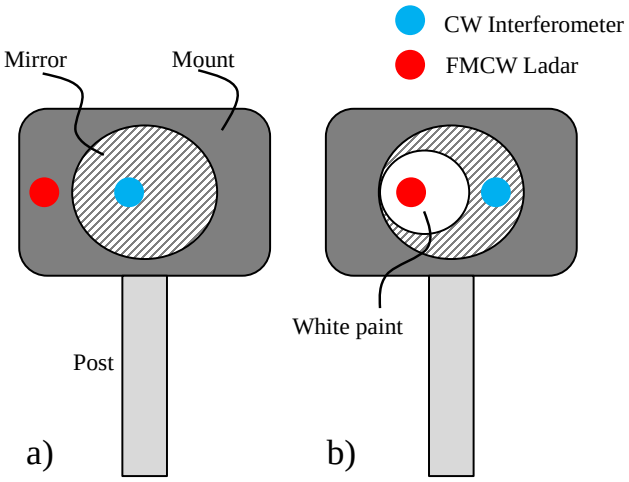

Figure 28. Target setup for non-cooperative target measurements with the FMCW LADAR system.

The SNR decreased approximately by 40 dB with the use of the non-cooperative target, which can be seen in Figure 30.

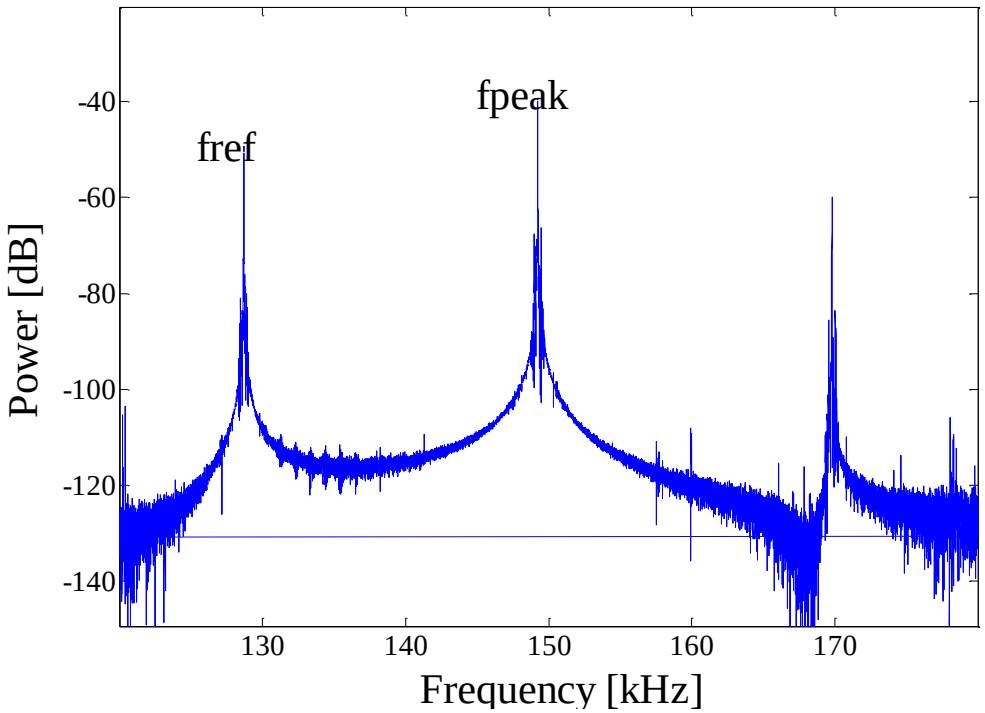

Figure 29. Power(dB) vs Frequency (Hz) plots for cooperative target (SNR~90dB)

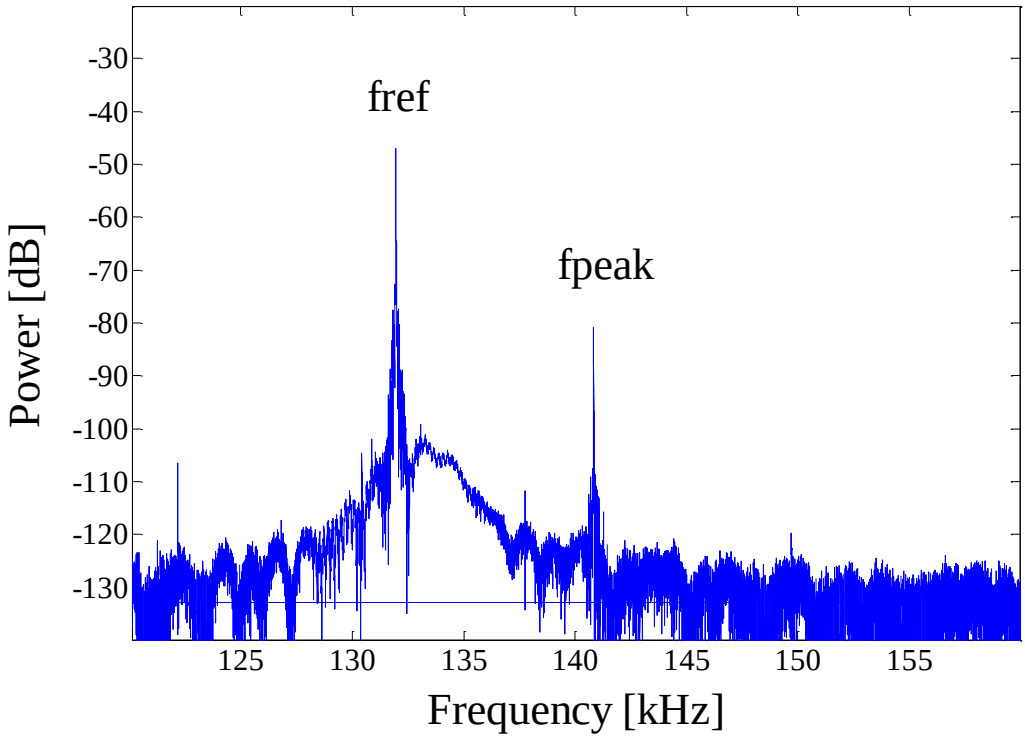

Figure 30. Power(dB) vs Frequency (Hz) for non-cooperative target (SNR~50dB).

However, the returning signal´s power was still more than enough to analyze the target. As done for the cooperative target, comparison between the mean of four interferometer measurements and the corresponding single chirped LADAR measurement is made leading to a standard deviation of 0.16 μm for the mount and 0.17 μm for the paint. The results are summarized in Table 3 including the ones presented previously for the steady Cooperative target.

	Steady Target		Standard Deviation [µm]	
Synchronized measurement	CW Interferometer	FMCW LADAR	CW Interferometer	FMCW LADAR
#1	Mirror	Mirror	0.02	0.09
#2	Mirror	Mount	0.04	0.15
#3	Mirror	Paint	0.03	0.17

Table 3. Chirp region 1570-1600 [nm].

Steady Non-Cooperative Target Positioned
at Different Points of the Stage

While sweeping the FMCW laser along the 1570-1600 nm region, synchronized measurements were taken translating the non-cooperative targets along the Zaber stage. The uncertainty in the chirp constant $d\kappa$ found in the calibration with the CO cell prior to the measurements is compared with the corresponding fractional deviation in Table 4 including the results for steady cooperative target presented before. The bad result obtained when tracking the mount as the target is considered to be due to the irregularities on its surface, as well as to the lack of complete flatness.

		Steady Target		FMCW LADAR Calibration Process	Fractional Uncertainty in Calibration	Measurements Fractional Deviation
		CW Interferometer	FMCW LADAR			
Synchronized measurement	#1	Mirror	Mirror	CO cell	10	60 ppm
				Best scale	-	6 ppm
	#2	Mirror	Mount	CO cell	9 ppm	143 ppm
				Best scale	-	121 ppm
	#3	Mirror	Paint	CO cell	9 ppm	37 ppm
				Best scale	-	14 ppm

Table 4. Chirp region 1570-1600 [nm]

To summarize, comparison with another length metrology method, that is the CW interferometer, has shown the one dimensional ranging capability of the FMCW LADAR system to be ~90-160 ppb for a steady target at a fixed point of the stage (system's precision) and ~6.5-14 ppm for a steady target displaced to different points of the stage (system's accuracy). The later strongly depends on how well things are calibrated which means the system's accuracy could get as good as 90-160 ppb with the right calibration method even for non-cooperative targets.

2D TRILATERATION SYSTEM USING FMCW LADAR

Overview

To perform two dimensional metrology of diffuse-reflecting non-cooperative targets we proposed and constructed the optical setup shown in Figure 31. Using a stabilized chirped laser as a source, two emitters, one scanning emitter/receiver and heterodyne coherent auto-balanced detection, diffuse targets were scanned giving a two dimensional profile of their surface. The MATLAB code built to process the data is described in detail including an explanation of the consequence of speckle on the full profile of the target and how to mitigate it.

A low resolution chirp laser (B=76.6 GHz) was used first to test and initially calibrate the system because of its ability to speed up collecting the data. Once everything was working correctly, a much higher resolution laser (B=1.8 THz) was employed to get a full profile of a variety of diffuse targets.

The error analysis of the results show a bigger uncertainty than expected and proved that this scatter could be greatly diminished by achieving a better calibration of the position of the emitter B using the trilateration system itself. Finally, a detailed analysis of the system's photon budget is presented, giving numerical values for the number of photons emitted/collected by the system in the coherent integrated time, CNR, SNR, etc.

Setup

A stabilized chirped laser source emits a beam that is first split into a 90% path transmission to the target (Tx) and a 10% path that forms the Local Oscillator path (LO). The latter is used as a reference to mix with the returned signal (Rx) providing coherent optical gain of the optical information to the RF regime and allowing auto-balanced detection. Next, the Tx path is split again with a proportion 99.99/0.01%. This unusual Comcore customized high ratio splitter serves many purposes as will be shown later in this chapter.

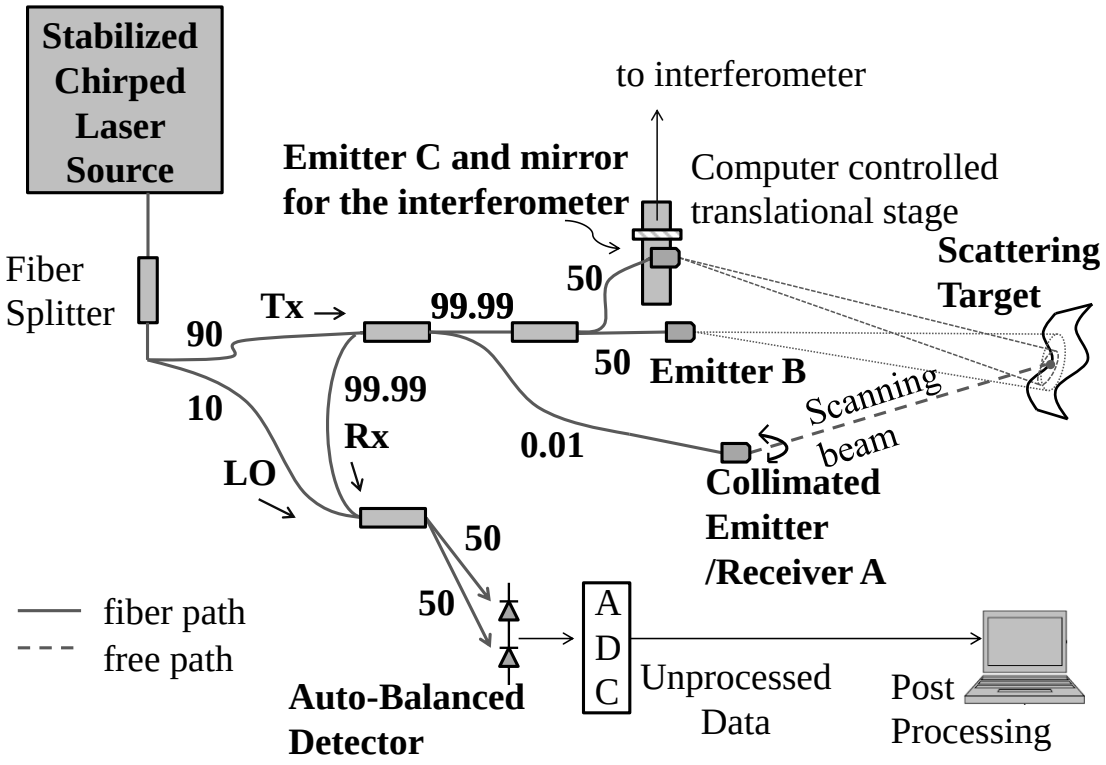

Figure 31. Experimental setup for 2D metrology of non-cooperative targets.

The lowest power output (0.01%) is directed to the emitter optics labeled A. The output transmit beam of A is very well collimated thanks to a "triple" collimator that uses

air-spaced triplet lenses producing a beam quality superior to aspheric lens collimators (less divergence, less wavefront error). The output of emitter A is focused on a small spot on the target with additional optics. Concretely, these optics are a concave and a convex lenses of equal and opposite focal length $|f_1| = |f_2|$ positioned in a slotted lens tube that allows the distance d between these two lenses to vary (see Figure 32).

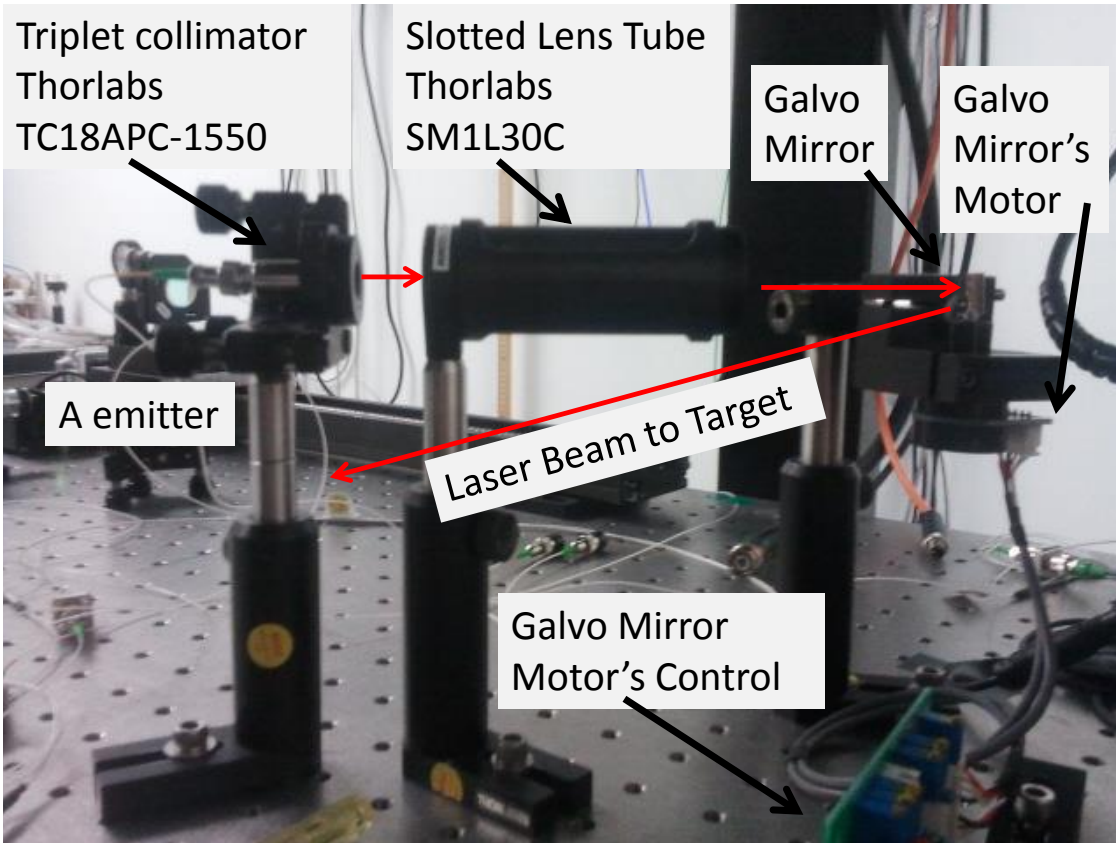

Figure 32. Setup for the A emitter.

As the thickness of the lenses used was negligible compared to their radii of curvature, the thin lens approximation equation to calculate the focal length F of the combined system could be used:

$$\frac{1}{F}=\frac{1}{f_1}+\frac{1}{f_2}-\frac{d}{f_1 f_2}, \tag{4.2.1}$$

which for this case where $|f_1|=|f_2|=f$ results in:

$$F=\frac{f^2}{d} \tag{4.2.2}$$

Adjusting d moving one lense inside of the slotted lense tube permits to vary F and consequently, change the position the target at different distance F of the emitters for different measurements, having the emitter A beam focused on the target at all times.

Also, while the power of this beam is concentrated on a small spot, because it is low in power it does not cause any damage on the target and, more importantly, it is eye safe for the wavelength of use in this work. This last feature was double checked calculating the maximum permissible exposure (MPE) for point source ocular exposure to a laser beam according to the American National Standard for Safe Use of Laser [35]. Given the beamwidth of our laser is under the limiting aperture for 1.55 microns (3.5 mm), its size does not affect the calculation and the MPE's units are Watts. A $\lambda = 1550\ nm$ laser beam yields a $MPE = 9.6\ mW/cm^2$ for Class 1 (i.e. to be safe under all conditions of normal use). As the power transmitted by A is in the order of $\sim 44\ \mu W$, the beam is 100% eye safe.

The emitter A is also used as the main receiver for the light emitted by A and returning along the same path after hitting the target (D_{aa}), but also for the light emitted by B (D_{ba}) and C (D_{ca}) as can be seen in Table 5. The emitter/receiver A has a computer controlled galvo-mirror to allow scanning of the target.

The high power output of the 99.99/0.01% splitter is directed thoruhg a 50/50 coupler to the emmiters B and C, which for this table top setup are merely bare fibers (diameter $\pi\omega_0 = 10.5\ \mu m$) which allow the beams to diverge rapidly (see how Equation (2.3.3) relates ω_0 and the divergence θ) . These beams will be eye safe at a distance from the emitters with an intensity equal or smaller than $MPE = 9.6\ mW/cm^2$. For a transmitted power of 221 mW and using Equation (2.3.1) this condition is met at a distance of 40 cm. Therefore, this configuration allows these beams to obey eye safety restrictions at a minimum distance of 40 cm from the emitters (considered Class 1 according to [35]) and assures that the target is illuminated with minimal directing needed for the beam. The emitter B is fixed to the optics table and C is placed on the previously described Zaber stage allowing translation in one direction. The origin of coordinates for the system is defined at one end of this Zaber stage to facilitate the calibration process. The relative displacement of C along the stage is tracked at all times with the CW interferometer setup described in section 3.2.

The light emitted by A, B and C is returned from the target and collected by receiver A. Finally, a 2x2 splitter directs the output of the 99.99% splitter onto the two ports of the auto-balanced detector, this nearly all of the light received by A along the Rx path efficiently reaches the auto-balanced detector, maximizing the SNR of the experiment.

The auto balanced detector output signal is converted to digital using the digitizer card NI-5122 described in section 3.2. Then, the collected data is processed on the computer using algorithms implemented using MATLAB code.

The digitized signal is first masked with a Hanning Fourier window to minimize the side-lobe level. The use of the Hanning window has the effect of reducing the CNR of the signal by 3 dB and broadening the peak width at 3 dB by a factor of 2 (i.e. $\Delta R_{Hanning} = \Delta R \times 2$). Then, a scaled Fourier transform is used to select the data region of interest resulting in a frequency spectrum similar to that shown in Figure 33.

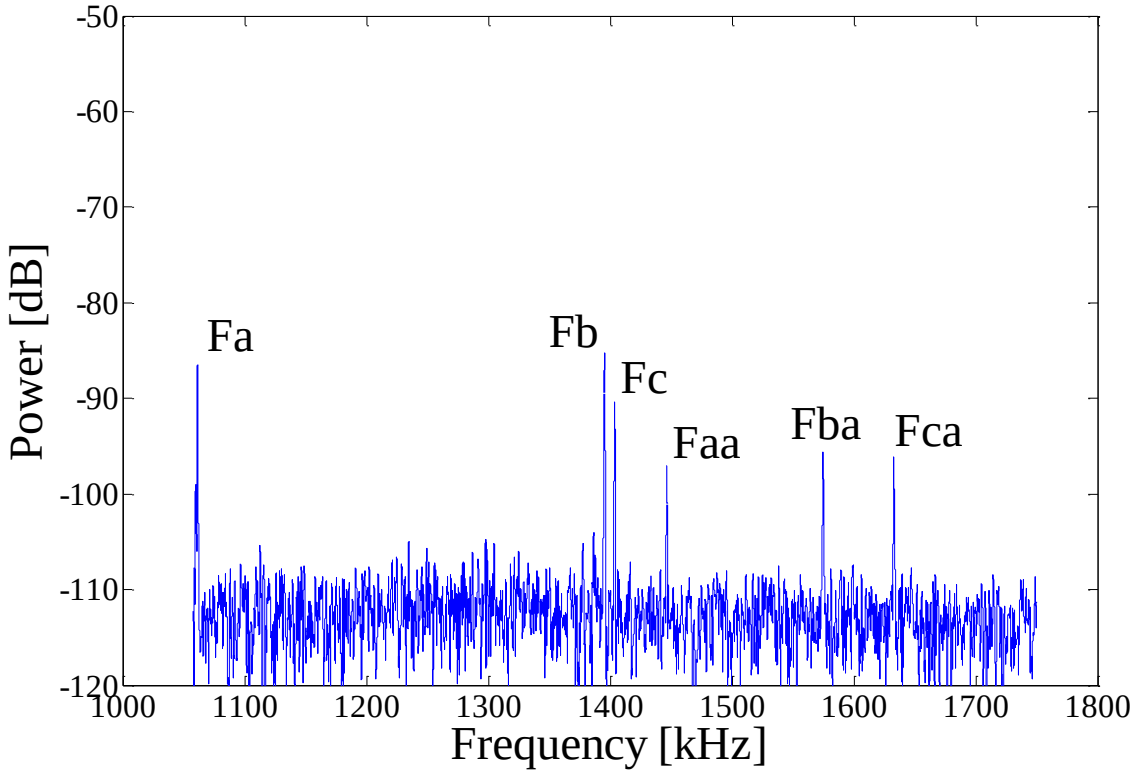

Figure 33. Detected peaks in frequency domain using the DFB laser as the source. The correspondence in the range domain is explained in Figure 37 and Table 5.

Besides the system efficiency, any coherent LADAR scattered signal from a diffuse target (see target classification discussion in photon budget analysis section) presents a granular spatial structure as the result of coherent waves scattering from points on the target interfering with each other [36]. This target-induced interference

phenomenon is called speckle effect and takes place when the target's surface is rough on scale of an optical wavelength of the system's source (which most of the targets are, both handmade and natural) [37]. The speckle effect is observed by the human eye as a chaotic and unordered pattern of bright and dark spots, adding a significant excess of uncertainty while mapping a surface of a target and making it a strong limit on the achievable range uncertainty/precision [16]. Although suppressing the effects of speckle in coherent imaging systems preserving image detail at the same time is still an unsolved problem [37], it has been shown that speckle can be significantly reduced with increased optical bandwidth [16]. For the goals of this thesis, speckle phase noise proved to be a challenge and special care was taken choosing the target's surfaces and removing the outlier points of data that could be detected.

While performing trilateration experiments, it was sometimes noticed that one peak or more would show up with a double tip, probably due to the speckle effect. In the worst case, i.e. for a phase jump of π due to speckle destructive interference, there would be a node in the beat frequency as shown in Figure 35.

The speckle pattern changes phase with λ and therefore distance. To mitigate its effects we found it useful to divide the collected data in three equal sized pieces, taking individual FFTs of the pieces and incoherently averaging them.

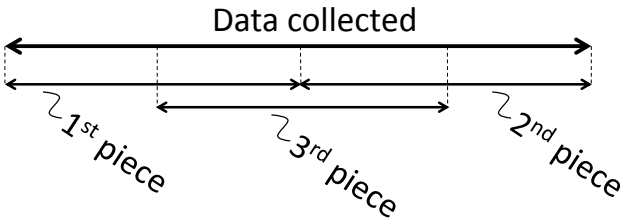

Figure 34. Dividing collected data in three equal sized pieces as the first step to mitigate speckle effect.

In this way, each piece of data would have a different realization of the speckle at f_{beat} and the superposition would help cancelling the phase modulation effect. However, the repercussion was reducing the range resolution again by a factor of 2:

$$\Delta R_{data\ division+Hanning} = \Delta R_{Hanning} \times 2 = \Delta R \times 4 \tag{4.2.3}$$

Therefore, the range resolutions corresponding to the DFB and BP lasers used for the measurements in this chapter can be obtained from their bandwidth B by combining Equations (2.1.14) and (4.2.3):

$$\begin{aligned} \Delta R_{DFB} &= \frac{c}{2B_{DFB}} \times 4 = 7.8\ mm \\ \Delta R_{BP} &= \frac{c}{2B_{BP}} \times 4 = 329\ \mu m \end{aligned} \tag{4.2.4}$$

In addition to this, the center of mass of the peak was used instead of Gaussian fitting the maximum to get the corresponding frequency value f_{beat}.

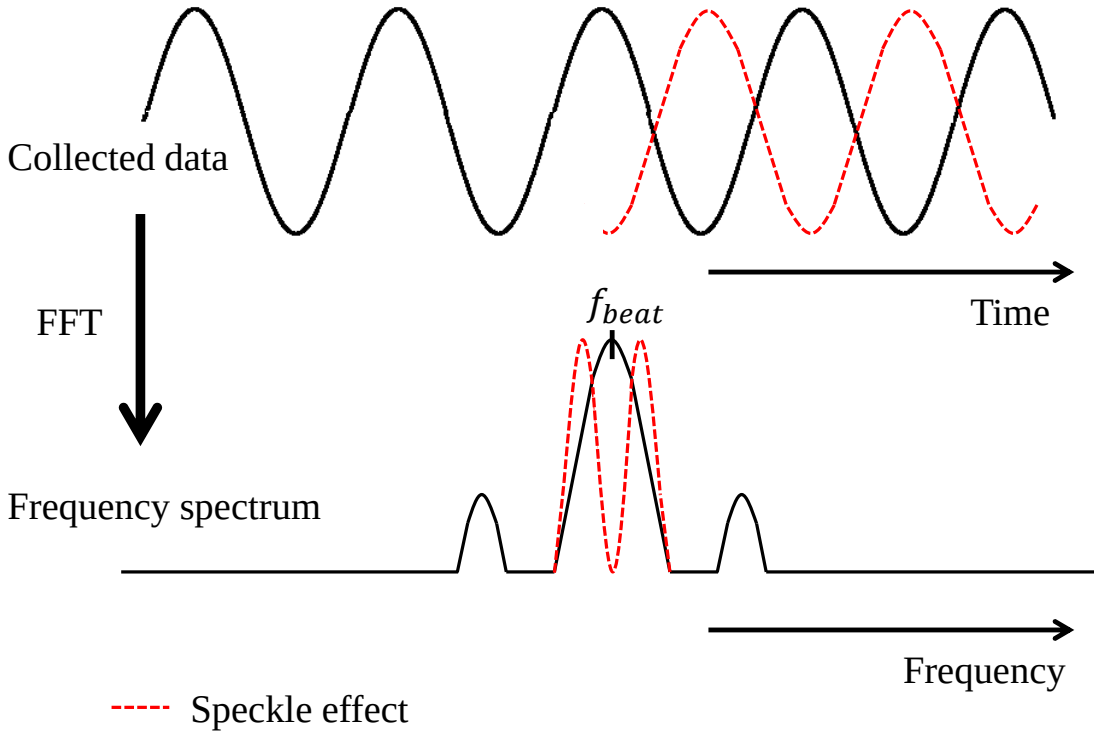

Figure 35. Sketch of the worst case scenario for a phase jump of π in the collected data due to destructive speckle interference.

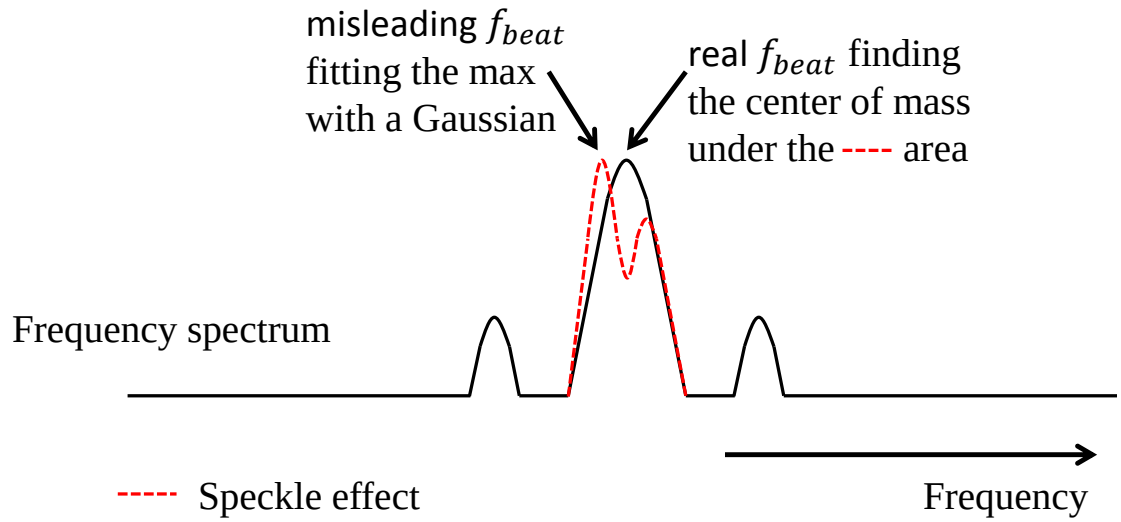

Figure 36. Different methods to obtain f_{beat}.

The different detected signals are identified in this frequency domain, and the corresponding and desired equivalents in range calculated using the already known relation:

$$R = \frac{c \times f}{2 \times \kappa}, \tag{4.2.5}$$

where the index of refraction is assumed to be 1 to simplify as it is only a scale factor in the order of 0.03%.

Defining the length of the fibers as shown in Figure 37 the resulting measurements of interest are summarized in Table 5.

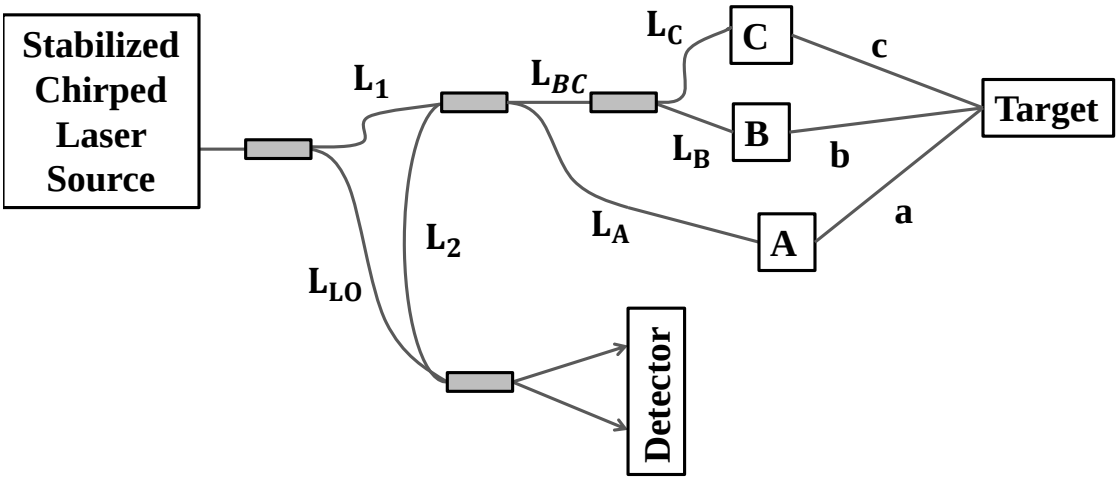

Figure 37. Experimental setup for 2D metrology with 3 emitters (A,B,C) and 1 receiver (A) showing the length fibers L and the free space distances a,b and c.

Signal Name				
Frequency Domain	Range Domain	Emitted by	Received by	Range measured
F_{aa}	D_{aa}	A	A	$2L_A + 2a + L_{net}$
F_a	D_a	Reflection from A fiber tip		$2L_A + L_{net}$
F_{ba}	D_{ba}	B	A	$L_{BC} + L_B + b + a + L_A + L_{net}$
F_b	D_b	Reflection from B fiber tip		$2L_{BC} + 2L_B + L_{net}$
F_{ca}	D_{ca}	C	A	$L_{BC} + L_C + c + a + L_A + L_{net}$
F_c	D_c	Reflection from C fiber tip		$2L_{BC} + 2L_C + L_{net}$

Table 5. Resulting range or distance measurements D from the trilateration setup. L_{net} is defined to be $L_1 + L_2 - L_{LO}$.

To get the desired distance measurements, m_1 and m_2 are defined as follows:

$$\begin{aligned} m_1 &= D_{ba} + D_{ca} - \frac{1}{2}D_b - \frac{1}{2}D_c - D_{aa} = b + c \\ m_2 &= D_{ba} - D_{ca} - \frac{1}{2}\left(D_b - D_c\right) = b - c\,, \end{aligned} \tag{4.2.6}$$

and then,

$$\begin{aligned} a &= \frac{D_{aa} - D_a}{2} \\ b &= \frac{m_1 + m_2}{2} = D_{ba} - \frac{1}{2}D_b - \frac{1}{2}D_{aa} \\ c &= \frac{m_1 - m_2}{2} = D_{ca} - \frac{1}{2}D_c - \frac{1}{2}D_{aa} \end{aligned} \tag{4.2.7}$$

As shown below, the target's position is fully determined by the absolute distances b, c and the relative position of the emitters B and C respect to the 2D coordinate system of choice. Therefore, the possible error on the distance a due to the scanning movement of emitter/receiver A does not affect the results of this experiment.

To facilitate the math, the origin of the coordinate system is chosen to be at the far end of the Zaber stage as shown in Figure 40. In this way, as the C emitter is constrained

to move along the stage, the x-coordinate of its position (C_x) is always zero while the y-coordinate (C_y) is given by the CW interferometer with a resolution higher than $\lambda/8$.

Calibration Process to Find
the Position of the B Emitter

The position of the B emitter was found using several different calibration methods using the trilateration system itself described in this chapter. Firstly, we would have the emitter A looking at a fixed point (P_{x_1}, P_{y_1}) on the target surface. Then, C was moved along different positions along the Zaber stage and the c and b distances were measured for each of them. Apart from computer controlling the distance moved by the transmitter C on the y-direction, we also tracked it with the interferometer in order to have the best possible value for C_{y_2}.

Once $c_{1,1}$, $c_{2,1}$, C_{x_1}, C_{y_1}, C_{x_2} and C_{y_2} are known, the intersection of the circle with origin at (C_{x_1}, C_{y_1}) and radius $c_{1,1}$ with the circle with origin at (C_{x_2}, C_{y_2}) and radius $c_{2,1}$ determines the position of the target (P_{x_1}, P_{y_1}) by solving:

$$\begin{aligned} \left(P_{x_1} - C_{x_1}\right)^2 + \left(P_y - C_{y_1}\right)^2 &= {c_{1,1}}^2 \\ \left(P_{x_1} - C_{x_2}\right)^2 + \left(P_y - C_{y_2}\right)^2 &= {c_{2,1}}^2 \end{aligned} \tag{4.2.8}$$

This system has two possible solutions. As said before, the two solutions can be reduced to one by the use of a third emitter. For this system though, a simple algorithm selecting the solution with a positive P_x was sufficient due to the geometry of the experiment. Then, moving the A emitter beam to another spot on the target (P_{x_2}, P_{y_2}), the same process was done again to obtain (P_{x_2}, P_{y_2}) as shown in Figure 38.

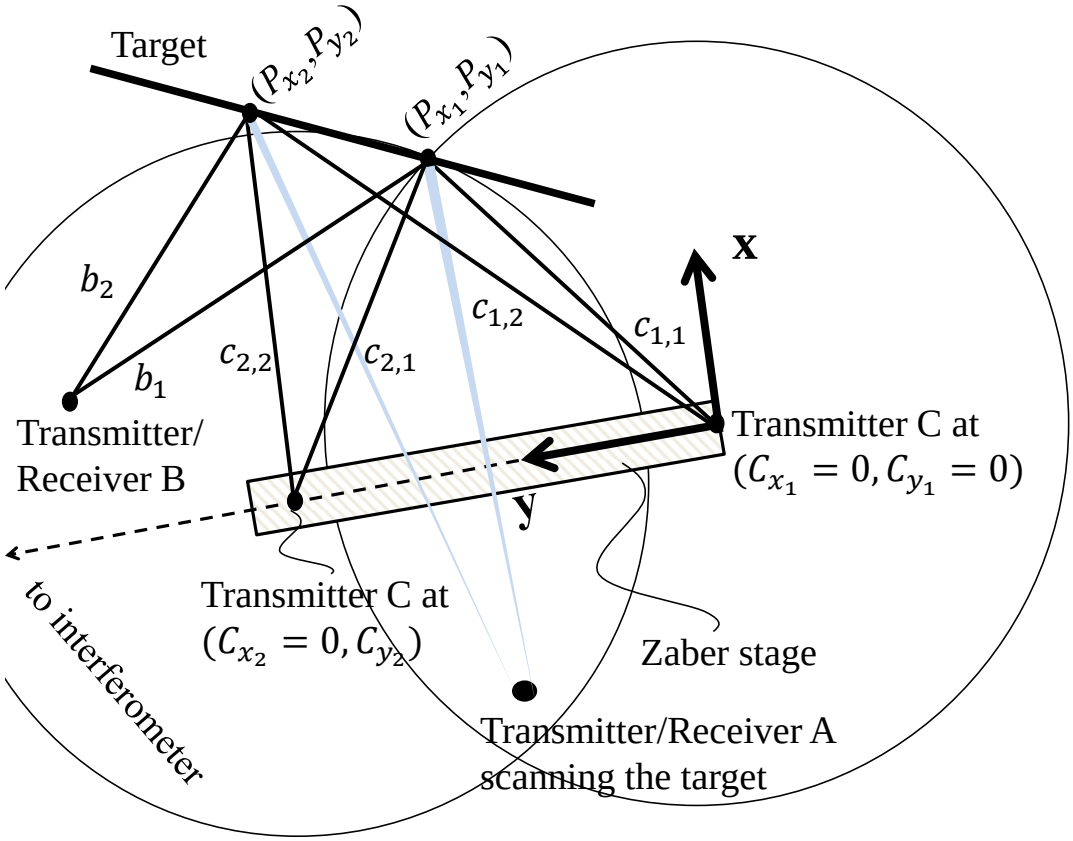

Figure 38. First part of the calibration for the position of the B emitter using the trilateration setup itself.

Secondly, following the same principle, now that we know b_1, b_2, P_{x_1}, P_{y_1}, P_{x_2} and P_{y_2}, the intersection of the circle with origin at (P_{x_1}, P_{y_1}) and radius b_1 with the circle with origin at (P_{x_2} P_{y_2}) and radius b_2 determines the position of the target (B_x, B_y) as it can be observed in Figure 39 by solving:

$$\begin{aligned} \left(P_{x_1} - B_x\right)^2 + \left(P_{y_1} - B_y\right)^2 &= {b_1}^2 \\ \left(P_{x_2} - B_x\right)^2 + \left(P_{y_2} - B_y\right)^2 &= {b_2}^2 \end{aligned} \tag{4.2.9}$$

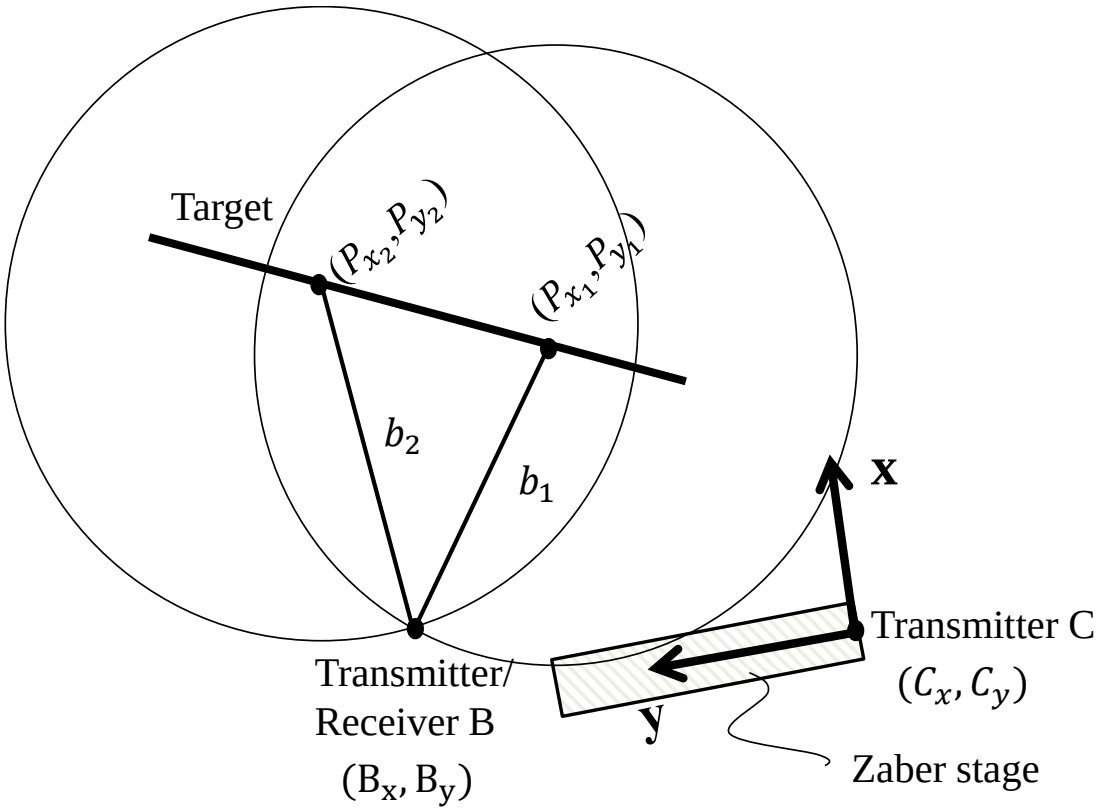

Figure 39. Second part of the calibration for the position of the B emitter using the trilateration setup itself.

Repeating this calibration process many times, i.e. doing it for a lot of different P points on the target surface, would reduce the uncertainty on the resulting B emitter position. Unfortunately, our setup limited the movement range for the C emitter (by the Zaber stage short length (36 cm)) which as a consequence did not let us scan large ranges of positions P. Therefore, the derived results for B_x and B_y were not as accurate as desired and this error was reflected on the target results shown later. Improving the calibration method, i.e. finding the position of the B emitter more accurately, would allow the whole trilateration setup to be self-calibrated, which is one the most important features of a metrology system.

Scanning the Target

Once b, c, B_x, B_y, C_x and C_y are known, the intersection of the circle with origin at (B_x, B_y) and radius b with the circle with origin at (C_x, C_y) and radius c determines the position of the target (P_x, P_y) by solving:

$$\begin{aligned}\left(P_x - B_x\right)^2 + \left(P_y - B_y\right)^2 &= b^2 \\ \left(P_x - C_x\right)^2 + \left(P_y - C_y\right)^2 &= c^2\end{aligned} \tag{4.2.10}$$

Scanning the target with the emitter/receiver A permits taking measurements at several positions (P_x, P_y) giving a full 2D profile of the surface.

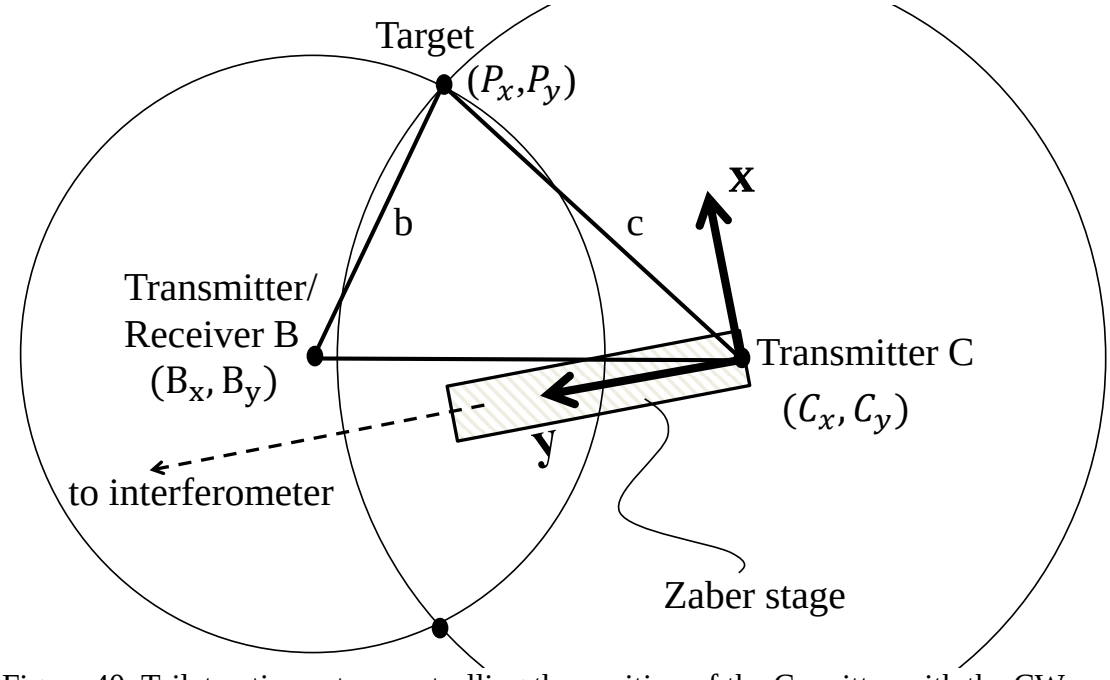

Figure 40. Trilateration setup controlling the position of the C emitter with the CW interferometer.

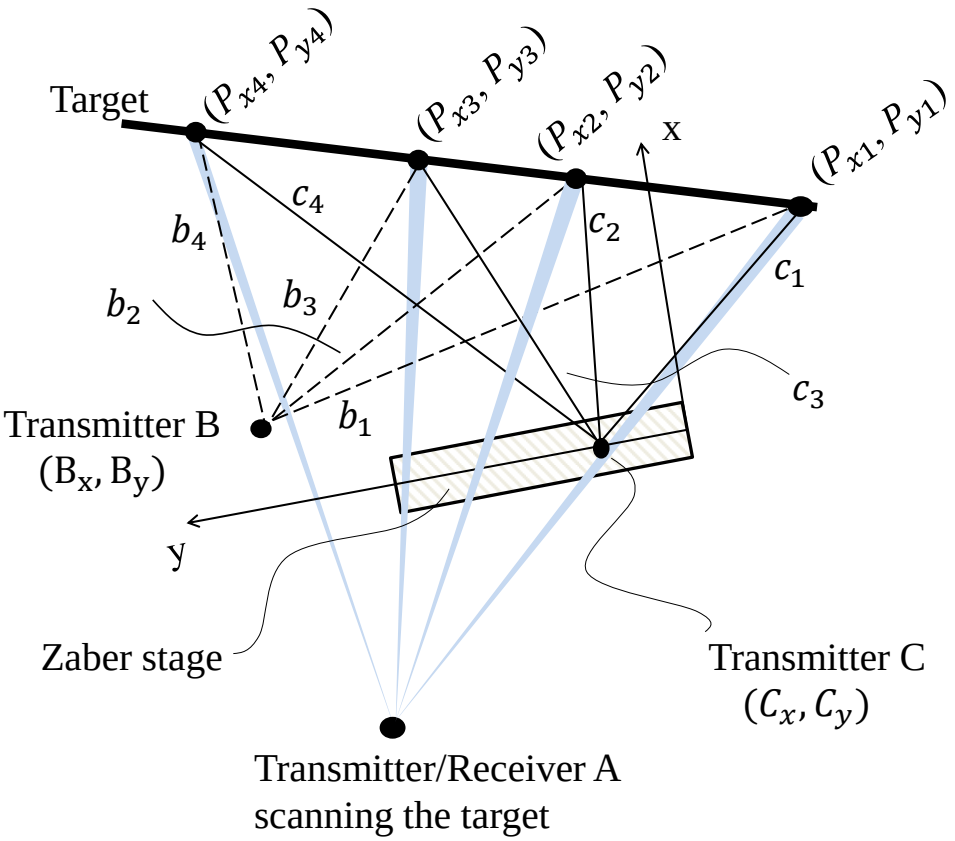

Figure 41.Setup to horizontally scan the target and get a 2D profile of its surface.

Photon Budget Analysis

A step by step analysis of the power/photon budget going through the system (see Figure 42) from the very beginning (laser source) to the very end (detector) follows below. All the pertaining calculations are done using the MATLAB script photonBudget.m (see Appendix).

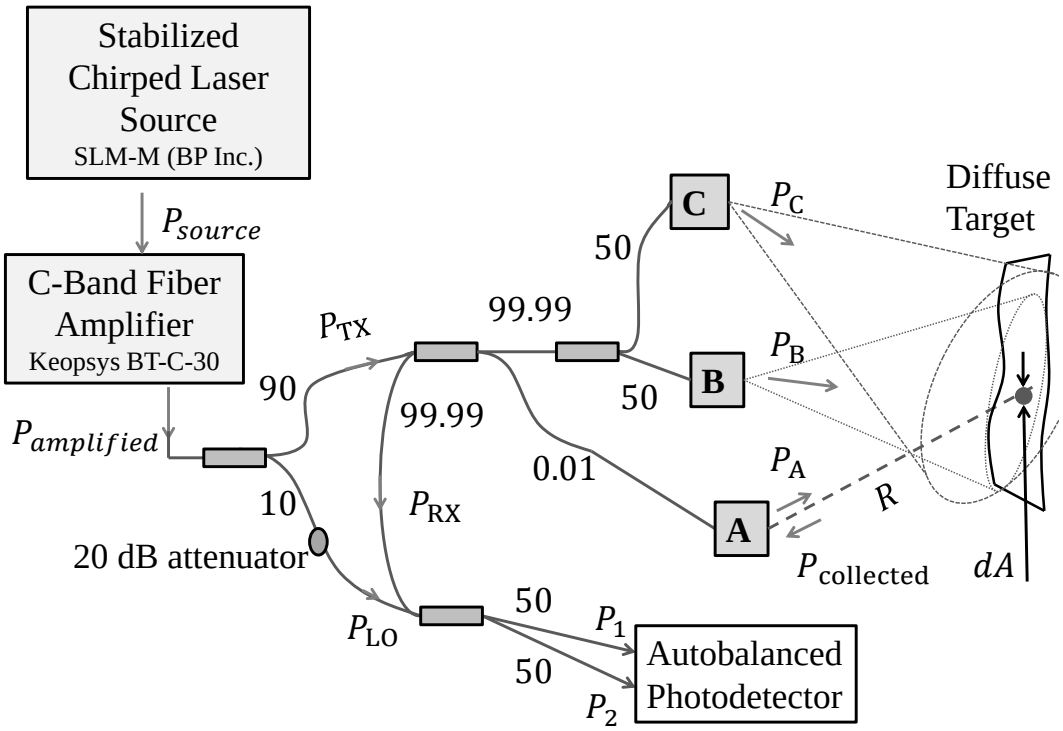

Figure 42. Power scheme of the trilateration setup for photon budget calculations.

From Laser Source to Emitters A,
B and C and to LO Path

For the trilateration setup presented above, an initial power (P_{source}) of 11 mW was used. A Keopsys C-band fiber amplifier was used to bump up this power to 0.8 W. Initial power measurements showed low loss on the output of the amplifier but after several fiber changes a bad connector (61% transmission) was accidentally introduced right after the amplifier in the setup for the measurements presented in this chapter. Considering this bad connector the amplified power, $P_{amplified}$, going into the system was 491 mW. This power was then split several times with different ratios (see Figure 42) till the light arrived following the Tx path at the emitters A, B and C. There is a loss of 0.3 dB in power that has to be taken into account every time the light goes through a

fiber (connector to connector). However, these losses are ignored in the Tx/Rx path as they are not significant when compared with the LO path's ones. A 20 dB attenuator was placed at the LO path to decrease the power reaching the auto-balanced photodetector in order to avoid saturation.

The power transmitted by the emitters results to be:

$$\begin{aligned} P_A &= 44\ \mu W \\ P_B &= P_C = \ 221\,\text{mW} \end{aligned} \tag{4.3.1}$$

As explained before, having a really low portion of the power emitted by A allows focusing that beam tightly on the target's surface without having to worry about eye safety on the surrounding of the experiment. The light emitted by B and C is high power but still safe(after a distance of 40 cm) as the emitters are bare fibers that allow the beam to diverge quickly and make sure the target would be hit by some of it, even if they are not perfectly directed to the target. All of these facts combined make the experiment idea really suitable to long range measurements outside of the lab.

At the end of the LO path the power, considering the fiber connector losses and the 20 dB attenuator, results to be $P_{LO} = 366\ \mu W$ which is several orders of magnitude larger than the power returning from the target into receiver A ($P_{collected}$) as it can be seen below.

Propagation from Emitter A to
Target and Back to Receiver A

As the experiments were all tabletop-scale laboratory demonstrations at 1536 nm, atmospheric absorption and scattering is small and can be ignored and $\eta_{atm} = 1$ is

assumed for the photon budget calculations. For the diffuse targets under consideration a 70% target reflectivity (ρ_T) is assumed for the photon budget calculation.

As explained in section 4.2, a triple collimator is used for transmitter A to provide the minimum divergence and wavefront error with an initial spot size of 1.9 mm. The collimated beam travels through two lenses that allow focusing the light on a small spot of area A_{spot} onto the target surface (for a distance from emitter/receiver A to target of 1.6 m the radius of the spot according to Equation (2.3.1) is 409 μm) . The focal length F of the system could be varied by changing the distance d between the lenses, allowing for focusing on different targets at different distances from the emitter/receivers. The transmission through the optics is assumed to be 100% as the lenses are AR coated. As the full extent of this collimated beam hits the target, it is considered an extended target and we can obtain the power returning back P_{AA} with the use of Equations (2.3.4) and (2.3.5):

$$P_{AA} = 42\ pW\ , \tag{4.3.2}$$

where the receiver area is taken equal to the emitter area of spot size 1.9 mm (power emitted by A and returning back to A). This power is equivalent to $3 \times 10^8 photons/s$, which is also equal to the power in the 2x2 splitter before the auto-balanced detector, since 99.99% of the power collected by emitter A is coupled to the 2x2 splitter. Therefore, the number of photons collected in the coherent integration time T (equal to the length of the chirp τ_c) is $N_{collectedAA} 7 \times 10^5 \sim photons$ for the DFB laser ($\tau_c = 2.3ms$) and is $N_{collectedAA} \sim 2.6 \times 10^6\ photons$ for the BP laser ($\tau_c = 8ms$).

Propagation from Emitters B and C to
Target and Back to Receiver A

The emitters B and C are just bare fibers to allow the beams diverging really fast after leaving the fiber. In this way, only a portion of the whole beams (with areas A_{spotB} and A_{spotC} respectively) hit the target, and even a smaller portion of them hit exactly the A_{spot} area of the beam A's focused spot on the target. Only the last is reflected by the diffuse target and collected back by receiver A. A small amount of the transmitted light is reflected back to B and C and collected but it is neglected because it doesn't contain any information of interest for getting the target's position according to the power setup design. Thus, taking into account the ratio of the spot areas at the target A_{spot}/A_{spotB} and A_{spot}/A_{spotC}, the power captured by A returning from the emitters B (P_{BA}) and C (P_{CA}) is given by using Equations (2.3.4) and (2.3.5) :

$$\begin{aligned} P_{BA} &= 0.72\ pW \\ P_{CA} &= 0.65\ pW\ , \end{aligned} \tag{4.3.3}$$

which is equivalent to $N_{collectedBA}$~$1.28 \times 10^4\ photons$ and $N_{collectedCA}$~$1.16 \times 10^4\ photons$ collected in the coherent integration time for the DFB laser respectively, and $N_{collectedBA}$~$4.46 \times 10^4\ photons$ and $N_{collectedCA}$~$4.02 \times 10^4\ photons$ collected in the coherent integration time for the BP laser respectively.

From Receiver A to Detector

Nearly all the power collected by receiver A from the target (P_{AA}, P_{BA}, P_{CA}) travels through the Rx path (P_{RX}, see Figure 31) and is coherently combined with the power of the LO path (P_{LO}) before reaching the two inputs of the auto balanced detector.

Shot Noise Analysis

Taking into account the Hanning window effect in the CNR explained previously (decreases CNR by a factor of 3 dB), the CNR and SNR results obtained with Equations (2.2.3) and (2.2.5) according to the shot noise in coherent heterodyne detection theory are summarized in Table 6 below.

	T_{read} [ms]	CNR [dB]			SNR [dB]			Precision		
		AA	BA	CA	AA	BA	CA	AA	BA	CA
DFB	2.3	51.2	33.5	33.0	48.2	30.5	30.1	1.1 mm	1.4 mm	1.4 mm
BP	8	56.6	38.9	38.5	53.6	35.9	35.5	45 μm	55 μm	55 μm

Table 6. CNR and SNR results for the BP and DFB laser trilateration system for heterodyne detection at the shot noise limit. The CNR and SNR values are obtained by introducing the theoretical number of photons received ($N_{collectedAA}$, $N_{collectedBA}$, $N_{collectedCA}$) into Equations (2.2.3) and (2.2.5) respectively. Then, the theoretical range resolution obtained in Equation (4.2.4) and the resulting SNR are introduced into Equation (2.2.6) to get the precision.

Now, some examples of the frequency spectrum for the data collected with the DFB laser (Figure 43) and with the BP laser (Figure 44 and Figure 45) are shown below:

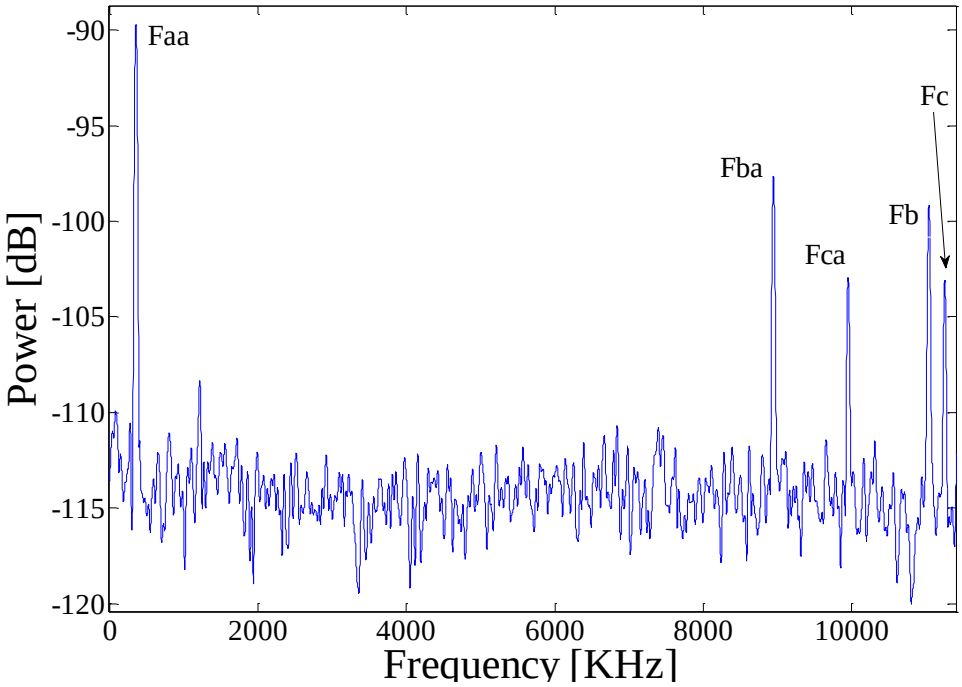

Figure 43. Example of the Power versus Frequency of the signals obtained with the DFB laser (see Table 5 for nomenclature definitions).

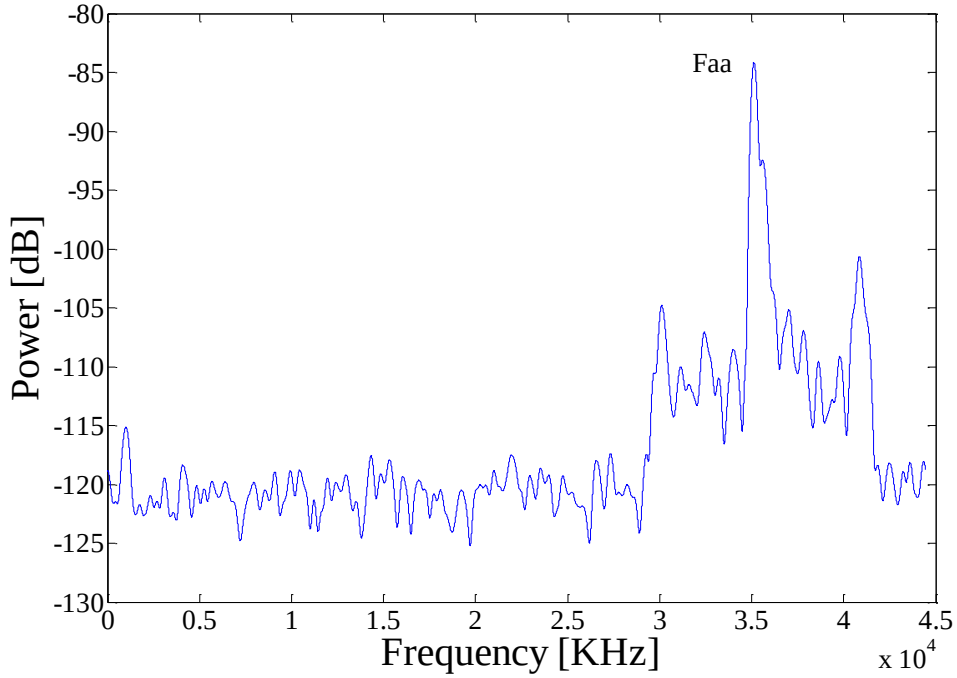

Figure 44. Example of the Power versus Frequency for the F_{aa} signal obtained with the BP laser (see Table 5 for nomenclature definitions).

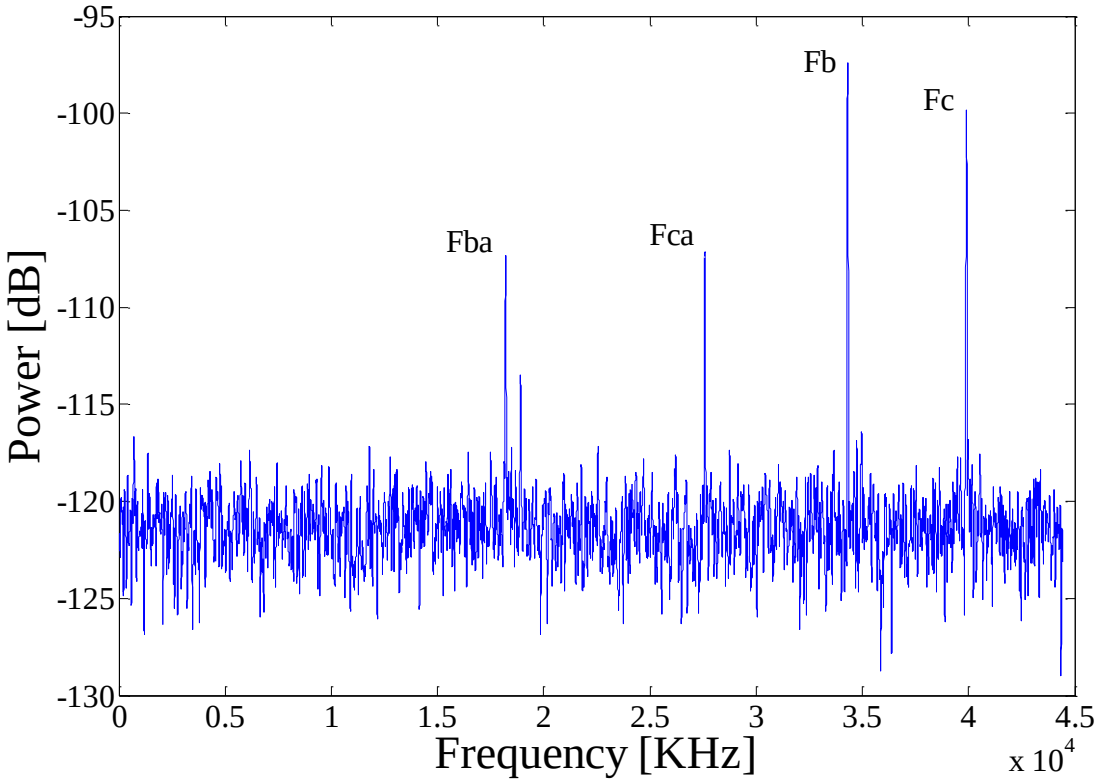

Figure 45. Example of the Power versus Frequency of the signals obtained with the BP laser (see Table 5 for nomenclature definitions).

A table comparing the values for the SNR on Table 6 with the experimental SNR shown by the pictures is shown below.

	AA			BA			CA		
	$N_{collected}$ $\times 10^4$	SNR [dB]		$N_{collected}$ $\times 10^4$	SNR [dB]		$N_{collected}$ $\times 10^4$	SNR [dB]	
		Th	Exp		Th	Exp		Th	Exp
DFB	37	48	~25	0.6	30.5	~18	0.58	30	~15
BP	130	54	~35	2.2	35.9	~15	2	35.5	~15

Table 7. Number of photons collected in the integration time, theoretical and experimental SNR for each of the signal returning back to receiver A.

The power ratios between corresponding peaks vary considerably for both experimental (Exp) and theoretical (Th) values. Moreover, a significant lower resulting

experimental SNR is observed for all the peaks. To check if these differences can be explained by the Rayleigh scattering effect in the fibers, the CNR and SNR are calculated again taking this loss into account.

Rayleigh Scattering at the Fiber Tip

Substituting $\gamma_{ray} = 4.6 \times 10^{-5} m^{-1}$, $NA = 1.2$, $n_{fib} = 1.486$ and the corresponding range resolutions calculated in Equation (4.2.4) into Equation (2.3.6):

$$\eta_{rayDFB} = 1 \times 10^{-10}$$
$$\eta_{rayBP} = 6 \times 10^{-12} \qquad (4.3.4)$$

Then, taking into account the different splitters in the setup (Figure 42) and converting to photons (see photonBudget.m script in Appendix), the new values for CNR and SNR are calculated and shown in the table below.

	AA			BA			CA		
	$N_{collected}$ $\times 10^4$	SNR [dB]		$N_{collected}$ $\times 10^4$	SNR [dB]		$N_{collected}$ $\times 10^4$	SNR [dB]	
		Th	Exp		Th	Exp		Th	Exp
DFB	37	35	~25	0.6	17.5	~18	0.58	17	~15
BP	130	49	~35	2.2	31.2	~15	2.01	30.7	~15

Table 8. Number of photons collected in the integration time, theoretical and experimental SNR for each of the signal returning back to receiver A taking into account Rayleigh scattering effect in the fibers.

A significantly lower resulting experimental SNR is still observed for all the peaks (more pronounced in the case of the BP laser), although comparing values from Table 7 and Table 8 it can be seen that the SNR of the measurements are limited by the Rayleigh scattering effect by a factor of 13 dB for the DFB laser and a factor of 5 dB for the BP laser. An improvement of these values could be obtained by making longer the

fiber going to the transmitter/receiver A in order to move the signals F_{ba} and F_{ca} to frequencies higher than the corresponding to the signals F_b and F_c (see Table 5 for notation). Other possible issues explaining this disagreement could be the target being tilted with respect to the emitters/receivers and the speckle phase effects, that were strongly affecting the signals, especially for D_{ba} and D_{ca}. In any case, the experimental powers used and detected were more than enough power to allow analyzing the information contained in the signal.

Distributed Feedback (DFB) Laser Results

The DFB laser used to take the first measurements is centered at 1536 nm and has an optical bandwidth B of 76.6 GHz that translates in a theoretical resolution of 1.9 mm. However, accounting for the division of data and the Hanning window used for processing the collected data this resolution turns out to be 7.8 mm (see Equation (4.2.4)). Its lower resolution and higher speed collecting the data made it suitable to test to calibrate the system before switching to higher optical bandwidth lasers with higher resolution.

The first target was a non-cooperative aluminum plate painted with matte white spray. The plate was bent several times in a different amount to check the effect of the target surface angle with respect the emitter A's beam direction (Figure 46). The results in Figure 47 indicate that the FMCW LADAR system does a worse job when the target's surface gets far away from 90 degrees relative to the A beam (the dispersion of the points indicating the position of the target is bigger). The explanation for this is that when the

target is totally perpendicular to the emitter A, the spot of the beam A on its surface is nice and small, while when looking from a steep angle is a bigger spot. The accuracy is therefore reduced on the latest case as the area collecting light back to the receiver is bigger than theoretically calculated after focusing the beam as tight as possible. Moreover, Lambertian scattering produces the highest brightness when its surface is normal to source, i.e. the steeper the beam angle when hitting the target, the less power returns to the receiver (see Photon Budget section for further detail).

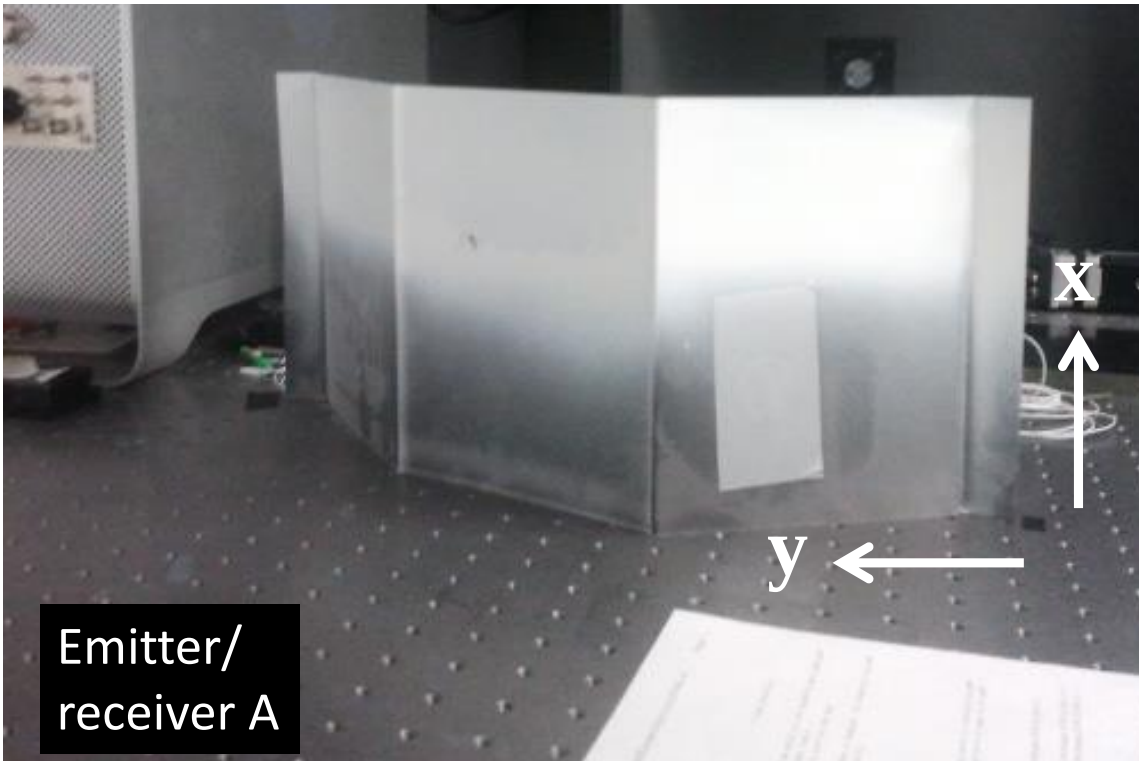

Figure 46. Non-cooperative aluminum plate where its surface is positioned with different angles with respect to the light beam coming from the A emitter

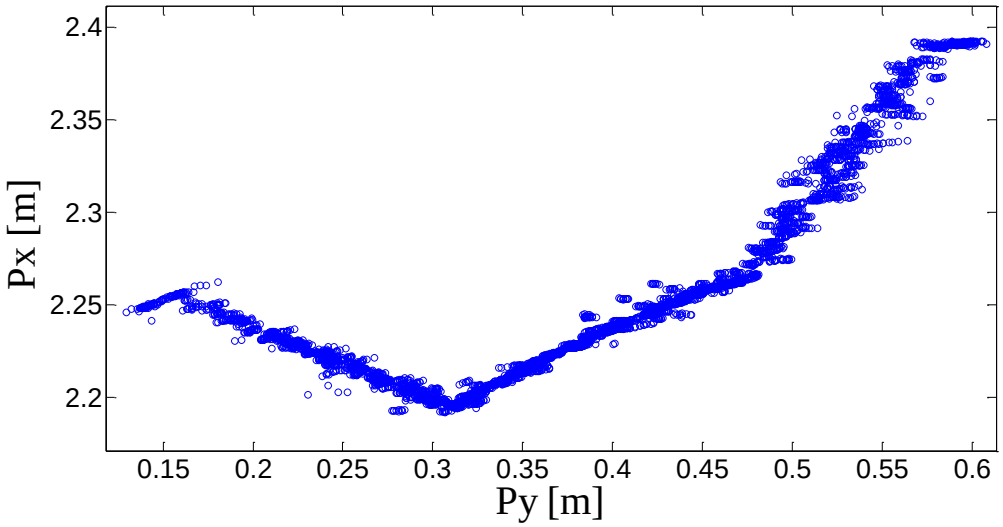

Figure 47. DFB scanning results where a higher dispersion for the target surfaces at a steep angle relative to the incoming beam can be appreciated.

The second target was a flat black anodize aluminum plate. A linear fit of the results reflects a standard deviation of 0.25 mm for the residuals in the x direction (see Figure 48 and Figure 49) and a standard deviation of 2 mm for the residuals in the y direction (see Figure 50 and Figure 51).

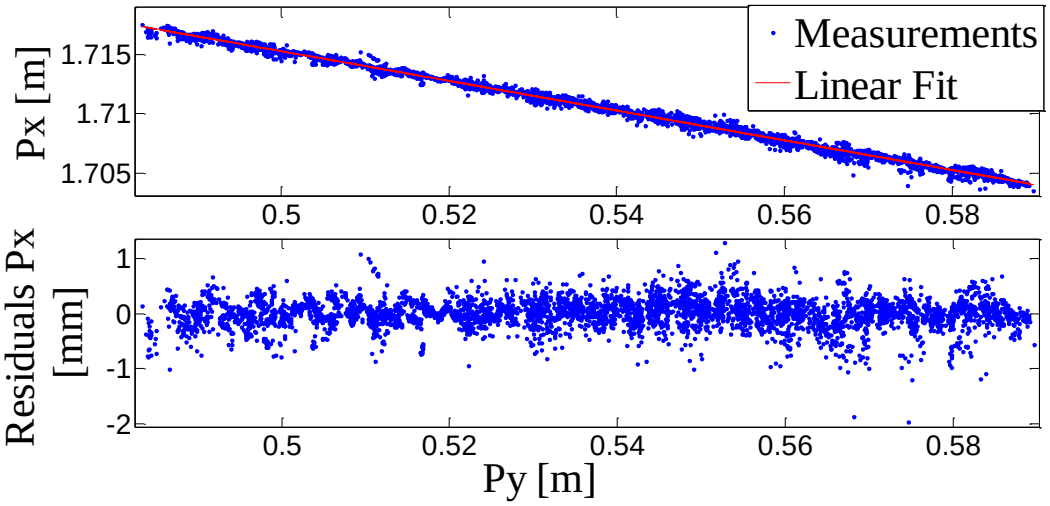

Figure 48. DFB scanning results for a black matte flat target showing residuals in the x direction after linear fit.

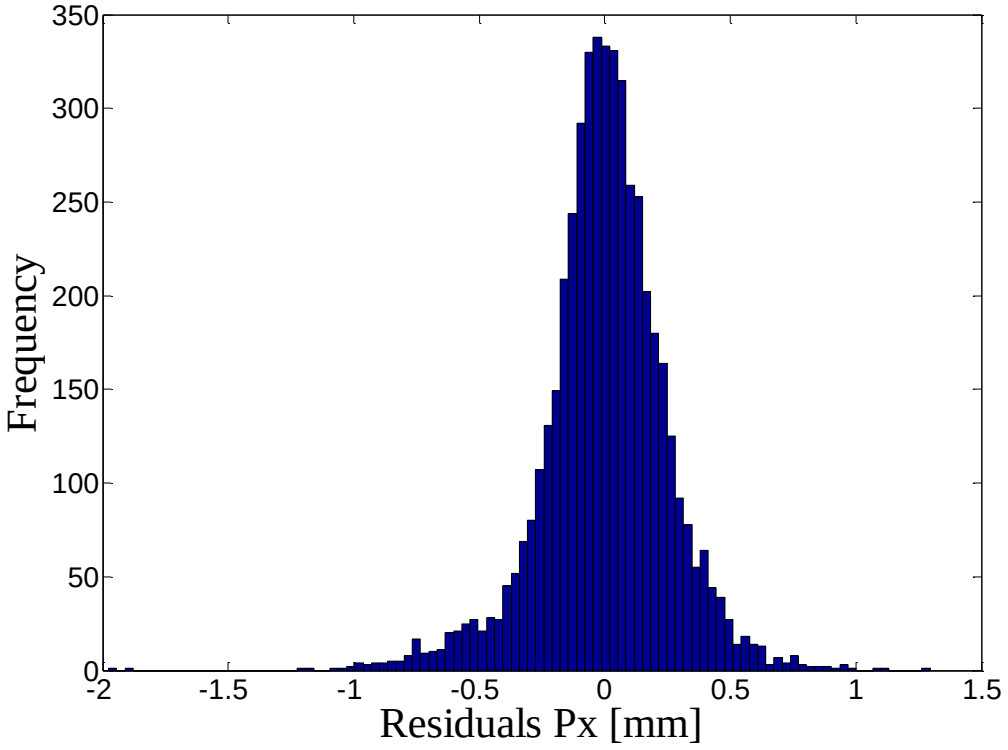

Figure 49. Histogram of the residuals in the x direction after a linear fit of the DFB scanning results.

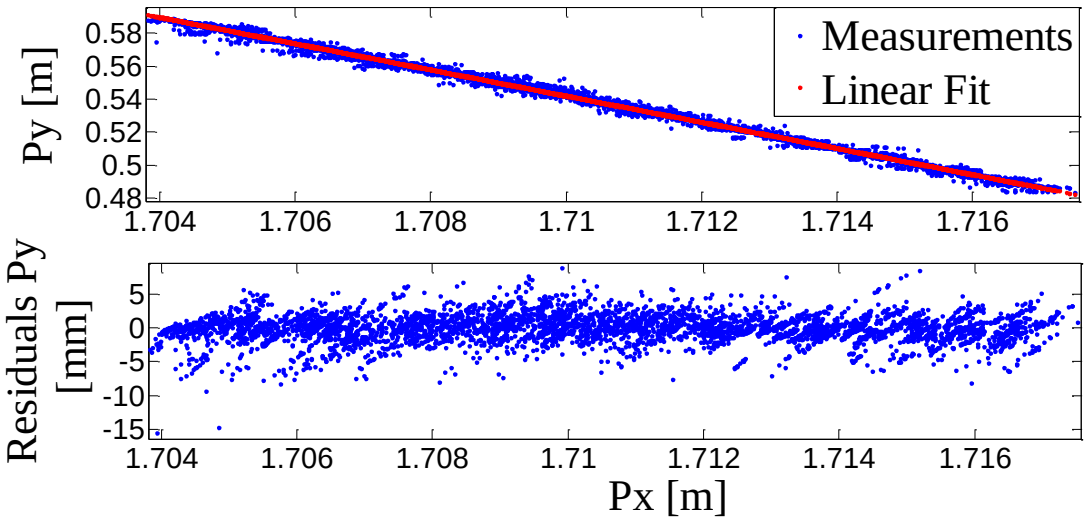

Figure 50. DFB scanning results for a black matte flat target showing residuals in the y direction after linear fit.

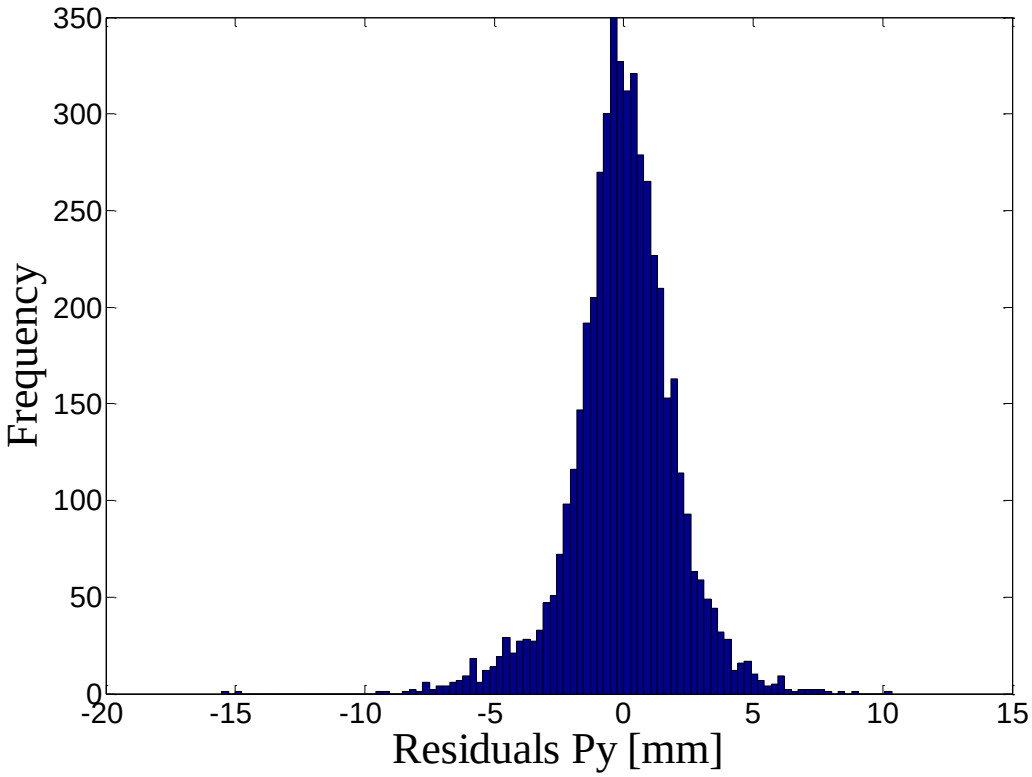

Figure 51. Histogram of the residuals in the y direction after a linear fit of the DFB scanning results.

The residuals in the direction perpendicular to the target (transverse direction in Figure 52) were obtained using basic geometry principles. As the final step of these calculations involved a square root, the sign of the transverse residuals was unknown explaining why the histogram in Figure 53 only shows positive values. The standard deviation of the transverse residuals is found to be 0.21 mm.

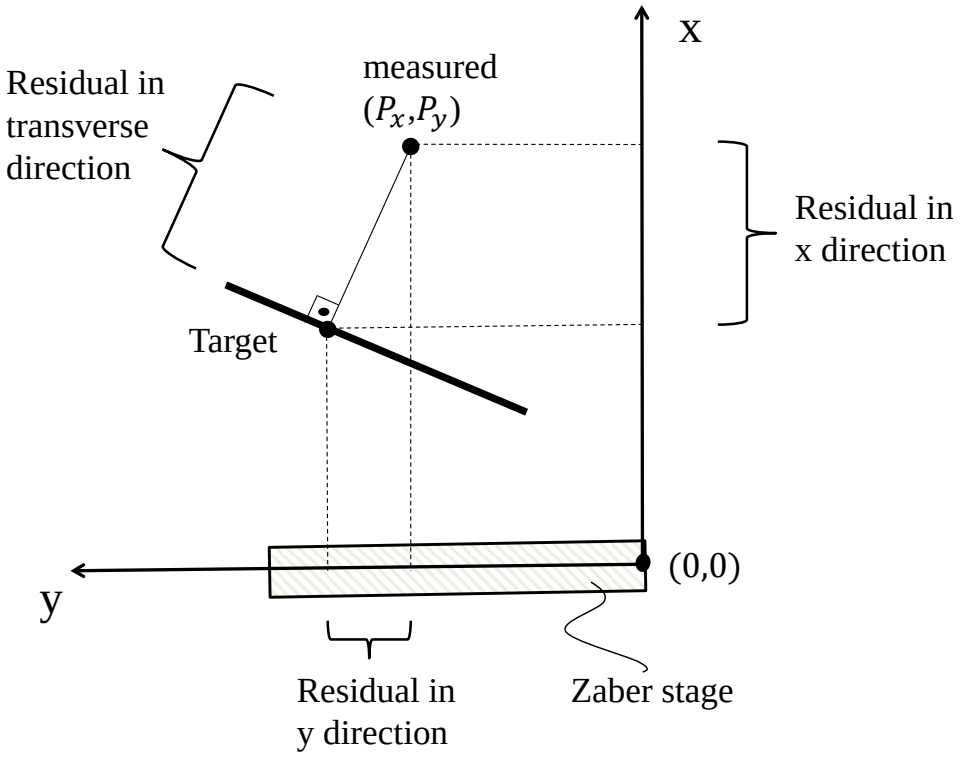

Figure 52. Scheme showing the residuals analyzed after scanning the target.

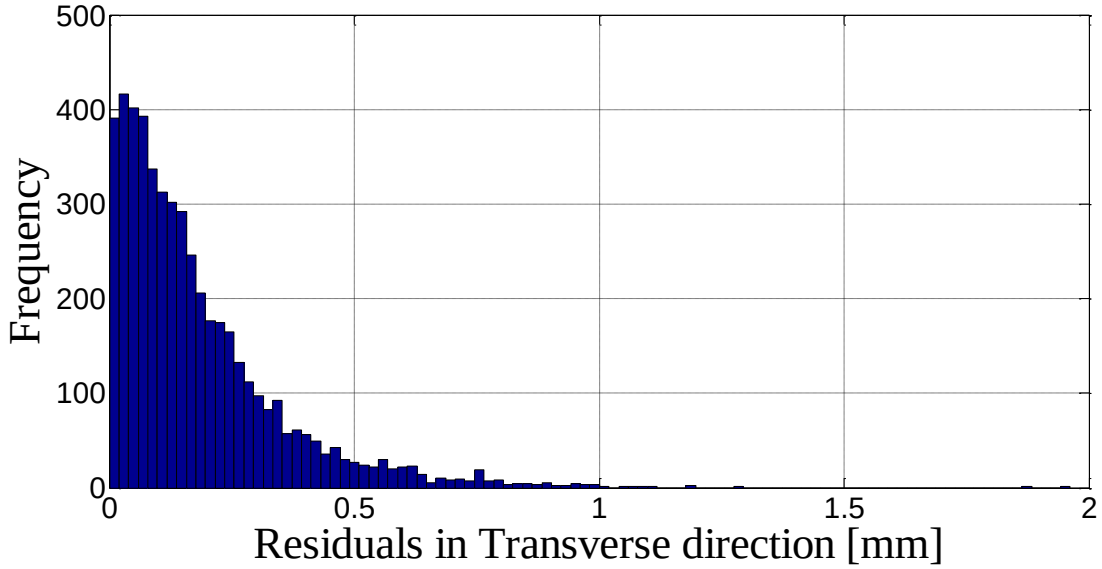

Figure 53. Histogram of the residuals in the transverse direction after a linear fit of the DFB scanning results.

An angled flat surface of 10 degrees was machined in an originally flat piece of aluminum material. The matte white painted resulting target was scanned and the resulting data was smoothed with the Saviztky Golay method to get an approximation of the residuals (Figure 54).

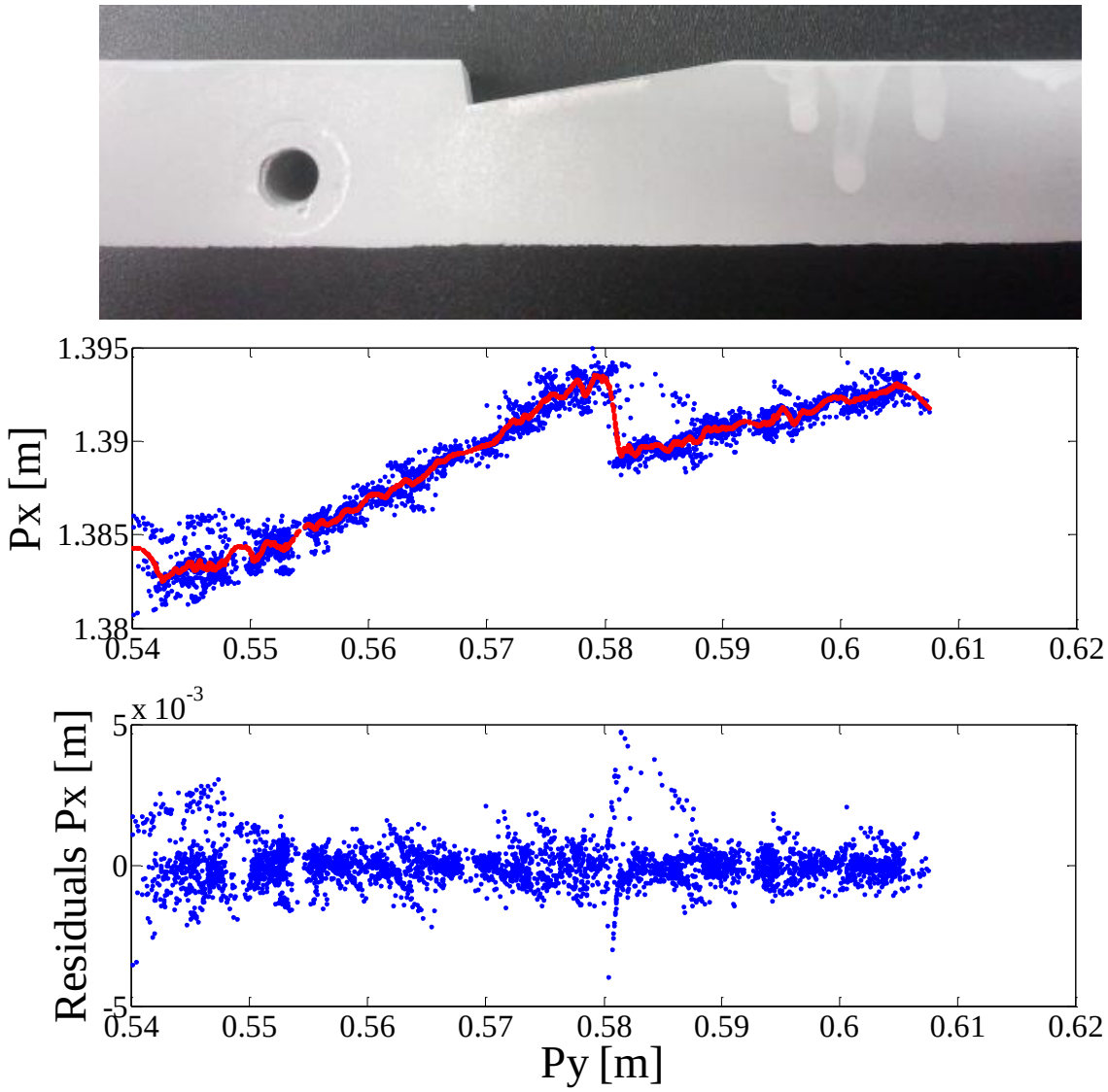

Figure 54. (top) Machined flat surface with a 10 degrees angle on matte white aluminum (bottom) DFB scanning results of the target and Saviztky Golay smooth residuals (standard deviation of 0.66 mm).

The dispersion of the residuals for the flat surface target ($\sim 0.2 - 1.9\ mm$) and for the machined flat surface with a 10 degrees angle ($\sim 0.7\ mm$) are lower than the theoretical range resolution expected with the BP laser's bandwidth of 76.6 GHz (ΔR = 7.8 mm).

Bridger Photonics (BP) Laser Results

A laser from Bridger Photonics Inc. (SLM-M) was borrowed for testing the trilateration system with high resolution. Introducing into Equation (4.2.4) its 1.8 THz optical bandwidth gives a range resolution equal to 329 μm.

The first experiment using this source consisted in looking at a steady point of the target (A beam is fixed) during approximately 5 minutes. In this way, the speckle effect will not affect the uncertainties in the fundamental measurements ($D_{aa}, D_{ba}, D_{ca}, D_b$ and D_c) or in the derived results (c, b, P_x, P_y) as the speckle realization would be the same for every measurement. The standard deviations of the results are summarized in Table 9. The decrease in the value for the uncertainties of the derived distances with respect to the corresponding to the fundamental measurements indicates an existing correlation among $D_{aa}, D_{ba}, D_{ca}, D_b$ and D_c.

Standard deviations [μm]								
Fundamental measurements					Derived results			
D_{aa}	D_{ba}	D_{ca}	D_b	D_c	c	b	P_x	P_y
9.0	10.2	11.5	3.7	4.4	8.5	6.9	7.9	9.5

Table 9. Standard deviations for BP laser trilateration experiment scanning a steady point. The covariance between P_x and P_y was calculated to be equal to $(5\ \mu m)^2$.

When the target is perpendicular to the emitter/receiver all rays contained in the beam travel the same path, while there is more than one emitter and none of them are perpendicular to the target, every path is different (see Figure 55). For example for the distance from emitter B to receiver A (D_{ba}) the rays on the right side of the beam travel a longer path than the rays on the right side of the beam (the difference is marked in red). This can result in different speckle realizations within the spot which would ultimately limit the resolution of the spot to its size 2ω for the worst speckle effect case scenario.

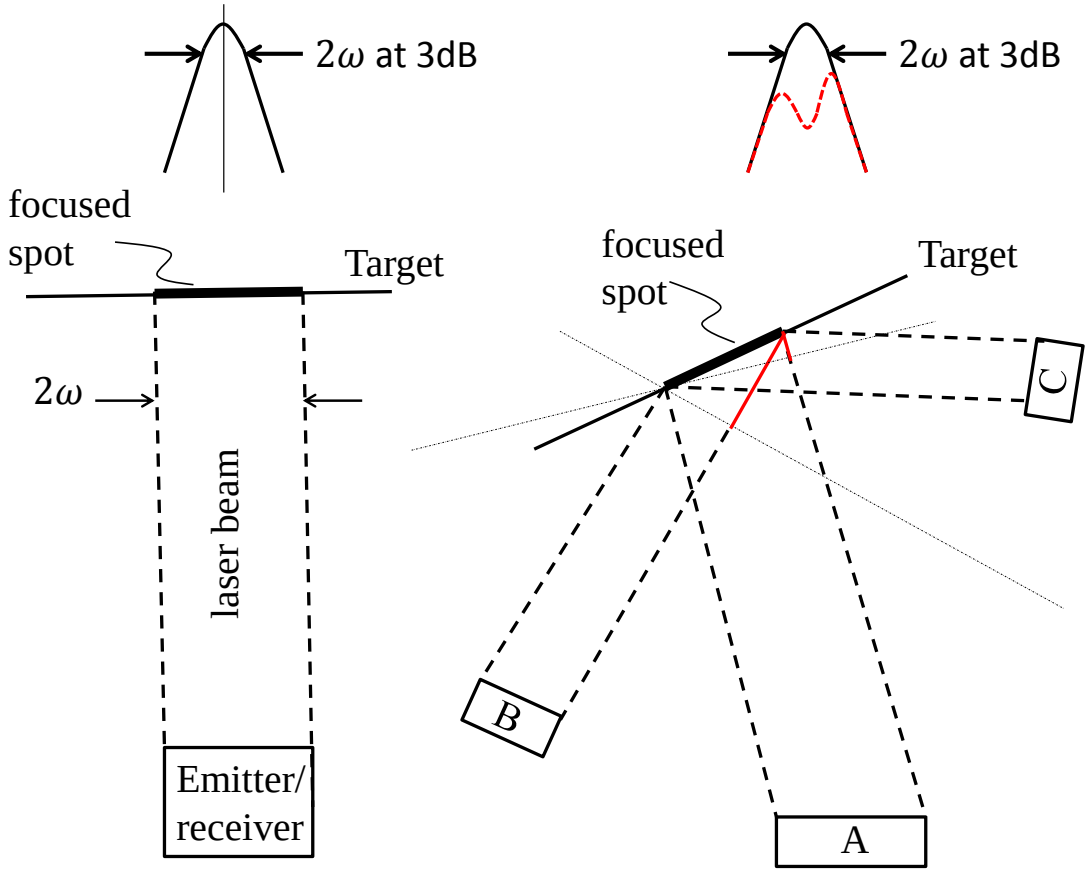

Figure 55. Effect of a non-perpendicular target to the resolution of the measurements in presence of speckle.

Assuming a surface roughness of 5 µm, Equation (2.2.4) was used to calculate the predicted uncertainty in a length measurement perpendicular to the emitter by reference [16] with the range resolution of the BP laser:

$$\sigma = 8.8\ \mu m \tag{4.6.1}$$

Despite of our target not being perpendicular to either of the beams, the standard deviation found for P_x and P_y (7.9 and 9.5 µm respectively) is consistent with this prediction and also well below the size of the spot at the target (2ω = 409 µm).

For the same flat target scanned with the DFB laser source (flat black anodize aluminum plate), the residuals for the resulting data compared to a linear fit are shown below. The dispersion on the residuals in the x direction is 0.1 mm which is 2.6 times less than the theoretical range resolution expected for the BP laser.

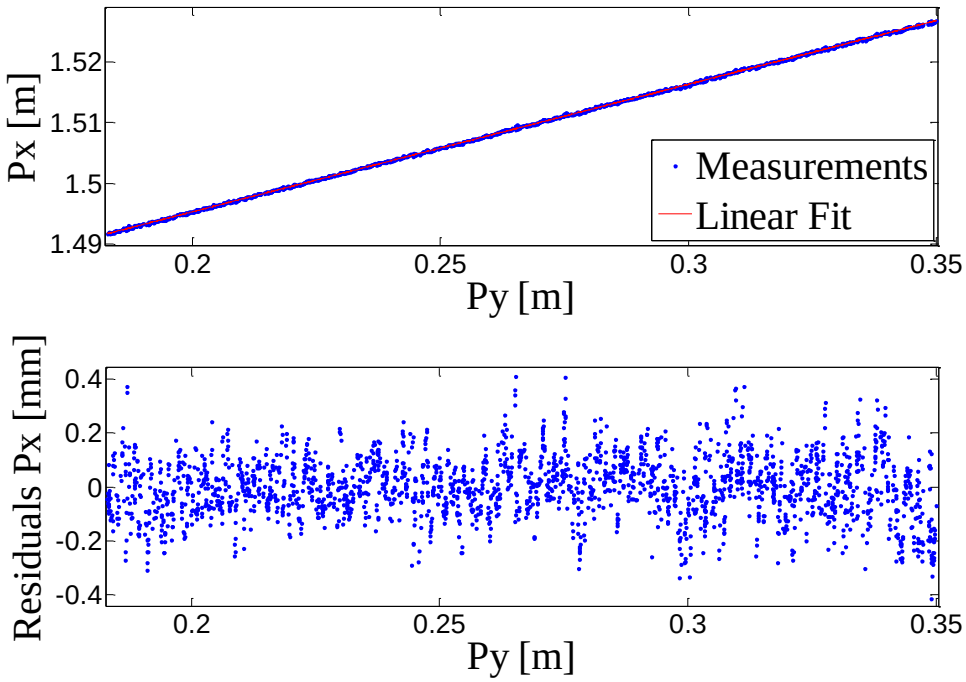

Figure 56. BP scanning results for a black matte flat target showing residuals in the x direction after linear fit.

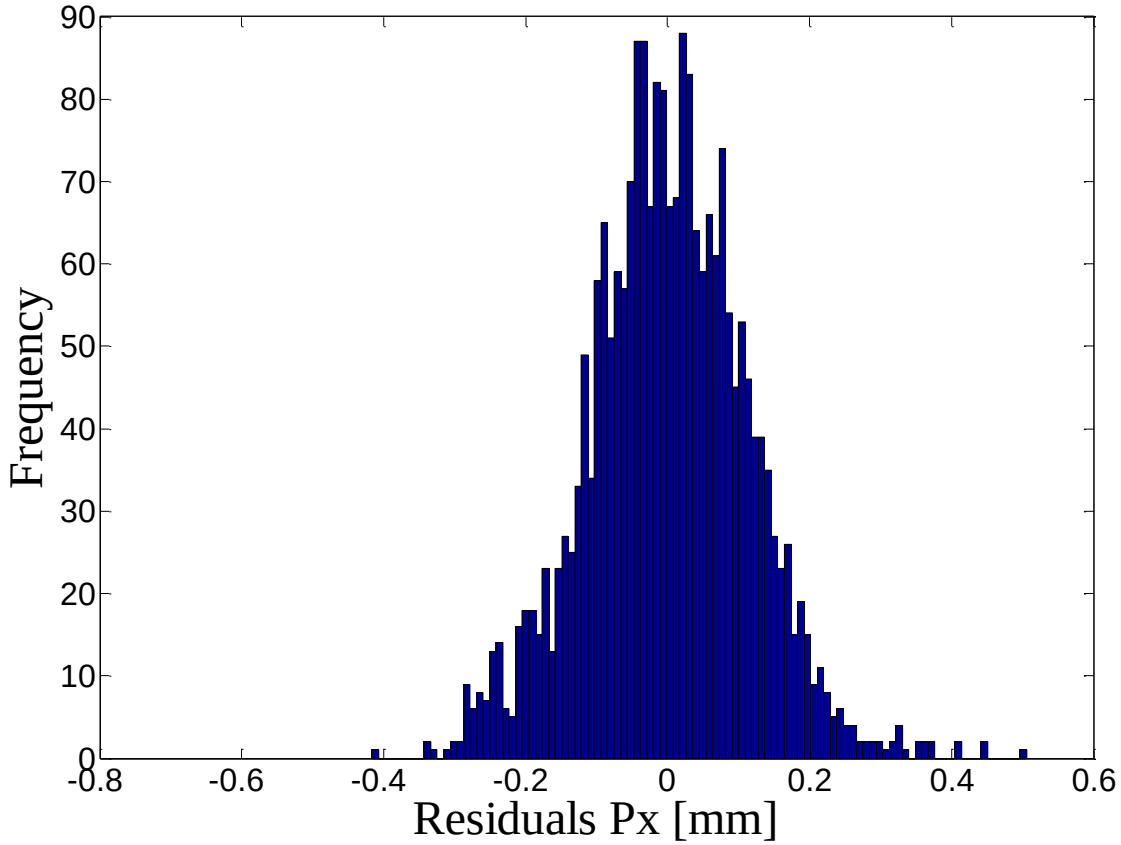

Figure 57. Histogram of the residuals in the x direction after a linear fit of the BP scanning results.

However, the residuals in the y direction are much bigger than expected (standard deviation equal to 0.5 mm, almost twice the resolution) and possible reasons to explain this are analyzed later on this chapter.

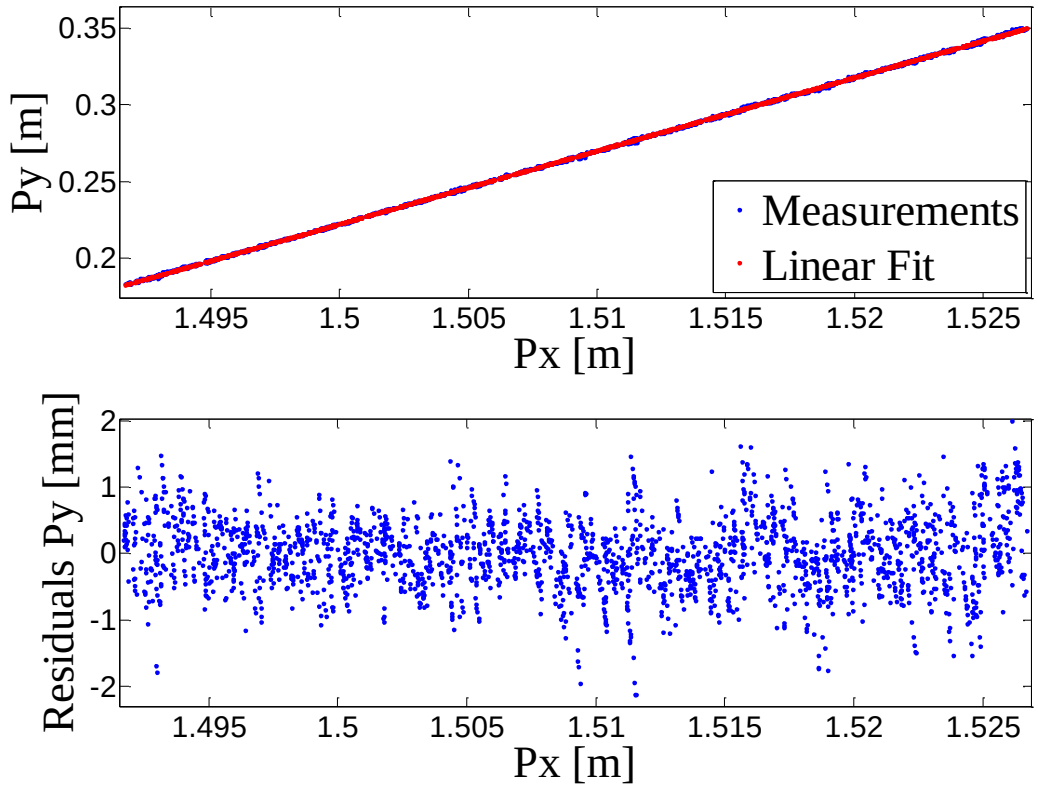

Figure 58. BP scanning results for a black matte flat target showing residuals in the y direction after linear fit.

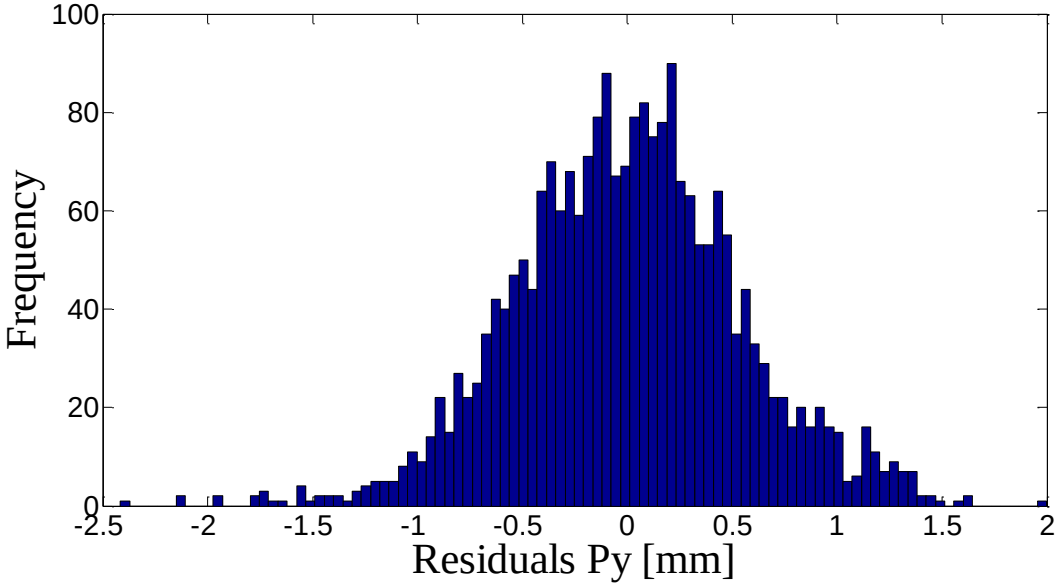

Figure 59. Histogram of the residuals in the y direction after a linear fit of the BP scanning results.

The residuals on the transverse direction are found as explained for the DFB laser and their corresponding standard deviation is 105 μm, which is well below the range resolution but still almost 10 times the result obtained when looking at a steady point of the target. This could be due to a stronger consequence of the issue described in Figure 55 when the emitter A is scanning the target. Averaging data measurements before calculating P_x and P_y shows improvement on the standard deviation of the residuals on the transverse direction. However, this has to be done carefully to avoid averaging measurements corresponding to different spots on the target.

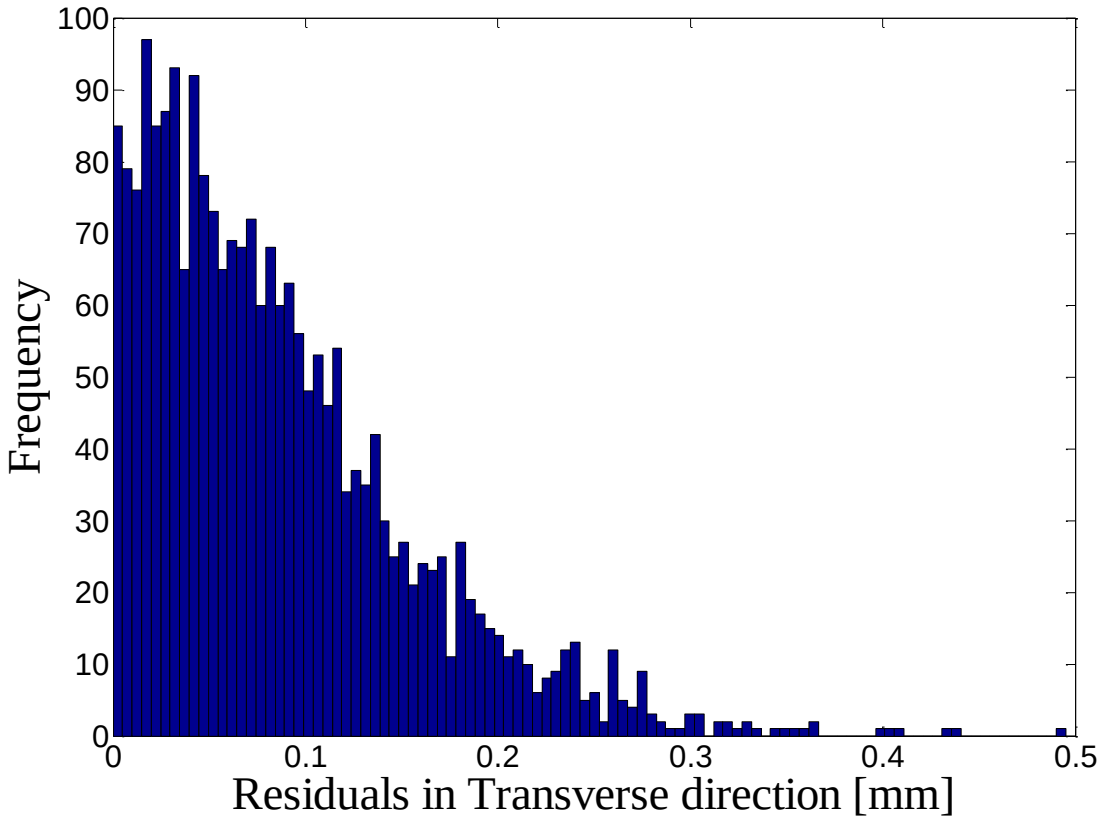

Figure 60. Histogram of the residuals in the transverse direction after a linear fit of the BP scanning results (without averaging).

In the end, a customized machined target with different features of different sizes was scanned with the FMCW LADAR system using the BP laser as a source. The big feature showing an angled flat surface of 10 degrees (see machined feature on the far left of Figure 61) is the same as the one used as a target for the DFB laser above (Figure 54). The Savitzky-Golay method was used again here to get an idea of the residuals depending on the scanned feature of the target.

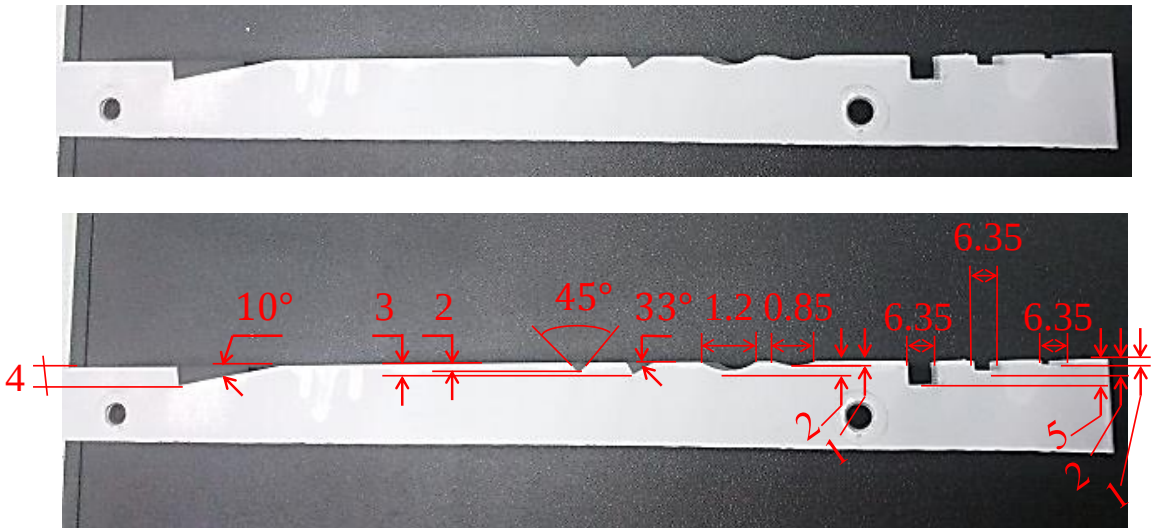

Figure 61. Machined aluminum plate with various features with (middle) its dimensions in mm

The results show that the system is capable to image all kind of features (angled flat surfaces, rectangular incisions, round incisions) of depths ranging from 1 to 5 mm. The residuals show a dispersion of 0.19 mm which is more than 1.5 times lower than the theoretical expected range resolution for the bandwidth of the laser source.

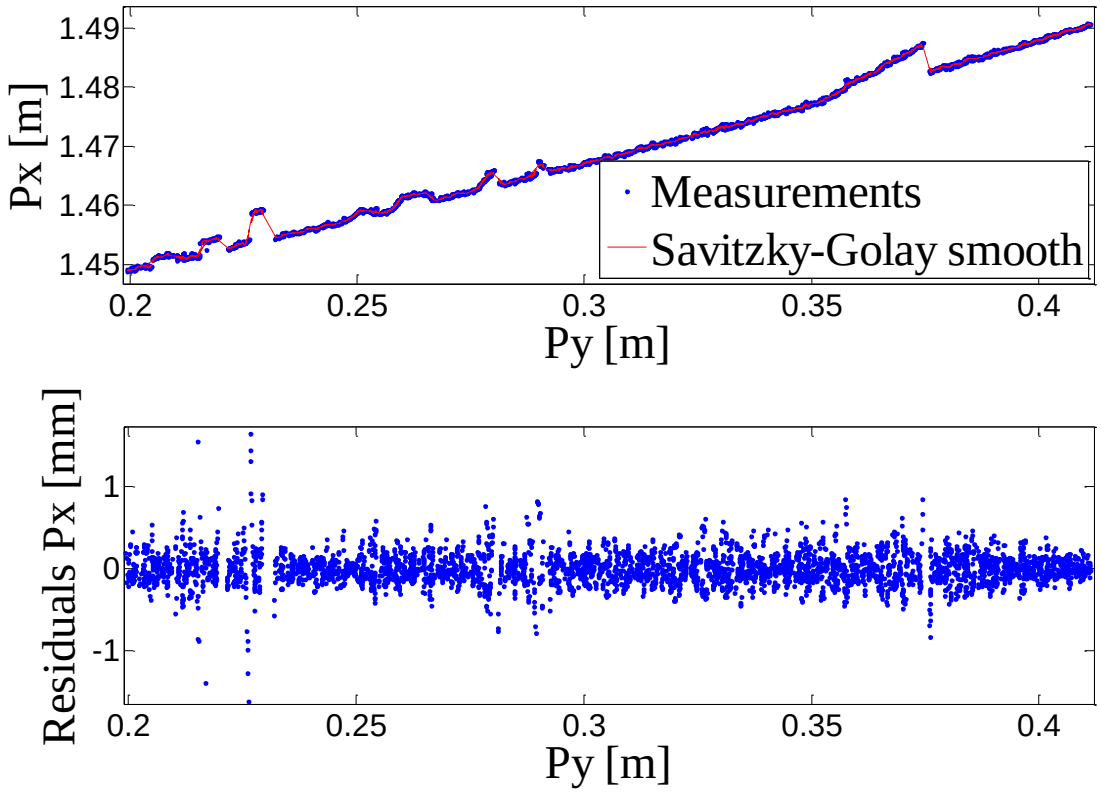

Figure 62. BP scanning results with residuals of linear fittings.

Table 10 compares the dispersion of the residuals found for the flat target and for the machined target using the two different laser sources. Although Equation (2.1.14) clearly states that a large optical bandwidth B is desired to achieve high range resolution in 1D FMCW LADAR, this is not as obvious for the two dimensional case according to the results in the table below. Increasing the optical bandwidth by a factor of 26 translates to barely double resolution in the transverse direction. Speckle is definitely playing an important role in the 2 dimensional imaging system and appears to be the biggest limiting factor encountered for this thesis.

	B	$\Delta R_{data\ division +Hanning}$ [mm]	Dispersion of residuals [mm]			
			Target #1			Target # 2
			x-dir	y-dir	transverse direction	x-dir
DFB	76.6 GHz	7.80	0.25	1.99	0.21	0.66
BP	1.8 THz	0.27	0.11	0.54	0.10	0.19

Table 10. Comparison of the BP and the DFB results for target #1 (black anodize aluminum plate, linear fit to get residuals) and target #2 (angled flat surface of 10 degrees, Saviztky Golay smooth to get residuals).

A statistical analysis of the uncertainties follows to determine how to improve the system setup in order to reduce the dispersion even more on the experimental results.

Uncertainty Analysis

The goal of the experiments presented above was to find the target position (P_x, P_y) as a function of several measured variables: the distance from emitter B to target (b), the distance from emitter C to target (c), the position of emitter C (C_x, C_y) and the position of emitter B (B_x, B_y). To achieve this result and evaluate its uncertainty a MATLAB script was created (see errorPropPxPy.m in the Appendices).

$$CovMatrix = \begin{pmatrix} \sigma_{bb}^2 & \sigma_{bc}^2 & \sigma_{bC_y}^2 & \sigma_{bC_x}^2 & \sigma_{bB_y}^2 & \sigma_{bB_x}^2 \\ \sigma_{cb}^2 & \sigma_{cc}^2 & \sigma_{cC_y}^2 & \sigma_{cC_x}^2 & \sigma_{cB_y}^2 & \sigma_{cB_x}^2 \\ \sigma_{C_yb}^2 & \sigma_{C_yc}^2 & \sigma_{C_yC_y}^2 & \sigma_{C_yC_x}^2 & \sigma_{C_yB_y}^2 & \sigma_{C_yB_x}^2 \\ \sigma_{C_xb}^2 & \sigma_{C_xc}^2 & \sigma_{C_xC_y}^2 & \sigma_{C_xC_x}^2 & \sigma_{C_xB_y}^2 & \sigma_{C_xB_x}^2 \\ \sigma_{B_yb}^2 & \sigma_{B_yc}^2 & \sigma_{B_yC_y}^2 & \sigma_{B_yC_x}^2 & \sigma_{B_yB_y}^2 & \sigma_{B_yB_x}^2 \\ \sigma_{B_xb}^2 & \sigma_{B_xc}^2 & \sigma_{B_xC_y}^2 & \sigma_{B_xC_x}^2 & \sigma_{B_xB_y}^2 & \sigma_{B_xB_x}^2 \end{pmatrix} \quad (4.6.2)$$

Some of the CovMatrix elements could be directly extrapolated from collected data ($\sigma_b^2, \sigma_c^2, \sigma_{C_y}^2, \sigma_{bc}^2, \sigma_{bC_y}^2, \sigma_{cC_y}^2$). Setting the rest of the elements to zero the resulting expected error is:

$$\begin{aligned} \sigma_{P_x} &= 14\mu m \\ \sigma_{P_y} &= 3\mu m \end{aligned} \tag{4.6.3}$$

These results are consistent with the experimental values obtained looking at a steady point of the target (see Table 9 values). This confirms that fundamentally the system is capable of making 10 μm measurements but the speckle noise increases the scatter when scanning the target.

To get a more realistic approximation of $\sigma_{P_x}^2$ and $\sigma_{P_y}^2$ the following assumptions were made to obtain the values of the CovMatrix that could not be extrapolated from actual data:

- To find the position of the B emitter the calibration method is basically the same problem as finding the position of target P, but proceeding backwards. Therefore, $\sigma_{B_yB_x}^2$ can be found making the following ratios approximately equal:

$$\frac{\sigma_{P_xP_y}^2}{{\sigma_{P_x}}^2 + {\sigma_{P_y}}^2} \approx \frac{\sigma_{B_yB_x}^2}{{\sigma_{B_x}}^2 + {\sigma_{B_y}}^2}, \tag{4.6.4}$$

  where the standard deviation σ_{B_x} can be assumed to be approximately equal to σ_{P_x} following the same reasoning or can be retrieved from the data obtained on the calibration process.

- According to the manual for the Zaber stage (model THK KR33), the running of parallelism accuracy is 10 μm. Consequently, the $\sigma_{C_x}^2$ was taken to be that uncertainty squared.
- The changes in C_x and C_y are fairly independent in the experiment setup for this thesis due to the definition of the origin of coordinates for both parameters being zero. Hence, $\sigma_{C_yC_x}^2 \approx 0$.
- The movement of the C emitter is independent from the movement of the B emitter, therefore: $\sigma_{C_yB_y}^2 \approx 0$, $\sigma_{C_yB_x}^2 \approx 0$, $\sigma_{C_xB_y}^2 \approx 0$, $\sigma_{C_xB_x}^2 \approx 0$.
- Also, the movement of the B emitter does not affect the distance c: $\sigma_{cB_y}^2 \approx 0$, $\sigma_{cB_x}^2 \approx 0$. In the same way, the movement of the C emitter does not affect the distance b: $\sigma_{bC_x}^2 \approx 0$.
- The covariance between the distance b and the y-coordinate of the B emitter's position is assumed to be approximately equal to the covariance between the c distance and the y-coordinate of the C emitter's position: $\sigma_{bB_y}^2 \approx \sigma_{cC_y}^2$
- The covariance between the C emitter x-coordinate C_x and the distance c can be expanded using the Equations (2.6.1) and found to be approximately equal to: $\sigma_{cC_x}^2 \approx \cos\theta\sigma_{C_x}^2$, where θ is the angle between the x axis and the straight line between the P point at the target and the C emitter. For $\theta = 90$, $\sigma_{cC_x}^2 \approx \sigma_{C_x}^2$.

- The covariance between the distance b and the x-coordinate of the B emitter's position is assumed to be approximately equal to the covariance between the c distance and the x-coordinate of the C emitter's position: $\sigma^2_{bB_x} \approx \sigma^2_{cC_x}$

Using the data retrieved from calibration measurements for the position of the B emitter, $\sigma^2_{B_y} = (16.9\times10^{-4})^2, \sigma^2_{B_x} = (9.14\times10^{-4})^2$, and taking into account all the assumptions above the MATLAB function gave the following output:

$$\begin{aligned} \sigma_{P_x} &= 3.9\, mm \\ \sigma_{P_y} &= 1.6\, mm \end{aligned} \tag{4.6.5}$$

Obviously, the result is highly biased by the bad results from the calibration of B position. Instead of using those values, the following can be assumed as explained above: $\sigma_{B_y} \approx \sigma_{P_y}$ and $\sigma_{B_x} \approx \sigma_{P_x}$. The statistical uncertainty for the target point P position found using the error propagation equation with these values is:

$$\begin{aligned} \sigma_{P_x} &= 43\, \mu m \\ \sigma_{P_y} &= 20\, \mu m \end{aligned} \tag{4.6.6}$$

The results obtained are summarized in the following table:

	σ_{P_x} [μm]	σ_{P_y} [μm]
Setting the unknown CovMatrix terms to zero	14.2	2.9
Making assumptions for the unknown CovMatrix terms and taking $\sigma^2_{B_x}$ and $\sigma^2_{B_y}$ from the experimental calibration	3900	1600
Making assumptions for the unknown CovMatrix terms and taking $\sigma_{B_y} \simeq \sigma_{P_y}$ and $\sigma_{B_x} \simeq \sigma_{P_x}$	43.9	20.1

Table 11. Summary of the propagation error equation results for three different cases.

Comparison of the results indicates that a better calibration of the B emitter position with respect the origin of coordinates would lead to a self-calibrated ranging system with results' uncertainties of the target position below $\sim 50 \mu m$.

Discussion

We have studied in this chapter a two dimensional metrology system for passive non-cooperative targets based on trilateration principles and using a FMCW laser as the source. Two of them were used: the DFB laser with B=76.6 GHz and the BP laser with B=1.8 THz. The photon budget analysis of the setup gave the number of photons collected returning back from the target and getting to the detector in the integration coherent time for a particular laser. Study of the shot noise in heterodyne detection provided the CNR and SNR of the system. All these results with the SNR experimental values are summarized in Table 7 and Table 8 showing that the experimental values were limited by Rayleigh scattering from the tip of the fibers.

The self-calibrated trilateration setup presented above allowed two dimensional metrology measurements of several targets with diverse features giving results with precision way lower to the theoretical range resolutions of the laser sources in use: $\sim 0.2 - 0.6\, mm$ for the DFB laser and $\sim 0.1 - 0.2\, mm$ for the BP laser. The poor calibration obtained for the B emitter was found to increase the distortion of the shape for the final results for the target's profiles. Assuming the B emitter position is be found accurately, the estimation of the uncertainties in the measurements lead to theoretical

errors in the final results using the BP laser of $44\ \mu m$ and $21\ \mu m$ for P_x and P_y respectively, which is an order of magnitude better than the experimental results.

The precision of the results obtained with the DFB laser is on the order of what leading companies in the market of imaging laser scanners offer (~2-3 mm). Therefore, the results obtained with the BP laser are a great improvement on the current surface metrology scenario and, even more, we theoretically demonstrated through the error analysis study that these can be enhanced even more with a better calibration process and a better understanding of the speckle effect.

CONCLUSIONS

Successes and Shortcomings

The CW interferometer was effectively built using a novel fringe counting technique for resolution higher than $\lambda/8$. The high resolution 5 THz FMCW LADAR showed the capability of achieving measurement precision comparable to a CW interferometer without the requirement of continuous unobstructed measurement. Its chirp rate system was calibrated using molecular absorption in ^{12}CO to the 10 ppm level. Moreover, comparison of synchronized measurements of the FMCW LADAR system with the CW interferometer agreed to the 10 ppm level in air. The significant increase in error between the HCN and CO measurements indicates a calibration issue that could be related with the fitting polynomial.

A self-calibrated two dimensional ranging system based on trilateration using a FMCW laser as a source was developed from design stage to experimental implementation providing an excellent learning experience. Several diffuse targets with different machined features were successfully scanned giving out two dimensional profiles of the surfaces. Although the precision of the results was good enough to distinguish every feature, the overall shape was compromised by the calibration of the relative position between the emitters. In any case the results obtained with the BP laser are a great improvement on current non-contact commercial surface metrology and, even more, we theoretically demonstrated through the error analysis that these can be

enhanced even more with a better calibration process and a better mitigation of the speckle effect.

Future Work

The very next step would be to investigate the trilateration-FMCW LADAR system combination's potential for accurate 3D metrology. An extra transmitter would have to be included in the setup as well as another galvo-mirror to scan beam A across the target on the vertical direction.

In general, the success of the work in this thesis was limited to the realm of demonstration and study of the FMCW LADAR on an optical bench. Therefore, the obvious next step would be to take everything done outside of the lab in order to perform longer range (up to 100 meters) 1D and 3D long range measurements. Moreover, mixing trilateration-FMCW LADAR with Synthetic Aperture LADAR (SAL) could bring exponential benefits as SAL is capable of resolving the speckles.

REFERENCES CITED

[1] J. R. Alexandre Cabral, “Accuracy of frequency-sweeping interferometry for absolute distance metrology,” *Opt Eng*, vol. 46, p. 073602, 2007.

[2] P. A. Roos, R. R. Reibel, T. Berg, B. Kaylor, Z. W. Barber, and W. R. Babbitt, “Ultrabroadband optical chirp linearization for precision metrology applications,” *Opt. Lett.*, vol. 34, no. 23, pp. 3692–3694, Dec. 2009.

[3] Z. Barber, “GOALI: Accurate, High Resolution Ladar for 3D Metrology at a Large Standoff Distances Project Description.” .

[4] “Non-contact measurements for today and tomorrow. Nikon metrology formerly Metris. [Online].” .

[5] P. C. D. Hobbs, “Shot noise limited optical measurements at baseband with noisy lasers,” 1991, pp. 216–221.

[6] “A Survey of Methods Using Balanced Photodetection.” Newport.

[7] G. N. Pearson, K. D. Ridley, and D. V. Willetts, “Chirp-pulse-compression three-dimensional lidar imager with fiber optics,” *Appl. Opt.*, vol. 44, no. 2, pp. 257–265, Jan. 2005.

[8] J. R. Taylor, *An introduction to error analysis: the study of uncertainties in physical measurements*, 2nd ed. Sausalito, Calif: University Science Books, 1997.

[9] Z. W. Barber, J. R. Dahl, T. L. Sharpe, and B. I. Erkmen, “Shot noise statistics and information theory of sensitivity limits in frequency-modulated continuous-wave ladar,” *J. Opt. Soc. Am. A*, vol. 30, no. 7, p. 1335, Jul. 2013.

[10] C. Van Loan and Society for Industrial and Applied Mathematics, *Computational frameworks for the fast fourier transform*. Philadelphia: SIAM, 1992.

[11] K. Iiyama, L.-T. Wang, and K. Hayashi, “Linearizing optical frequency-sweep of a laser diode for FMCW reflectometry,” *J. Light. Technol.*, vol. 14, no. 2, pp. 173–178, Feb. 1996.

[12] C. Greiner, B. Boggs, T. Wang, and T. W. Mossberg, “Laser frequency stabilization by means of optical self-heterodyne beat-frequency control,” *Opt. Lett.*, vol. 23, no. 16, pp. 1280–1282, Aug. 1998.

[13] G. Gorju, A. Jucha, A. Jain, V. Crozatier, I. Lorgeré, J.-L. Le Gouët, F. Bretenaker, and M. Colice, "Active stabilization of a rapidly chirped laser by an optoelectronic digital servo-loop control," *Opt. Lett.*, vol. 32, no. 5, pp. 484–486, Mar. 2007.

[14] N. Satyan, A. Vasilyev, G. Rakuljic, V. Leyva, and A. Yariv, "Precise control of broadband frequency chirps using optoelectronic feedback," *Opt. Express*, vol. 17, no. 18, pp. 15991–15999, Aug. 2009.

[15] "National Institute of Standards and Technology." .

[16] E. Baumann, J.-D. Deschênes, F. R. Giorgetta, W. C. Swann, I. Coddington, and N. R. Newbury, "Speckle phase noise in coherent laser ranging: fundamental precision limitations," *Opt. Lett.*, vol. 39, no. 16, pp. 4776–4779, Aug. 2014.

[17] S. M. Maughan, "Distributed fibre sensing using microwave heterodyne detection of spontaneous Brillouin backscatter," University of Southampton, Faculty of Engineering and Applied Science, Optoelectronic Research Centre, 2002.

[18] B. H. Bunch, *The history of science and technology: a browser's guide to the great discoveries, inventions, and the people who made them, from the dawn of time to today*. Boston: Houghton Mifflin, 2004.

[19] A. Sona, "Lasers in Metrology: Distance Measurements," in *Laser Handbook*, vol. 2, North-Holland, 1972.

[20] H. J. Tiziani, "Optical methods for precision measurements," *Opt. Quantum Electron.*, vol. 21, no. 4, pp. 253–282, Jul. 1989.

[21] F. Barone, E. Calloni, R. D. Rosa, L. D. Fiore, F. Fusco, L. Milano, and G. Russo, "Fringe-counting technique used to lock a suspended interferometer," *Appl. Opt.*, vol. 33, no. 7, p. 1194, Mar. 1994.

[22] P. R. Bevington, *Data reduction and error analysis for the physical sciences*, 3rd ed. Boston: McGraw-Hill, 2003.

[23] *Matlab*. Mathworks.

[24] W. C. S. Sarah L. Gilbert, "Hydrogen Cyanide H13C14N Absorption Reference for 1530 nm to 1565 nm Wavelength Calibration - SRM 2519a."

[25] Z. Barber, J. R. Dahl, P. A. Roos, R. R. Reibel, N. Greenfield, F. Giorgetta, I. Coddington, and N. R. Newbury, "Ultra-Broadband Chirp Linearity Characterization with an Optical Frequency Comb," in *CLEO:2011 - Laser Applications to Photonic Applications*, 2011, p. CWH4.

[26] Z. W. Barber, W. R. Babbitt, B. Kaylor, R. R. Reibel, and P. A. Roos, "Accuracy of active chirp linearization for broadband frequency modulated continuous wave ladar," *Appl. Opt.*, vol. 49, no. 2, pp. 213–219, Jan. 2010.

[27] Z. W. Barber, F. R. Giorgetta, P. A. Roos, I. Coddington, J. R. Dahl, R. R. Reibel, N. Greenfield, and N. R. Newbury, "Characterization of an actively linearized ultrabroadband chirped laser with a fiber-laser optical frequency comb," *Opt. Lett.*, vol. 36, no. 7, pp. 1152–1154, Apr. 2011.

[28] S. L. G. W. C. Swann, "Pressure-induced shift and broadening of 1560–1630-nm carbon monoxide wavelength-calibration lines," *J. Opt. Soc. Am. B-Opt. Phys. - J OPT SOC AM B-OPT Phys.*, vol. 19, no. 10, 2002.

[29] P. C. D. Hobbs, *Building electro-optical systems: making it all work*. New York: Wiley, 2000.

[30] *Labview*. National Instruments.

[31] M. A. Lombardi, "Fundamentals of Time and Frequency," 2nd ed., CRC Press, 2007.

[32] P. E. Ciddor, "Refractive index of air: new equations for the visible and near infrared," *Appl. Opt.*, vol. 35, no. 9, pp. 1566–1573, 1996.

[33] K. P. Birch and M. J. Downs, "Correction to the updated Edlén equation for the refractive index of air," *Metrologia*, vol. 31, no. 4, p. 315, 1994.

[34] "Engineering Metrology Box." .

[35] American National Standards Institute and Laser Institute of America, *American National Standard for safe use of lasers*. Orlando, FL: Laser Institute of America, 2007.

[36] A. V. Jelalian, *Laser radar systems*. Boston: Artech House, 1992.

[37] J. W. Goodman, *Statistical optics*, Wiley classics library ed. New York: Wiley, 2000.

APPENDIX A

MATLAB CODE

APPENDIX: MATLAB CODE

Note – all code written in MATLAB release R2013a or previous.

FMCWPicoDRangesSteadyTarget.m

```
DTIN.Tread = 600e-3;                                %time while you are
grabbing data
DTIN.fs_ADC = 2.5e6/3;                              %sample rate for the
DAQ
DTIN.VertRange = .4;
DTIN.N_Read = round(DTIN.Tread*DTIN.fs_ADC)/2;  %number of samples
boolsave = 0;

F = linspace(0,DTIN.fs_ADC/2,DTIN.N_Read/2);
F = [F -F(end:-1:1)];

Ranges = [];
Trackpk= [];
clk= [];

R = F/4.980911148129962e12*2.99792458e8/2;          % possible range
dr = R(2)-R(1);                                     % range increment

data0max=1.5;                                       %%to avoid data
when servo is throwing errors
peak_threshold_db =-20;

FastAcDualChInitMega(DTIN.N_Read,['test','.bin'],boolsave,DTIN.VertRang
e,DTIN.fs_ADC,1);
fwin = gausswin(DTIN.N_Read);                       %Gaussian window
for i=1:1
        BothCh =
FastAcDualChInitMega(DTIN.N_Read,['test','.bin'],boolsave,DTIN.VertRang
e,DTIN.fs_ADC,0);
        Data0 = BothCh(1:DTIN.N_Read);              % Error Signal

        while max(abs(Data0))>data0max              %checking that the
servo is not throwing any errors
                BothCh =
FastAcDualChInitMega(DTIN.N_Read,['test','.bin'],boolsave,DTIN.VertRang
e,DTIN.fs_ADC,0);
                Data0 = BothCh(1:DTIN.N_Read);
                figure(1);plot(Data0)
                    title('Data0 Raw
ERROR','fontname','Helvetica','fontsize',14)
        end

        figure(1);plot(Data0)
            title('Data0 Raw','fontname','Helvetica','fontsize',14)
        Data1 = BothCh((DTIN.N_Read+1):end);          % Range Data
```

```
        Ch1FFT = fft(Data1);
        N = abs(Ch1FFT/length(Data1)).^2;             %FFT of the Range
Data without windowing
        figure(3);plot(F/1000,10*log10(N))
                title('Detector Output(before
windowing)','fontname','Helvetica','fontsize',14)
                xlim([0 200]);
                ylim([-120 -20]);
                xlabel('kHz','fontname','Helvetica','fontsize',12)
                ylabel('dB','fontsize',12)


        Ch1FFTwin = zeros(size(Ch1FFT));
        nfilt1 = find(F >=128e3,1,'first');         %looking at the
plot for data 0. make sure the reference peak is in between this
numbers
        nfilt2 = find(F >=129.4e3,1,'first');

        Ch1FFTwin(nfilt1:nfilt2) = Ch1FFT(nfilt1:nfilt2);
        Ref = ifft(Ch1FFTwin);
        DataC =Data1./Ref;
        M = abs(fft(fwin.*DataC)/length(Data1)).^2; %FFT of the data
without the ref peak and the modulation noise

        peak =10^(peak_threshold_db/10);
        [Pk,Locs] = findpeaks(M,'MINPEAKHEIGHT',peak);
        Fitbeta = [Pk(1),R(Locs(1)),2*dr];
        BetaFit = fitnonlin(R((-200:200)+Locs(1)),M((-
200:200)+Locs(1)),'gaussfit',Fitbeta);
        range = BetaFit(2);
        Mfit = gaussfit(BetaFit,R((-200:200)+Locs(1)));

        figure(8)
        clf
        lh1 = line(F/1000,10*log10(M),'color','k','linewidth',2);
        lh4 = line(F((-
200:200)+Locs(1))/1000,10*log10(Mfit),'color','r');
        set(gca,'Box','On','fontsize',10,'fontweight','bold');
        grid on;
        xlim([-10 100]);
        ylim([-100 10]);
        title('Detector Output after windowing and Gauss
Fit','fontname','Helvetica','fontsize',14)
        xlabel('kHz','fontname','Helvetica','fontsize',12)
        ylabel('dB','fontsize',12)
        drawnow

        trackpk=10*log10(Pk(1));                    %height of the
peak fitted for tracking the signal power

        Ranges=[Ranges; range];
        Trackpk=[Trackpk; trackpk];
```

```
        clk=[clk; clock];
end

FastAcDualChInitMega(DTIN.N_Read,['test','.bin'],boolsave,DTIN.VertRang
e,DTIN.fs_ADC,-1);
```

FMCW_BPlaser_NONFlatTargetPosition_7Aug14.m

```
Bposition=[0.315507710500456   0.960679102395162];

% Cposition=[0 0];
% Cposition=[0 0.0499183993922];
%Target4
% Cposition2=[0 0];
%Target5
Cposition=[0 0.0999387985636];
%Target6
% Cposition=[0 0.1999468780985];
%Target7

Rangess=Ranges;

Px=[];
Py=[];
b=[];
c=[];

%
%Ranges=[Daa Dba Dca Db Dc]
b=(Rangess(:,2)-mean(Rangess(isfinite(Rangess(:,4)),4))/2-
Rangess(:,1)/2);           %b=(Dba-Db/2-Daa/2)
c=(Rangess(:,3)-mean(Rangess(isfinite(Rangess(:,5)),5))/2-
Rangess(:,1)/2);           %c=(Dca-Dc/2-Daa/2)


for i=1:(length(Rangess))
    if c(i)>=0 && isfinite(c(i))==1 && b(i)>=0 && isfinite(b(i))==1
    [xout,
yout]=circcirc(Cposition(1),Cposition(2),c(i),Bposition(1),Bposition(2)
,b(i));
    px=xout(2);
    py=yout(2);
    else
    px=NaN;
    py=NaN;
    end

Px=[Px; px];
Py=[Py; py];

end
```

```
figure(9)
plot(Py,Px,'o')

Py=Py(isfinite(Py));
Px=Px(isfinite(Px));

Pyfit = smooth(Px,Py,35,'sgolay');
Pxfit = smooth(Py,Px,35,'sgolay');

figure(6)
plot(Py,Px,'b.',Py,Pxfit,'r.');
subplot(2,1,1);plot(Py,Px,'b.',Py,Pxfit,'-r');
xlabel('Py [m]', 'FontName','Times New Roman','FontSize',36);
ylabel('Px [m]', 'FontName','Times New Roman','FontSize',36);
hleg=legend('Measurements','Savitzky-Golay smooth');
set(hleg,'Location','SouthEast');
set(hleg,'FontName','Times New Roman','FontSize',36);
set(gca,'fontsize',24)

subplot(2,1,2);plot(Py,(Px-Pxfit)*1e3,'.') ;
xlabel('Py [m]', 'FontName','Times New Roman','FontSize',36);
ylabel('Residuals Px [mm]', 'FontName','Times New
Roman','FontSize',36);
set(gca,'fontsize',24)

figure(4)
subplot(2,1,1);plot(Px,Py,'b.',Px,Pyfit,'.r');
xlabel('Px [m]', 'FontName','Times New Roman','FontSize',36);
ylabel('Py [m]', 'FontName','Times New Roman','FontSize',36);
hleg=legend('Measurements','Linear Fit');
set(hleg,'Location','SouthEast');
set(hleg,'FontName','Times New Roman','FontSize',36);
set(gca,'fontsize',24)

subplot(2,1,2);plot(Px,(Py-Pyfit)*1e3,'.')
xlabel('Px [m]', 'FontName','Times New Roman','FontSize',36);
ylabel('Residuals Py [mm]', 'FontName','Times New
Roman','FontSize',36);
set(gca,'fontsize',24)
```

errorPropPxPy.m

```
function
[Px,Py,STDPx,STDPy]=errorPropPxPy(b,c,Cy,Cx,By,Bx,deltaBy,deltaBx)
%outputs are in meters

% b=1.10252;
% c=1.23262;
% Cy=0.05;
% Cx=0;
```

```
% By=0.96163;
% Bx=0.31584;

[px,py]=circcirc(Cx,Cy,c,Bx,By,b);

Px=px(2);
Py=py(2);

CovMatrix=1e-9*[0.165121009210967   0.030682347563699
0.000003355079431   0       -0.000006167992186    1e-5;
                0.030682347563699   0.057177660331158  -
0.000006167992186   1e-5       0                       0;
                0.000003355079431  -0.000006167992186
0.000000533713393   0       0                       0;
                0                   1e-5                    0
1e-5       0                    0;
                -0.000006167992186  0                   0
0       deltaBy^2*1e9         2.4256;
                1e-5                    0                   0
0       2.4256              deltaBx^2*1e9  ];


dPx=[];                         %[b c Cy Cx By Bx]
dPx(1)=-1/(2*(Bx-Cx));
%partial derivative of Px with respect to c
dPx(2)=1/(2*(Bx-Cx));
%partial derivative of Px with respect to b
dPx(3)=(-Cy+Py)/(Bx-Cx);
%partial derivative of Px with respect to Cy
dPx(4)=(Bx^2+By^2-2*Py*By+Cx^2-Cy^2+2*Py*Cy-b+c-2*Bx*Cx)/(2*(Bx-Cx)^2);
%partial derivative of Px with respect to Cx
dPx(5)=(By-Py)/(Bx-Cx);
%partial derivative of Px with respect to By
dPx(6)=(b+Cx^2-2*Bx*Cx-c+Cy^2-2*Py*Cy-By^2+2*By*Py+Bx^2)/(2*(Cx-Bx)^2);
%partial derivative of Px with respect to Bx

M=[];
for i=1:6
    for j=1:6
        M(i,j)=dPx(i)*dPx(j);
    end
end

ErrorPropMatrixPx=M.*CovMatrix;

VPx=sum(sum(ErrorPropMatrixPx));
STDPx=VPx^(1/2)

dPy=[];                         %[b c Cy Cx By Bx]
dPy(1)=-1/(2*(By-Cy));
dPy(2)=1/(2*(By-Cy));
```

```
dPy(3)=(-b+Bx^2-2*Bx*Px+c-Cx^2+2*Cx*Px+By^2-2*By*Cy+Cy^2)/(2*(By-
Cy)^2);
dPy(4)=(Cx-Px)/(Cy-By);
dPy(5)=(b-Bx^2+2*Bx*Px-c+Cx^2-2*Cx*Px+Cy^2-2*Cy*By+By^2)/(2*(Cy-By)^2);
dPy(6)=(Px-Bx)/(Cy-By);

N=[];
for i=1:6
    for j=1:6
        N(i,j)=dPy(i)*dPy(j);
    end
end

ErrorPropMatrixPy=N.*CovMatrix;

VPy=sum(sum(ErrorPropMatrixPy));
STDPy=VPy^(1/2)
end
```

photonBudget.m

```
Pamplified=0.8;          %Output power for optical amplifier [W]
Pamplified=0.614*Pamplified;%Losses at the fiber connecting the amp
with the set up (low transmission)
tr=0.7;                     %Target reflectivity, assume 70%
Ra=1.6;
Rc=1.58;                    %range to target from emitter C[m]
Rb=1.50;                    %range to target from emitter B[m]
SMFdiam=10.5e-6;               %Single Fiber Mode diameter [m]
etaATM=1;                   %atmospheric propagation efficiency
lambda=1536e-9;             %wavelength [m]
Dgaussianaftertriplecollimator=3.736e-3;    %from data sheet

PC=0.5*0.9999*0.9*Pamplified;      %power emitted by C
PB=0.5*0.9999*0.9*Pamplified;      %power emitted by B
PA=0.0001*0.9*Pamplified;          %power emitted by A

PLO=0.0857*Pamplified              %power at LO path
PLO=PLO/100;                       %after a 20 dB attenuator

nLO=2;
PLO=PLO/(10^(0.3*nLO/10))  %power at LO path after fiber losses

wB=0.2214;                 %spot of B beam on target from gaussian beam
propagation eq for B beam
AtB=pi*wB^2;
wC=0.2332;                 %spot of C beam on target from gaussian beam
propagation eq for B beam
AtC=pi*wC^2;
wA0=409.5e-6;              %spot of A beam on target from gaussian beam
propagation eq
```

```
Ar=pi*wA0^2;

PBLamber=PB*Ar/AtB;         %Power of beam B hitting spot of A beam
area and being redirected by target as a lambertian source
PCLamber=PC*Ar/AtC;         %Power of beam C hitting spot of A beam
area and being redirected by target as a lambertian source
PALamber=PA;                %Power of beam A hitting spot of A beam
area and being redirected by target as a lambertian source

omegaLamber=2*pi;               %solid angle lambertian source [sr]
Arec=pi*(Dgaussianaftertriplecollimator/2)^2;           %area receiver
RBLamber=PBLamber*tr/(Ar*omegaLamber);         %Radiance of the
lambertian source with B power [W/(m^2*sr)]
RCLamber=PCLamber*tr/(Ar*omegaLamber);         %Radiance of the
lambertian source with C power [W/(m^2*sr)]
RALamber=PALamber*tr/(Ar*omegaLamber);         %Radiance of the
lambertian source with C power [W/(m^2*sr)]
omegaDet=Arec/Ra^2;              %solid angle detector [sr]

PBA=RBLamber*Ar*omegaDet;
PCA=RCLamber*Ar*omegaDet;
PAA=RALamber*Ar*omegaDet;

Pcollected=PAA+PBA+PCA;                 %in [W]=[J/s]
Eph=1.2933e-19;                         %Photon energy at 1536nm
[J/photon]

c=2.99792458e8;                      %speed of light [m/s]
e=1.60217657e-19;                    %electron charge [C]
n=0.7;                               %quantum detector efficiency

Tint=8e-3;                              %pulse length or integration
time (8e-3 for BP and 2.3e-3 for DFB) [s]
deltaR=c/(2*1.818e12);                  %range resolution
BforBP=1.818e12, BforDFB=76.59e9

PRXAA=0.9999*PAA;
PRXBA=0.9999*PBA;
PRXCA=0.9999*PCA;


NrecAA=PRXAA*Tint/Eph                %taking as the integration time
Tread
NrecBA=PRXBA*Tint/Eph
NrecCA=PRXCA*Tint/Eph

NA=0.12;
nf=1.486;                           %Fibre refractive index
S=(NA)^2/(4*nf^2);                   %S=fraction of Rayleigh scattering
reflecting backwards = NA^2/(4*n^2)
Ray_scat=4.6e-5;                     %rayleigh scattering factor per
meter [1/m]
```

```
eta_ray = Ray_scat*deltaR*S;           %backwards rayleigh scattering
factor for a range resolution bin

P_ray = PB*eta_ray/10000/2*2;      %99.99% amplitude ratio translates
in a 10000 power factor, the /2 is because the 50/50, *2 because of
having B and C
N_ray = (P_ray/Eph)*Tint             %number of photons

CNRAA_ray=NrecAA/N_ray;
CNRAA_raydB=10*log10(CNRAA_ray)
CNRBA_ray=NrecBA/N_ray;
CNRBA_raydB=10*log10(CNRBA_ray)
CNRCA_ray=NrecCA/N_ray;
CNRCA_raydB=10*log10(CNRCA_ray)

SNRAA_ray=(1+CNRAA_ray)^2/(1+2*CNRAA_ray);
SNRAA_raydB=10*log10(SNRAA_ray)
precAA_ray=deltaR/sqrt(SNRAA_raydB);
SNRBA_ray=(1+CNRBA_ray)^2/(1+2*CNRBA_ray);
SNRBA_raydB=10*log10(SNRBA_ray)
precBA_ray=deltaR/sqrt(SNRBA_raydB);
SNRCA_ray=(1+CNRCA_ray)^2/(1+2*CNRCA_ray);
SNRCA_raydB=10*log10(SNRCA_ray)
precCA_ray=deltaR/sqrt(SNRCA_raydB);

F=1.995;                               %3 dB drop because of hanning

CNRAA=n*NrecAA/F;                       %CNR high LO power in heterodyne
detection at the shot limit
CNRAAdB=10*log10(CNRAA)
CNRBA=n*NrecBA/F;                       %CNR high LO power in heterodyne
detection at the shot limit
CNRBAdB=10*log10(CNRBA)
CNRCA=n*NrecCA/F;                       %CNR high LO power in heterodyne
detection at the shot limit
CNRCAdB=10*log10(CNRCA)

deltaRr=c/(2*1.818e12)*2*2;           %reduced by 2 because of the 3
chunk method and by other 2 becuase the hanning window

SNRAA=(1+CNRAA)^2/(1+2*CNRAA);%SNR high LO power in heterodyne
detection at the shot limit
SNRAAdB=10*log10(SNRAA)
precAA=deltaRr/sqrt(SNRAAdB)
SNRBA=(1+CNRBA)^2/(1+2*CNRBA);%SNR high LO power in heterodyne
detection at the shot limit
SNRBAdB=10*log10(SNRBA)
precBA=deltaRr/sqrt(SNRBAdB)
SNRCA=(1+CNRCA)^2/(1+2*CNRCA);%SNR high LO power in heterodyne
detection at the shot limit
SNRCAdB=10*log10(SNRCA)
precCA=deltaRr/sqrt(SNRCAdB)
```